Use this document as a template

Millikelvin Confocal Microscopy of Semiconductor Membranes and Filter Functions for Unital Quantum Operations

Customise this page according to your needs

Tobias Hangleiter*

September 8, 2025

---

* A LaTeX lover/hater

The harmony of the world is made manifest in Form and Number, and the heart and soul and all the poetry of Natural Philosophy are embodied in the concept of mathematical beauty.

– D'Arcy Wentworth Thompson

Summary

Zusammenfassung

Acknowledgements

Preface

It's been a journey.

<div align="right">

Tobias Hangleiter
Aachen, September 2025

</div>

How to read this thesis

Contents

Publications

[1] Yaiza Aragonés-Soria, René Otten, Tobias Hangleiter, Pascal Cerfontaine, and David Gross. "Minimising Statistical Errors in Calibration of Quantum-Gate Sets." June 7, 2022. DOI: 10.48550/arXiv.2206.03417. arXiv: 2206.03417 [quant-ph]. Pre-published.

[2] Pascal Cerfontaine, Tobias Hangleiter, and Hendrik Bluhm. "Filter Functions for Quantum Processes under Correlated Noise." In: *Physical Review Letters* 127.17 (Oct. 18, 2021), p. 170403. DOI: 10.1103/PhysRevLett.127.170403.

[3] Thomas Descamps, Feng Liu, Sebastian Kindel, René Otten, Tobias Hangleiter, Chao Zhao, Mihail Ion Lepsa, Julian Ritzmann, Arne Ludwig, Andreas D. Wieck, Beata E. Kardynał, and Hendrik Bluhm. "Semiconductor Membranes for Electrostatic Exciton Trapping in Optically Addressable Quantum Transport Devices." In: *Physical Review Applied* 19.4 (Apr. 28, 2023), p. 044095. DOI: 10.1103/PhysRevApplied.19.044095.

[4] Thomas Descamps, Feng Liu, Tobias Hangleiter, Sebastian Kindel, Beata E. Kardynał, and Hendrik Bluhm. "Millikelvin Confocal Microscope with Free-Space Access and High-Frequency Electrical Control." In: *Review of Scientific Instruments* 95.8 (Aug. 9, 2024), p. 083706. DOI: 10.1063/5.0200889.

[5] Denny Dütz, Sebastian Kock, Tobias Hangleiter, and Hendrik Bluhm. "Distributed Bragg Reflectors for Thermal Isolation of Semiconductor Spin Qubits." In preparation.

[6] Sarah Fleitmann, Fabian Hader, Jan Vogelbruch, Simon Humpohl, Tobias Hangleiter, Stefanie Meyer, and Stefan van Waasen. "Noise Reduction Methods for Charge Stability Diagrams of Double Quantum Dots." In: *IEEE Transactions on Quantum Engineering* 3 (2022), pp. 1–19. DOI: 10.1109/TQE.2022.3165968.

[7] Fabian Hader, Jan Vogelbruch, Simon Humpohl, Tobias Hangleiter, Chimezie Eguzo, Stefan Heinen, Stefanie Meyer, and Stefan van Waasen. "On Noise-Sensitive Automatic Tuning of Gate-Defined Sensor Dots." In: *IEEE Transactions on Quantum Engineering* 4 (2023), pp. 1–18. DOI: 10.1109/TQE.2023.3255743.

[8] Tobias Hangleiter, Pascal Cerfontaine, and Hendrik Bluhm. "Filter-Function Formalism and Software Package to Compute Quantum Processes of Gate Sequences for Classical Non-Markovian Noise." In: *Physical Review Research* 3.4 (Oct. 18, 2021), p. 043047. DOI: 10.1103/PhysRevResearch.3.043047.

[9] Tobias Hangleiter, Pascal Cerfontaine, and Hendrik Bluhm. "Erratum: Filter-function Formalism and Software Package to Compute Quantum Processes of Gate Sequences for Classical Non-Markovian Noise [Phys. Rev. Research 3, 043047 (2021)]." In: *Physical Review Research* 6.4 (Oct. 16, 2024), p. 049001. DOI: 10.1103/PhysRevResearch.6.049001.

[10] Isabel Nha Minh Le, Julian D. Teske, Tobias Hangleiter, Pascal Cerfontaine, and Hendrik Bluhm. "Analytic Filter-Function Derivatives for Quantum Optimal Control." In: *Physical Review Applied* 17.2 (Feb. 2, 2022), p. 024006. DOI: 10.1103/PhysRevApplied.17.024006.

[11] Paul Surrey, Julian D. Teske, Tobias Hangleiter, Pascal Cerfontaine, and Hendrik Bluhm. "Data-Driven Qubit Characterization and Optimal Control Using Deep Learning." In preparation.

[12] Kui Wu, Sebastian Kindel, Thomas Descamps, Tobias Hangleiter, Jan Christoph Müller, Rebecca Rodrigo, Florian Merget, Beata E. Kardynal, Hendrik Bluhm, and Jeremy Witzens. "Modeling an Efficient Singlet-Triplet-Spin-Qubit-to-Photon Interface Assisted by a Photonic Crystal Cavity." In: *Physical Review Applied* 21.5 (May 24, 2024), p. 054052. DOI: 10.1103/PhysRevApplied.21.054052.

[13] Kui Wu, Sebastian Kindel, Thomas Descamps, Tobias Hangleiter, Jan Christoph Müller, Rebecca Rodrigo, Florian Merget, Hendrik Bluhm, and Jeremy Witzens. "An Efficient Singlet-Triplet Spin Qubit to Fiber Interface Assisted by a Photonic Crystal Cavity." In: *The 25th European Conference on Integrated Optics.* Ed. by Jeremy Witzens, Joyce Poon, Lars Zimmermann, and Wolfgang Freude. Cham: Springer Nature Switzerland, 2024, pp. 365–372. DOI: 10.1007/978-3-031-63378-2_60.

Software

The following open-source software packages were developed (at least partially) during the work on this thesis.

[1] Tobias Hangleiter, Isabel Nha Minh Le, and Julian D. Teske, *Filter_functions* version v1.1.3, May 14, 2024. Zenodo. DOI: 10.5281/ZENODO.4575000,

[2] Tobias Hangleiter, *Lindblad_mc_tools* Aug. 8, 2025. URL: https://git.rwth-aachen.de/tobias.hangleiter/lindblad_mc_tools.

[3] Tobias Hangleiter, *Mjolnir* Aug. 8, 2025. URL: https://git-ce.rwth-aachen.de/qutech/python-mjolnir.

[4] Tobias Hangleiter, Simon Humpohl, Max Beer, Paul Surrey, and René Otten, *Python-Spectrometer* version 2025.9.1, Sept. 8, 2025. Zenodo. DOI: 10.5281/zenodo.17079009,

[5] Tobias Hangleiter, Simon Humpohl, Paul Surrey, and Han Na We, *Qutil* version 2025.8.1, Aug. 12, 2025. Zenodo. DOI: 10.5281/zenodo.16816394,

Part I

A FLEXIBLE PYTHON TOOL FOR FOURIER-TRANSFORM NOISE SPECTROSCOPY

Introduction | 1

N OISE is ubiquitous in condensed matter physics experiments, and in mesoscopic systems in particular it can easily drown out the sought-after signal. In solid-state quantum technology research, devices on the length scale of the Fermi wavelength – say tens of nanometers – are embedded in a crystalline matrix of 10^{23} atoms. These devices host single quantum objects such as electrons or quasiparticles—collective many-body excitations. They are controlled and measured by classical signals routed to the device through macroscopic connections like cables and fibers. The signals, in turn, are generated and analyzed by electronic (*e.g.*, transistors) or optical instruments (*e.g.*, lasers) that, in all likelihood, are again based on solid-state technology driven by the first quantum revolution [2, 3]. Ultimately, then, the experiments take place in an environment full of external influences from trams passing by, shaking the ground, to cosmic rays creating electron-hole or breaking up Cooper pairs.

All of these different layers to such experiments are inherently – and in fact often fundamentally[1] – *noisy*, and it is the physicist's challenge to measure their desired effects in spite of this noise. A well-thought-out experimental setup is hence one that has been designed taking the various noise sources into consideration, and state-of-the-art experiments often need to push the frontier in order to be successful. From material choice in the sample to the signal path and the specs of the measurement equipment, many aspects need to be optimized and, in particular, characterized in order to assess the noise. Indeed, the assessment of noise might even be the entire *goal* of the experiment, for instance to evaluate material properties. In this case, the quantity being measured might not be the same quantity whose noise one is interested in but rather some function of it, and the resulting data still needs to be transformed before one is able to make any practical statements about those properties.

Noise, in the sense that we are concerned with in the present thesis,[2] is a stochastic process, meaning that we cannot predict with certainty a dynamical system's time evolution; it *fluctuates* randomly around its noise-free value.[3] Only by obtaining statistics, *i.e.*, repeated observations, either by preparing the system in the same initial state or measuring for a certain amount of time, can we make any statements about the underlying stochastic process. Two questions are key to assessing these statistics: first, what is the amplitude of the fluctuations? And second, at which frequency do the fluctuations occur? If the amplitude is small enough, we might not need to care, and if the frequency is large enough, we might be able to average out the fluctuations while if it is small enough, it might appear *quasistatic* and we might be able to subtract them. Although numerous other techniques for measuring and estimating a noise's properties exist, analyzing noise in frequency space by means of the Fourier transform imposes itself when considering these two notions.

[1]: Bluhm, Hangleiter, Neul, Kammerloher, Visser, Beer, Willmes, Struck, Huckemann, Grothe, Humpohl, Xue, Surrey, We, and Schreiber (2022), *Research Techniques for Advanced Solid State Device Experiments*

a: RWTH Aachen University and Forschungszentrum Jülich GmbH.

b: Then at RWTH Aachen University and Forschungszentrum Jülich GmbH.

1: Consider Johnson-Nyquist noise in a resistor, for example.

2: Quantum noise does not fall under this scope as it may – disregarding vacuum fluctuations for the sake of argument – be considered *emergent*; it arises from a system entangled with a (not necessarily large) number of quantum degrees of freedom being observed, *i.e.*, tracing out the environment's degrees of freedom. Our lack of knowledge about this environment then appears as noise in our observations. See Reference 4 for a comprehensive review of the quantum case.

3: Quantum measurements are also noisy in this sense as we cannot predict the outcome of a single-shot measurement, but here the stochasticity is in the outcomes of an ensemble rather than the sequence of values in time. The two are, however, closely related through ergodicity, which we will require in Section 2.1.

This approach is the central topic of this part of the present thesis. However, we will neither be too much concerned with the theoretical side of the subject matter nor with the details of its practical application in identifying and mitigating noise.[4] Rather, I will focus on making these techniques readily and easily accessible to experimentalists in the lab. Given the arguments laid out above, noise spectroscopy should be an essential item in an experimentalists toolbelt. In practice, though, we are faced with several challenges. First, different experiments require different data acquisition (DAQ) hardware, all of which have both varying capabilities and software interfaces. Hence, transferring a spectroscopy code from one device or setup to another is a non-trivial task and can inhibit adoption of the technique. Albeit some instruments come with built-in spectroscopy solutions, they vary in functionality and are not easily transferred to different systems. Second, while probably everyone finding themselves in the situation is capable of computing the noise spectrum when presented with a set of time series data, inferring the correct parameters for data acquisition given the desired parameters of the resulting spectrum can, while not difficult, be cumbersome to do.[5] Lastly, noise spectroscopy is most effective when proper visualization tools are employed. Again, this is not a difficult task per se, but such things always incur overhead costs that can deter users from employing these essential techniques.

Here, I address these points by introducing a Python software package, `python_spectrometer` [6], that tackles the entire processing chain of practical noise spectroscopy in a physics laboratory. By abstracting DAQ hardware into a unified interface, it is portable between different setups. With the goal to make noise spectroscopy as accessible as possible and lower the entry barrier, it automatically handles parameter inference and hardware constraints. Finally, it provides a comprehensive plotting solution that allows for interactively analyzing the data using various different data visualization methods. I will employ the tool to perform displacement noise spectroscopy in a cryogenic confocal microscope in Part II using two different methods that highlight its versatility.

The remainder of this part is structured as follows. In Chapter 2, I review the mathematical groundwork underpinning noise spectroscopy by means of Fourier transforms of time series and discuss parameters and properties of the central quantity of interest, the power spectral density (PSD). In Chapter 3, I then present the software package by going over its design choices and giving a walkthrough of its features using a typical workflow as an example. I conclude by giving an outlook on future directions in Chapter 4.

4: I refer the interested reader to the lecture material of Refences 5 and 1 and references therein.

5: Although it is of course a good exercise, and, as a physicist, one should always strive to understand the tools one is using and the underlying principles at work. This part of the present thesis is intended to provide a starting point for that.

Theory of spectral noise estimation

2

THERE exist various methods for estimating the properties of noise in a classical signal $x(t)$.[1] A simple metric quantifying the average noise amplitude of the signal observed from time $t = 0$ to $t = T$ is the root mean square (RMS) [8],

$$\mathrm{RMS}_x = \sqrt{\frac{1}{T} \int_0^T \mathrm{d}t\, |x(t)|^2}. \tag{2.1}$$

While this already tells us *something* about the noise, it is evident that a single number does not provide many clues if we were to attempt to mitigate the noise or say something qualitative about it beyond "small" and "large". In cases such as these, physics has often turned to the *spectral* representation of the function of interest. Knowing the frequency content of a function gives access to a wealth of information about the underlying contributing processes. But how can we learn how a system behaves as a function of frequency?

Consider an electrical black box – some device under test (DUT) – with two leads connected to a lock-in amplifier (LIA) as sketched in Figure 2.1. Assuming the DUT is conducting, we could simply measure the conductance $G(t) = I(t)/V(t)$ through the device for some time T with a given lock-in modulation frequency f_i, subtract the constant offset,[2] and calculate the RMS using Equation 2.1. Repeating this procedure for different modulation frequencies $\{f_i\}_i$, we would collect a set of RMS-values that we could assign to the modulation frequencies at which they were measured and thus sample the noise amplitude spectrum[3] of the conductance, $S_G(f_i)$.[4] This method has the advantage that we can choose the frequencies at which the spectrum should be sampled—in particular they do not have to be evenly spaced. However, it has two significant shortcomings. First, it is rather inefficient and therefore time-consuming. For N frequency sample points, it takes a total time of NT to acquire all data, where T needs to be chosen such that the variance of RMS_G is sufficiently small. Second, and crucially, it is not always possible to excite the system at a certain frequency and measure its response. For example, it is generally considered hard[5] to – deliberately – excite vibrations of a specific frequency in a cryostat, yet we might still be interested in the displacement spectrum inside of it. A related method is available if one has access to a frequency-tunable probe, that is, a physical system whose behavior – typically its time evolution or some measurable property after letting the system evolve – under noise is well understood within a given noise model, and that can be controlled to be sensitive to a certain frequency. One example for such methods is dynamical decoupling (DD)-based noise spectroscopy using a qubit [9–12], a protocol based on insights gained from the filter-function formalism—see Part IV. These protocols are especially well-suited for high but less so for low frequencies as they rely on observing the coherence of a qubit and hence the visibility on long time scales.

In a sense the most straight-forward way of measuring the noise spectrum presents itself as a consequence of the Wiener-Khinchin theorem [13, 14] that relates the noise spectrum to the Fourier transform of a time-dependent signal. This makes it possible to estimate the noise spectrum by simply observing a signal for a certain amount of time and perform-

1: We discuss only classical noise here, meaning $x(t)$ commutes with itself at all times. For descriptions of and spectroscopy protocols for quantum noise refer to Refences 4 and 7, for example.
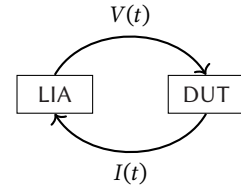
Figure 2.1: Measuring the conductance through a device under test (DUT) using a lock-in amplifier (LIA).

2: The constant part $G_0 = G(t) - \delta G(t)$ of course also holds some information about the system, for example about its bandwidth.

3: We will properly define this term below.

4: See Subsection 3.2.1 for a discussion on how the RMS at a certain frequency relates to other quantities discussed in this part.

5: And also unpopular with colleagues.

ing some post-processing![6] This method will be the topic of the present chapter. It is laid out as follows. I will first derive the Wiener-Khinchin theorem for continuous stochastic processes and introduce the central quantity of interest in noise spectroscopy; the PSD. Then, I will discretize the method and discuss resulting side-effects before describing an efficient way of obtaining the spectrum from a finite amount of data. I will conclude by elaborating on relevant parameters and properties.

2.1 Spectrum estimation from time series

To see how spectral noise properties may be estimated from time series data, consider a continuous wide-sense stationary[7] signal in the time domain, $x(t) \in \mathbb{C}$, that is observed for some time T. We define the windowed Fourier transform of $x(t)$ and its inverse by[8]

$$\hat{x}_T(\omega) = \int_0^T \mathrm{d}t\, x(t)e^{-i\omega t} \tag{2.2}$$

$$x(t) = \int_{-\infty}^{\infty} \frac{\mathrm{d}\omega}{2\pi}\hat{x}_T(\omega)e^{i\omega t}, \tag{2.3}$$

i.e., we assume that outside of the window of observation $x(t)$ is zero. The autocorrelation function of $x(t)$ is given by

$$C(\tau) = \langle x^*(t)x(t+\tau)\rangle \tag{2.4}$$

$$= \lim_{T\to\infty} \frac{1}{T} \int_0^T \mathrm{d}t\, x^*(t)x(t+\tau), \tag{2.5}$$

where $\langle \cdot \rangle$ is the ensemble average over multiple realizations of the process and the last equality holds true for ergodic processes. Expressing $x(t)$ in terms of its Fourier representation (Equation 2.2) and reordering the integrals, we get

$$C(\tau) = \lim_{T\to\infty} \frac{1}{T} \int_0^T \mathrm{d}t \int_{-\infty}^{\infty} \frac{\mathrm{d}\omega}{2\pi}\hat{x}_T^*(\omega)e^{-i\omega t} \int_{-\infty}^{\infty} \frac{\mathrm{d}\omega'}{2\pi}\hat{x}_T(\omega')e^{i\omega'(t+\tau)} \tag{2.6}$$

$$= \lim_{T\to\infty} \frac{1}{T} \int_{-\infty}^{\infty} \frac{\mathrm{d}\omega}{2\pi} \int_{-\infty}^{\infty} \frac{\mathrm{d}\omega'}{2\pi}\hat{x}_T^*(\omega)\hat{x}_T(\omega')e^{i\omega'\tau} \int_0^T \mathrm{d}t\, e^{it(\omega'-\omega)} \tag{2.7}$$

The innermost integral approaches a δ-function for large T, allowing us to further simplify this under the limit as

$$C(\tau) = \lim_{T\to\infty} \frac{1}{T} \int_{-\infty}^{\infty} \frac{\mathrm{d}\omega}{2\pi} \int_{-\infty}^{\infty} \frac{\mathrm{d}\omega'}{2\pi}\hat{x}_T^*(\omega)\hat{x}_T(\omega')e^{i\omega'\tau}2\pi\delta(\omega'-\omega) \tag{2.8}$$

$$= \lim_{T\to\infty} \frac{1}{T} \int_{-\infty}^{\infty} \frac{\mathrm{d}\omega}{2\pi}|\hat{x}_T(\omega)|^2 e^{i\omega\tau} \tag{2.9}$$

$$= \int_{-\infty}^{\infty} \frac{\mathrm{d}\omega}{2\pi}S(\omega)e^{i\omega\tau} \tag{2.10}$$

with the power spectral density (PSD)[9]

$$S(\omega) = \lim_{T\to\infty} \frac{1}{T}|\hat{x}_T(\omega)|^2 \tag{2.11}$$

$$= \int_{-\infty}^{\infty} \mathrm{d}\tau\, C(\tau)e^{-i\omega\tau} \tag{2.12}$$

6: An interesting combination of the Fourier-transform-based and the qubit-based spectroscopy methods was recently proposed in Reference 15, where the authors compute the spectrum by Fourier-transforming the second derivative of the coherence function.

7: For a wide-sense stationary (also called weakly stationary) process $x(t)$, the mean is constant and the autocorrelation function $C(t,t') = \langle x^*(t)x(t')\rangle$ simplifies to $\langle x^*(t)x(t+\tau)\rangle = \langle x^*(0)x(\tau)\rangle$ with $\tau = t' - t$ and where $\langle \cdot \rangle$ is the ensemble average. That is, it is a function of only the time lag τ and not the absolute point in time. For Gaussian processes as discussed here, this also implies stationarity [16]. The property further implies that $C(\tau)$ is an even function.

8: In this chapter we will always denote the Fourier transform of some quantity ξ using the same symbol with a hat, $\hat{\xi}$.

9: The term *power spectrum* is often used interchangeably. I will do so as well, but emphasize at this point that in digital signal processing in particular, the *spectrum* is a different quantity from the *spectral density*. See also Sidenote 21 in Chapter 3.

Equation 2.10 is the Wiener-Khinchin theorem [13, 14] that states that the autocorrelation function $C(\tau)$ and the PSD $S(\omega)$ are Fourier-transform pairs [16]. Furthermore, defining the latter through Equation 2.11 gives us an intuitive picture of the PSD if we recall Parseval's theorem,

$$\int_{-\infty}^{\infty} \frac{\mathrm{d}\omega}{2\pi} \frac{1}{T} |\hat{x}_T(\omega)|^2 = \frac{1}{T} \int_0^T \mathrm{d}t \, |x(t)|^2. \qquad (2.13)$$

That is, the total power P contained in the signal $x(t)$ is given by integrating over the PSD. Similarly, the power contained in a band of frequencies $[\omega_1, \omega_2]$ is given by

$$P(\omega_1, \omega_2) = \mathrm{RMS}_S(\omega_1, \omega_2)^2 \qquad (2.14)$$

$$= \int_{\omega_1}^{\omega_2} \frac{\mathrm{d}\omega}{2\pi} S(\omega) \qquad (2.15)$$

where $\mathrm{RMS}_S(\omega_1, \omega_2)$ is the root mean square within this frequency band. These relations are helpful when analyzing noise PSDs to gauge the relative weight of contributions from different frequency bands to the total noise power.

To become familiar with the quantities $C(\tau)$ and $S(\omega)$, consider the Ornstein-Uhlenbeck process [17], the only stationary Gaussian Markovian stochastic process [18]. The autocorrelation function of the Ornstein-Uhlenbeck process is given by

$$C(\tau) = \sigma^2 e^{-\tau/\tau_c}, \qquad (2.16)$$

with σ the RMS and τ_c the correlation time of the process. The PSD in turn is the Lorentzian function

$$S(\omega) = \frac{2\sigma^2 \tau_c}{1 + (\omega\tau_c)^2}. \qquad (2.17)$$

For a given discretization time step Δt and hence bandwidth $\omega \in [0, \pi f_s]$, the Ornstein-Uhlenbeck process interpolates between perfectly uncorrelated, white noise ($\Delta t/\tau_c \to \infty$, $S(\omega) = 2\tau_c\sigma^2$), correlated, Brownian noise ($\Delta t/\tau_c \gg 1$, $S(\omega) = 2\sigma^2/\tau_c\omega^2$), and perfectly correlated, quasistatic noise ($\Delta t/\tau_c \to 0$, $S(\omega) = \sigma^2\delta(\omega)$), although I note that it is still Markovian in all cases. Figure 2.2 depicts simulated data and its autocorrelation function and PSD for exemplary parameters: in the white noise limit ($\tau_c = 10^{-2}\Delta t$, blue), in the intermediate regime ($\tau_c = \Delta t$, magenta), and in the correlated regime ($\tau_c = 10^2\Delta t$, green). From the time series plot at the top it becomes clear that the RMS alone is insufficient to describe the properties of noisy signals as the curves differ significantly despite being normalized to their RMS. The autocorrelation functions averaged over 10^3 realizations of the noisy signals as well as their theoretical (continuous) value, Equation 2.16, are plotted in the middle panel, normalized to $\tau_c = \Delta t$ and $\sigma^2 = \Delta t/4$. For the white noise limit (blue), correlations are too short to be resolved with the given time discretization. The correlations decay to e^{-1} at $\tau/\tau_c = 10^{-2}, 1, 10^2$, respectively. Finally, the bottom panel shows the PSD, Equation 2.17, and its periodogram estimate, again averaged over 10^3 realizations of the signal and normalized to $\tau_c = \Delta t$ and $\sigma^2 = \Delta t/4$. The cross-over from white to Brownian PSD occurs at $\omega = \tau_c$. While the simulated data for $\tau_c = 10^{-2}\Delta t$ appears perfectly white, that for $\tau_c = 10^2\Delta t$ appears perfectly $1/f$-like because the spectrum is only white below the smallest resolvable frequency $\Delta f = T^{-1}$.

Having gotten an intuition for the quantities $C(\tau)$ and $S(\omega)$, let us move
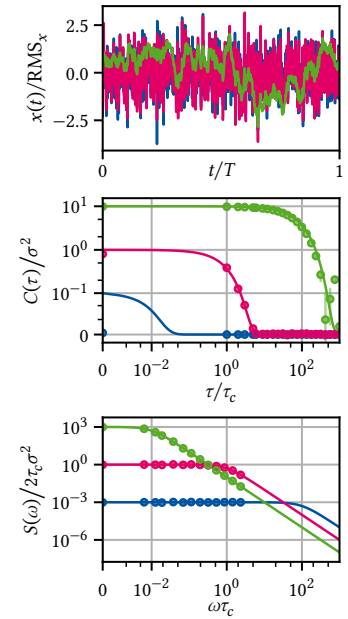
Figure 2.2: Ornstein-Uhlenbeck process. Simulated time traces, autocorrelation function, and PSD of the Ornstein-Uhlenbeck process. Top: Simulated time traces using the algorithm presented in ??. The data are normalized to the computed RMS (equal to σ in the continuous case). Middle: Theoretical autocorrelation function (Equation 2.16, solid lines) computed from the simulated data averaged over 10^3 traces (circles, subset of points). Error bars indicate the standard error of the mean, axes are scaled with respect to the parameters of the magenta data, and data are plotted on an asinh-scale. Bottom: Theoretical PSD (Equation 2.17, solid lines) and periodograms computed from the simulated data using scipy.signal.periodogram(), cf. Equation 2.21, averaged over 10^3 traces (circles, subset of points). Axes are again scaled with respect to the parameters of the magenta data and plotted on an asinh-scale. Parameters are $\tau_c = \Delta t \times \{10^{-2}, 1, 10^2\}$ and $\sigma^2 = \sqrt{\tau_c}/4$ for blue, magenta, and green data, respectively.

on to see how the latter may be obtained from time series data. Equation 2.11 represents the starting point for the experimental spectrum estimation procedure. Instead of a continuous signal $x(t), t \in [0, T]$, consider its discretized version[10]

$$x_n, \quad n \in \{0, 1, \dots, N - 1\} \qquad (2.18)$$

defined at times $t_n = n\Delta t$ with $T = N\Delta t$ and where $\Delta t = f_s^{-1}$ is the sampling interval (the inverse of the sampling frequency f_s). Invoking the ergodic theorem,[11] we can replace the long-term average in Equation 2.11 by the ensemble average over M realizations of the noisy signal, $\left\{ x_n^{(m)} \right\}_m$, and write

$$S_n = \frac{1}{M} \sum_{m=0}^{M-1} \left| \hat{x}_n^{(m)} \right|^2 \qquad (2.19)$$

$$= \frac{1}{M} \sum_{m=0}^{M-1} S_n^{(m)} \qquad (2.20)$$

where $\hat{x}_n^{(m)}$ is the discrete Fourier transform of $x_n^{(m)}$, we defined the *periodogram* of $x_n^{(m)}$ by

$$S_n^{(m)} = \left| \hat{x}_n^{(m)} \right|^2, \qquad (2.21)$$

and S_n is an *estimate* of the true PSD sampled at the discrete frequencies $\omega_n = 2\pi n/T \in 2\pi \times \{ -f_s/2, \dots, f_s/2 \}$. Equation 2.19 is known as Bartlett's method [21] for spectrum estimation.[12]

To better understand the properties of this estimate, let us take a look at the parameters Δt, N, and M. The sampling interval Δt defines the largest resolvable frequency by the Nyquist sampling theorem,

$$f_{\max} = \frac{f_s}{2} = \frac{1}{2\Delta t}. \qquad (2.22)$$

In turn, the number of samples N determines the frequency resolution Δf, or smallest resolvable frequency,

$$f_{\min} = \Delta f = \frac{1}{T} = \frac{1}{N\Delta t} = \frac{f_s}{N}. \qquad (2.23)$$

Lastly, M determines the variance of the set of periodograms $\{ S_n^{(m)} \}_{i=0}^{M-1}$ and hence the accuracy of the estimate S_n.

In practice, the ensemble realizations i are of course obtained sequentially, implying that one acquires a time series of data $x_n, n \in \{0, 1, \dots, NM-1\}$ and partitions these data into M sequences of length N. It becomes clear, then, that the Bartlett average (Equation 2.19) trades spectral resolution (larger N) for estimation accuracy (larger M) given the finite acquisition time $T = NM\Delta t$. An improvement in data efficiency can be achieved using Welch's method [22]. To see how, we first need to discuss spectral windowing.

2.2 Window functions

Partitioning a signal x_n into M sections $x_n^{(m)}$ of length N is mathematically equivalent to multiplying the signal with the rectangular *window*

11: Note that the limit of perfectly correlated noise, $S(\omega) \propto \delta(\omega)$, technically does *not* correspond to an ergodic process because $C(\tau) = \text{const.} \ \forall \tau \in (-\infty, \infty)$. In practice, this is always a mathematical idealization and the spectrum is actually better described by a nascent δ-function with a small but finite width.

12: By taking the limit $M \to \infty$ one recovers the true PSD,

$$\lim_{M \to \infty} S_n = S(\omega_n).$$

The continuum limit is as always obtained by sending $\Delta t \to 0, N \to \infty, N\Delta t = \text{const.}$

function given by[13]

$$w_n^{(m)} = \begin{cases} 1 & \text{if} \quad (m-1)N \le n < mN \quad \text{and} \\ 0 & \text{else} \end{cases} \tag{2.24}$$

so that $x_n^{(m)} = x_n w_n^{(m)}$. Now recall that multiplication and convolution are duals under the Fourier transform, implying that

$$\hat{x}_n^{(m)} = \hat{x}_n * \hat{w}_n^{(m)}, \tag{2.25}$$

where the Fourier representation of the rectangular window is given by[14]

$$\hat{w}_n^{(m)} = \hat{w}_n e^{-i(m-1/2)\omega_n T}, \tag{2.26}$$

$$\hat{w}_n = T \operatorname{sinc}\left(\frac{\omega_n T}{2}\right). \tag{2.27}$$

Figure 2.3 shows the unshifted rectangular window $\hat{w}_n$ in Fourier space. We can hence understand the Fourier spectrum of $x_n^{(m)}$ as sampling $\hat{x}_n$ with the probe $\hat{w}_n^{(m)}$. However, whereas in the continuum limit (see Sidenote 12) Equation 2.27 tends towards $\delta(\omega_n)$ and thus will produce a faithful reconstruction of the true spectrum, the finite sample rate f_s of discrete signals and observation length T induce finite frequency sampling and bandwidth of the probe as well as *sidelobes*.[15] These effects incur what is known as *spectral leakage* and *scalloping loss*, respectively, and lead to artifacts and deviations of the spectrum estimator S_n from the true spectrum $S(\omega_n)$ [16, 23].

For this reason, a plethora of *window functions* have been introduced to mitigate the effects of spectral leakage. Key properties of a window are the spectral bandwidth (center lobe width) and sidelobe amplitude between which there typically is a tradeoff.[16] A window frequently used in spectral analysis is the Hann window [25],

$$w_n^{(m)} = \begin{cases} \sin^2\left(\frac{\pi n}{N}\right) & \text{if} \quad (m-1)N \le n < mN \quad \text{and} \\ 0 & \text{else,} \end{cases} \tag{2.28}$$

with the Fourier representation of the unshifted window,

$$\hat{w}_n = \frac{T}{2} \operatorname{sinc}\left(\frac{\omega_n T}{2}\right) \frac{1}{1 - (\omega_n T/2\pi)^2} \tag{2.29}$$

shown in Figure 2.4. The favorable properties of the Hann window are apparent when compared to the rectangular window in Equation 2.27 and Figure 2.3; the sidelobes are quadratically suppressed while the center lobe is broadened by a factor of two.

Another favorable property of the Hann window is that $w_0^{(0)} = w_{N-1}^{(0)} = 0$. This suppresses detrimental effects arising from a possible discontinuity $(x_0^{(0)} \ne x_{N-1}^{(0)})$ at the edge of a data segment related to the discrete Fourier transform, which assumes periodic data.[17]
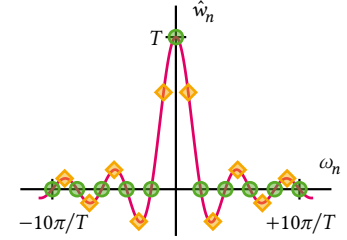
Figure 2.3: The Fourier representation of the rectangular window in continuous time (solid line) and for discrete frequencies $\omega_n = 2\pi n/T$ (circles). Introducing a phase shift, that is, shifting the window with respect to the signal in time, effectively shifts $\omega_n \to \omega_{n+\eta}$ as indicated for $\eta = 1/2$ (diamonds). This incurs scalloping loss.
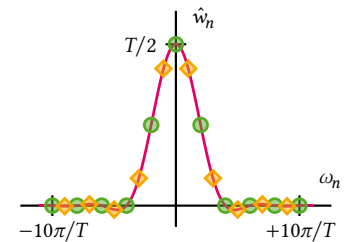
Figure 2.4: The Fourier representation of the Hann window in continuous time (solid line) and for discrete frequencies ω_n (circles). Diamonds indicate discrete sampling when the window completely out of phase with the signal (*cf.* Figure 2.3).
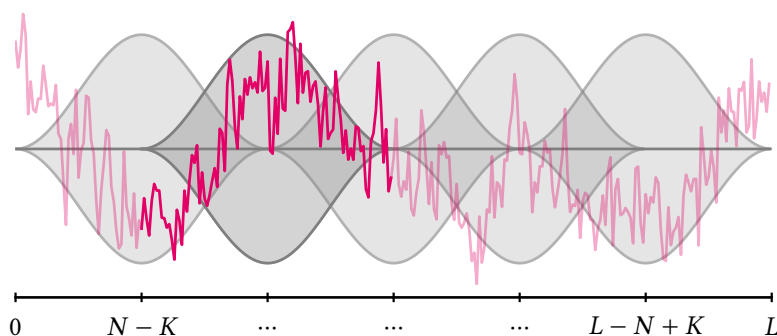
Figure 2.5: Illustration of Welch's method for spectrum estimation. The data (magenta) of length L is partitioned into $K = 2L/N - 1$ segments of length N. Each segment is multiplied with a window function (gray) which reduces spectral leakage and other artifacts. A finite overlap K between adjacent windows (gray) ensures efficient sample use.

2.3 Welch's method

Contemplating Equation 2.28, one might come to the conclusion that using a window such as this is not very data efficient in the sense that a large fraction of samples located at the edge of the window is strongly suppressed and hence does not contribute significantly to the spectrum estimate. To alleviate this lack of efficiency, one can introduce an overlap between adjacent data windows. That is, instead of partitioning the data x_n into M non-overlapping sections of length N, one shifts the mth window backward by mK with $K > 0$ the overlap. Finally, the periodogram (Equation 2.21) is computed for each window and subsequently averaged to obtain the spectrum estimator (Equation 2.19).

This method of spectrum estimation is known as Welch's method [22]. One can show [22] that the correlation between the periodograms of adjacent, overlapping windows is sufficiently small to avoid a biased estimate. The overlap naturally depends on the choice of window; a typical value for the Hann window $K = N/2$ with which one would obtain $M = 2L/N - 1$ windows for data of length L.[18]

18: Again neglecting integer arithmetic issues.

Figure 2.5 conceptually illustrates Welch's method for a trace of $1/f$ noise with $L = 300$ samples in total. Choosing the Hann window and an overlap of 50 % results in $M = 5$ segments for a window length of $N = 100$. The data in the second window is highlighted.

2.4 Parameters & Properties of the PSD

We are now in a position to discuss how the various parameters of a time series relate to both the physical parameters of the resulting spectrum estimate and to each other. To this end, we will go through the typical procedure of acquiring a spectrum estimate using Welch's method chronologically. Table 2.1 gives an overview of all relevant parameters.

To acquire data using some form of (digital) DAQ, one usually needs to specify two parameters first: the total number of samples to be acquired L, and the sample rate f_s. This results in a measurement of duration $T = L\Delta t$ where $\Delta t = f_\mathrm{s}^{-1}$ as previously mentioned. The choice of f_s already induces an upper bound on the first parameter characterizing the PSD estimate: the largest resolvable frequency $f_\mathrm{max} = f_\mathrm{s}/2$ (cf. Equation 2.22, but note that we allow f_max to be smaller than half the sample rate in anticipation of hardware constraints). Next, we choose a number of Welch averages, M, *i.e.*, data partitions, and their overlap, K. In doing so, one fixes the number of samples per partition N and thereby induces
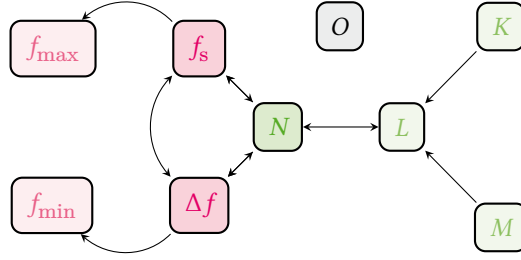
Table 2.1: Overview of spectrum estimation parameters. The parameters can be assigned into four groups: 1. DAQ parameters configuring the data acquisition device, 2. Welch parameters specifying the periodogram averaging, 3. Spectrum properties induced by the above, and 4. External parameters unrelated to the others.

1. DAQ PARAMETERS	
L	Total number of samples
f_s	Sample rate
2. WELCH PARAMETERS	
K	Number of overlap samples
N	Number of segment samples
M	Number of Welch segments
3. SPECTRUM PROPERTIES	
T	measurement of duration
f_min	Smallest resolvable frequency
f_max	Largest resolvable frequency
f_max	$f_\mathrm{s}/2$
4. MISCELLANEOUS PARAMETERS	
O	Number of outer averages

19: Technically, the smallest resolvable frequency in a fast Fourier transform (FFT) is zero, of course. But as data is typically detrended (a constant or linear trend subtracted) before computation of the periodogram, the smallest *meaningful* frequency is given by f_{min}.

the lower bound on the second parameter characterizing the PSD estimate: the frequency spacing $\Delta f = 1/N \le f_{min}$ (*cf.* Equation 2.23).[19] Finally, we can introduce a number of *outer* averages O, that is, the number of data batches that are acquired. While not directly related to Welch's method, choosing $O > 1$ can, for instance, help achieve a certain variance if the number of samples per batch, L, is limited by the data acquisition hardware, or simply allow for updating the spectrum estimate as data is being acquired. Figure 2.6 shows the relationships of the various parameters among each other. In Subsection 3.1.1, I lay out how these inter-dependencies are implemented in software.

To conclude this chapter, let us discuss some of the properties of stochastic processes and their autocorrelation function and PSD. Consider again the process $x(t)$. We say $x(t)$ is *Gaussian* if $x(t) \sim \mathcal{N}(\mu, \sigma^2) \, \forall t$, meaning that the value of $x(t)$ at a given point in time follows a normal distribution with some mean μ and variance σ^2 over multiple realizations of the process. In this case, its statistical properties are fully described by the autocorrelation function $C(\tau)$ and PSD $S(\omega)$. This is because only the first two cumulants of a Gaussian distribution are nonzero [26]. For the purpose of noise estimation, the assumption of Gaussianity is a rather weak one as the noise typically arises from a large ensemble of individual fluctuators and is therefore well approximated by a Gaussian distribution by the central limit theorem [27].[20] Even if $x(t)$ is not perfectly Gaussian, non-Gaussian contributions can be seen as higher-order contributions if viewed from the perspective of perturbation theory, and therefore the PSD still captures a significant part of the statistical properties. For this reason, the PSD is the central quantity of interest in noise spectroscopy. Let us just note at this point that techniques to estimate higher-order spectra (or *polyspectra*) exist [10, 31–33].

20: As an example, consider electronic devices, where voltage noise is thought to arise from a large number of defects and other charge traps in oxides being populated and depopulated at certain rates γ. The ensemble average over these so-called two-level fluctuators (TLFs) then yields the well-known $1/f$-like noise spectra [28, 29] (at least for a large density [30]).

For real signals $x(t) \in \mathbb{R}$, the autocorrelation function $C(\tau)$ is an even function, while for $x(t) \in \mathbb{C}$ its real part is even and its complex part odd. From this it immediately follows that for real $x(t)$ $S(\omega)$ is also an even function and one therefore distinguishes the *two-sided* PSD $S^{(2)}(\omega)$ defined over $\mathbb{R}$ from the *one-sided* PSD $S^{(1)}(\omega) = 2S^{(2)}(\omega)$ defined only over $\mathbb{R}^+$. Complex $x(t)$ such as those generated by LIAs after demodulation in turn have asymmetric, two-sided PSDs. In this chapter so far, we have implicitly employed the two-sided definition, but in the software package presented in Chapter 3, two-sided spectra are used only for complex data since they contain redundant information for real data.

Part II

CHARACTERIZATION AND IMPROVEMENTS OF A MILLIKELVIN CONFOCAL MICROSCOPE

Part III

Optical Measurements of Electrostatic Exciton Traps in Semiconductor Membranes

Part IV

A Filter-Function Formalism For Unital Quantum Operations

Author contributions — *This part of the present thesis is based to large extent on Reference [34], an early draft of which in turn was my Master's thesis [35], and as such contains text contributions from all three authors. Chapter 14 and* **??** *additionally contain results published in Reference [36], an early draft of which appears in Reference [37]. The first-order concatenation rule was originally derived by Pascal Cerfontaine.[a] He also conceived and performed initial calculations of the linearized quantum process expressed in terms of filter functions. Hendrik Bluhm[b] initiated the project and wrote the initial draft of the introduction. I recast the approach in the quantum operations formalism based on stochastic Liouville equations and the cumulant expansion, and derived expressions for the second-order terms, as well as developed an optimized expression for periodic Hamiltonians, derived quantities, discussed operator bases, and analyzed the computational efficiency. I also wrote the software package, performed all simulations, and developed all examples. Chapter 12 and* **??** *contain new results that I derived.*

Note — *In Reference [34], extensive use was made of Kubo's cumulant expansion [38]. Due to an error in Kubo's paper which was only pointed out several years later by Fox [39] and we were not aware of, those results turned out to be not exact as claimed but approximate [40].[1] We address this discrepancy in Chapter 12.*

I N the circuit model of quantum computing, computations are driven by applying time-local quantum gates. Any algorithm can be compiled using sequences of one- and two-qubit gates [41]. Ideal, error-free gates are represented by unitary transformations, so that simulating the action of an algorithm on an initial state of a quantum computer amounts to simple matrix multiplication. Real implementations are subject to noise that causes decoherence resulting in gate errors. If the noise is uncorrelated between gates, its effect can be described by quantum operations acting as linear maps on density matrices, even when several gates are concatenated. A closely related approach is the use of a master equation in Gorini-Kossakowski-Sudarshan-Lindblad (GKSL) form [42, 43], which governs the dynamics of density matrices under the influence of Markovian noise with a flat power spectral density.

Yet many physical systems used as hosts for qubits do not satisfy the condition of uncorrelated noise. One example frequently encountered in solid-state systems is that of $1/f$ noise, which in principle contains arbitrarily long correlation times. It emerges for instance as flux noise in superconducting qubits and electrical noise in quantum dot qubits [44–47]. Whereas simple approaches exist to treat for example quasistatic noise, which corresponds to perfectly correlated noise (*i.e.*, a spectrum with weight only at zero frequency), they cannot be applied to $1/f$ noise because of the wide distribution of correlation times it contains [12]. Thus, there is a gap in the mathematical descriptions of gate operations for noises with arbitrary power spectra that exist between the extremal cases

[34]: Hangleiter, Cerfontaine, and Bluhm (2021), *Filter-Function Formalism and Software Package to Compute Quantum Processes of Gate Sequences for Classical Non-Markovian Noise*

[35]: Hangleiter (2019), *Filter Function Formalism for Unitary Quantum Operations*

[36]: Cerfontaine, Hangleiter, and Bluhm (2021), *Filter Functions for Quantum Processes under Correlated Noise*

[37]: Cerfontaine (2019), *High-Fidelity Single- and Two-Qubit Gates for Two-Electron Spin Qubits*

a: Then at RWTH Aachen University and Forschungszentrum Jülich GmbH.

b: RWTH Aachen University and Forschungszentrum Jülich GmbH.

[40]: Hangleiter, Cerfontaine, and Bluhm (2024), *Erratum: Filter-function Formalism and Software Package to Compute Quantum Processes of Gate Sequences for Classical Non-Markovian Noise [Phys. Rev. Research 3, 043047 (2021)]*

1: Unfortunately, the error has proliferated through the literature and proves quite pervasive despite the significant amount of time that has passed since it was first discovered. Recent examples include Reference 33. One may only speculate if this is because of the 14 years that passed between the original publication and the correction, the lack of an erratum once the mistake had been discovered, or simply because of Kubo's fame. In any case, it might serve as a cautionary tale and possibly an impetus to a less static publication system that allows, for example, cross-linking commentaries and critiques.

of perfectly flat (white) and sharply peaked (quasistatic) spectra. To capture experimentally relevant effects important to understand the capabilities of quantum computing systems, a universally applicable formalism is hence desirable. For example, one may expect the fidelity requirements for quantum error correction to be more stringent for correlated noise as errors of different gates can interfere constructively [48]. On the other hand, it might also be possible to use correlation effects to one's benefit, attenuating decoherence by cleverly constructing the gate sequences in algorithms.

As experimental platforms begin to approach fidelity limits set by employing primitive pulse schemes [46, 49, 50] and detailed knowledge about noise sources and spectra in solid-state systems becomes available [11, 51, 52], control pulse optimizations tailored towards specific systems will be required to further push fidelities beyond the error correction threshold [53, 54]. This calls for flexible and generically applicable tools as a basis for the numerical optimization of pulses as well as the detailed analysis of the quantum processes they effect. In order to obtain a useful description also for gate operations that decouple from leading orders of noise, such as dynamically corrected gates (DCGs) [55], beyond leading order results are required.

In Reference 36 we presented a formalism based on filter functions and the Magnus expansion (ME) that addresses these needs and limitations of the canonical master equation approach for correlated noise. Specifically, we showed how process descriptions can be obtained perturbatively for arbitrary classical noise spectra and derived a concatenation rule to obtain the filter function of a sequence of gates from those of the individual gates. This work generalizes and extends these results.

Filter functions (FFs) were originally introduced to describe the decay of phase coherence under dynamical decoupling (DD) sequences [56–59] consisting of wait times and perfect π-pulses. The formalism facilitated recognizing these sequences as band-pass filters that allow for probing the environmental noise characteristics of a quantum system through noise spectroscopy [7, 9, 52, 60] or optimizing sequences to suppress specific noise bands [52, 61–63]. It can also be extended to fidelities of gate operations for single [64, 65] or multiple [66, 67] qubits using the ME [68, 69] as well as more general DD protocols [70]. The works by Green et al. [65] and Clausen, Bensky, and Kurizki [71] also introduced the notion of the control matrix as a quantity closely related to the canonical filter function that is convenient for calculations. In this context, the formalism's capability to predict fidelities of gate implementations has been identified and experimentally tested [63, 65, 72, 73]. More recently, it has also proved useful in assessing the performance requirements for classical control electronics [74].

While analytical approaches allow for the calculation of filter functions of arbitrary quantum control protocols in principle, it is in practice often a tedious task to determine analytical solutions to the integrals involved if the complexity of the applied wave forms goes beyond simple square pulses or extends to multiple qubits. Moreover, one does not always have a closed-form expression of the control at hand, such as is the case for numerically optimized control pulses. This calls for a numerical approach which, while giving up some of the insights an analytical form offers, is universally applicable and eliminates the need for laborious analytical calculations.

Here, we build and extend upon our work of Reference 36 and that of Reference 65 to show that the formalism can be recast within the frame-

work of stochastic Liouville equations by means of the cumulant expansion [38, 39, 75, 76]. For Gaussian noise commuting with the control, this entails exact results for the quantum process of an arbitrary control operation using only first and second order terms of the ME [68]. If the noise is Gaussian but in general non-commuting, the cumulant expansion does not terminate [39], but we show that the truncation still yields highly accurate results except in the ultralow-frequency regime by computing the exact filter function from random sampling. Moreover, due to the fact that the ME retains the algebraic structure of the expanded quantity [69] we are able to separate incoherent and coherent contributions to the quantum process. We give explicit methods to evaluate these terms for piecewise-constant control pulses. Moreover, we show that the formalism naturally lends itself as a tool for numerical calculations and present the `filter_functions` Python software package that enables calculating the filter function of arbitrary, piecewise constant defined pulses [77]. On top of providing methods to handle individual quantum gates, the package also implements the concatenation operation as well as parallelized execution of pulses on different groups of qubits, allowing for a highly modular and hence computationally powerful treatment of quantum algorithms in the presence of correlated noise. Given an arbitrary, classical noise spectral density, it can be used to calculate a matrix representation of the error process. From this matrix one can extract average gate fidelities, transition probabilities, and leakage rates as we derive below. To simplify adaptation the software's application programming interface (API) is strongly inspired by and compatible with QuTiP [78] as well as qopt [79]. This allows users to use these packages in conjunction. Assessing the computational performance, we show that our method outperforms Monte Carlo (MC) simulations for single gates. New analytical results applicable to periodic Hamiltonians and employing the concatenation property make this advantage even more pronounced for sequences of gates. To highlight the main software features, we show example applications below.

We provide this package in the expectation that it will be a useful tool for the community. Besides recasting and expanding on our earlier introduction of the formalism in Reference 36, the present work is intended to provide an overview of the software and its capabilities. It is structured as follows: In Chapter 11 we derive a closed-form expression for unital quantum operations in the presence of non-Markovian Gaussian noise and lay out how it may be evaluated using the filter-function formalism. We review the concatenation of quantum operations shown in Reference 36 and furthermore adapt the method by Green et al. [65] to calculate the filter function of an arbitrary control sequence numerically. We will specifically focus on computational aspects of the formalism and lay out how to compute various quantities of interest. Moreover, we classify its computational complexity for calculating average gate fidelities and remark on simplifications that allow for drastic improvements in performance in certain applications. In Chapter 12, we validate the truncation of the cumulant expansion after the second order using a random sampling approach to compute the exact filter functions of the noisy quantum process for Gaussian noise. In Chapter 13, we then introduce the `filter_functions` software package by outlining the programmatic structure and giving a brief overview over the API. Lastly, in Chapter 14, we show the application of the software by means of four examples that highlight various features of the formalism and its implementation. Therein, we first demonstrate that the formalism can predict average gate fidelities for complex two-qubit quantum gates in agreement with computationally much more costly MC calculations. Next, we

show how it can be applied to periodically driven systems to efficiently analyze Rabi oscillations. We finally establish the formalism's ability to predict deviations from the simple concatenation of unitary gates for sequences and algorithms in the presence of correlated noise by simulating a randomized benchmarking (RB) experiment as well as assembling a quantum Fourier transform (QFT) circuit from numerically optimized gates. We conclude by briefly remarking on possible future application and extension of our method in Chapter 15.

Throughout this part we will denote Hilbert-space operators by Roman font, *e. g. U*, and quantum operations and their representations as transfer matrices in Liouville space by calligraphic font, *e. g. $\mathcal{U}$*, which we also use for the control matrix $\tilde{\mathcal{B}}$ to emphasize its innate connection to a transfer matrix. For consistency, a unitary quantum operation will share the same character as the corresponding unitary operator. An operator in the interaction picture will furthermore be designated by an overset tilde, *e. g.* $\tilde{H} = U^{\dagger}HU$ with U the unitary operator defining the co-moving frame. Definitions of new quantities on the left and right side of an equality are denoted by := and =:, respectively. We use a central dot (•) as a placeholder in some definitions of abstract operators such as the Liouvillian, denoted by $\mathcal{L} := [H, \bullet]$, which is to be understood as the commutator of the corresponding Hamiltonian H and the operator that $\mathcal{L}$ acts on. The identity matrix is denoted by $\mathbb{1}$ and its dimension always inferred from context. Furthermore, we will use Greek letters for indices that correspond to noise operators in order to distinguish them clearly from those that correspond to basis or matrix elements. Lastly, we work in units where $\hbar = 1$.

Filter-function formalism for unital quantum operations

Wᴇ begin the mathematical part by showing how a superoperator matrix representation of the error process, the *error transfer matrix*, of a unital quantum operation can be computed from the control matrix of the pulse implementing the operation. The control matrix relates the operators through which noise couples into the system to a set of basis operators in the interaction picture and we detail how it can be calculated in a relatively efficient manner for two different situations. First, we consider a sequence of gates whose control matrices have been precomputed. Second, we lay out how the control matrix can be obtained from scratch under the assumption of piecewise-constant control, which is often convenient for approximating continuous pulse shapes. Other wave forms can be dealt with analogously by solving the corresponding integrals. We then move on to show how several quantities of interest can be extracted and present optimized strategies for computing the central objects of the formalism.

11.1 Transfer matrix representation of quantum operations

11.1.1 Brief review of quantum operations and superoperators

The quantum operations formalism provides a general framework for the description of open quantum systems [80, 81]. It forms the mathematical basis for quantum process tomography (QPT) [82, 83] as well as gate set tomography (GST) [84, 85] and has also been extensively employed in the context of RB [86, 87]. Several different representations of quantum operations exist. While all of them are equivalent one typically chooses the most convenient for the problem at hand. For an overview of the most commonly used representations see Reference 85 and for matrix representations in particular Reference 88 and the references therein. In this work we employ the Liouville representation, to the best of our knowledge first formalized by Fano [89], to profit from its simple properties under composition. It is also known as the transfer matrix representation and we will use the terms interchangeably below. We now briefly review the concept and refer the reader to the literature for further details. Concretely, the Liouville representation of an operation $\mathcal{E} : \rho \to \mathcal{E}(\rho)$ acting on density operators in a Hilbert space $\mathcal{H}$ of dimension d is given by

$$\mathcal{E}_{ij} \doteq \mathrm{tr}\!\left(C_i^\dagger \mathcal{E}(C_j)\right) \tag{11.1}$$

with an operator basis $\mathsf{C} = \{C_0, C_1, \dots, C_{d^2-1}\}$ for the space of linear operators over $\mathcal{H}$, $\mathsf{L}(\mathcal{H})$, orthonormal with respect to the Hilbert-Schmidt product $\langle A, B \rangle := \mathrm{tr}\!\left(A^\dagger B\right)$. In the case that the operator basis corresponds to the Pauli matrices Equation 11.1 is known as the Pauli transfer matrix (PTM). The operation $\mathcal{E}$ is thus associated with a $d^2 \times d^2$ matrix in *Liouville space* $\mathscr{L}$ that describes its action as the degree to which the jth basis element is mapped onto the ith. On $\mathscr{L}$ one can identify a set of basis kets $\{|C_i\rangle\!\rangle\}_{i=0}^{d^2-1} = \{|i\rangle\!\rangle\}_{i=0}^{d^2-1}$ isomorphic to the operators C_i (and correspondingly

bras $\langle\!\langle i|$ to the adjoint $C_i^\dagger$) as well as the inner product $\langle\!\langle i|j\rangle\!\rangle = \langle C_i, C_j\rangle$. As the vectors $|i\rangle\!\rangle$ form an orthonormal basis, any operator on $\mathscr{H}$ can be written as a vector on $\mathscr{L}$, $|A\rangle\!\rangle = \sum_i |i\rangle\!\rangle \langle\!\langle i|A\rangle\!\rangle$, whereas a superoperator on $\mathscr{H}$ becomes a matrix on $\mathscr{L}$, see Equation 11.1. It can then be shown that density operators represented by vectors are propagated by transfer matrices so that the action of a quantum operation $\mathcal{E}$ on a density operator ρ is given by $|\mathcal{E}(\rho)\rangle\!\rangle = \mathcal{E}\,|\rho\rangle\!\rangle = \sum_{ij} |i\rangle\!\rangle \langle\!\langle i|\mathcal{E}|j\rangle\!\rangle \langle\!\langle j|\rho\rangle\!\rangle$. Thus, the composition of two operations $\mathcal{E}_1$ and $\mathcal{E}_2$ corresponds to matrix multiplication in Liouville space, $[\mathcal{E}_2 \circ \mathcal{E}_1]_{ik} = \sum_j [\mathcal{E}_2]_{ij}[\mathcal{E}_1]_{jk}$, a property which makes the representation particularly attractive for sequences of operations. Although from a numerical perspective the computational complexity scales unfavorably with the system dimension d (*cf.* Section 11.9), we will employ the Liouville representation for its transparent interpretation and concise behavior under composition in the following analytical considerations. Lastly, we note that for $C_0 \propto \mathbb{1}$, trace-preservation and unitality are encoded in the relations $\mathcal{E}_{0j} = \delta_{0j}$ and $\mathcal{E}_{j0} = \delta_{j0}$, respectively.

11.1.2 Liouville representation of the error channel

We will now derive an expression for the quantum process of a quantum gate in the presence of arbitrary classical noise. As a single realization of a classical noise generates strictly unitary dynamics, we will be interested in the expectation value of the dynamics over many such realizations, which will lead to a quantum process including decoherence. If the noise is additionally Gaussian and commutes with the control, these results are exact and therefore apply without restrictions to arbitrarily large noise strength as well as to gates that partially decouple from noise. For such DCGs or DD sequences [55, 59] higher order terms can become dominant. Non-commuting noise leads to corrections at higher orders that we investigate in Chapter 12 [40]. In the case that the environment is not strictly Gaussian, our approach becomes perturbative and we recover the results presented in Reference 36. As most of our discussion later on in this part will focus on the approximation neglecting coherent errors, readers not interested in the full generality may refer to that publication for a less general but perhaps more accessible derivation and skip ahead to Section 11.2.

The difference is that in Reference 36, the Magnus expansion is applied to the solution of the Schrödinger equation, whereas the approach presented here is based on the theory of stochastic Liouville equations and the cumulant expansion [38, 75]. In the filter function context, the cumulant expansion has been used to express the decay of the off-diagonal terms of a single-qubit density matrix in Reference 59. More recently, Paz-Silva and Viola [70] employed it in conjunction with the ME to obtain the matrix elements of the perturbed density operator after a time T of noisy evolution. In Reference 90, the authors made use of the cumulant expansion and stochastic Liouville equations for the purpose of gate optimization. Here, we combine different aspects of these works and make the connection to the quantum operations formalism by determining the noise-averaged error propagator in the Liouville representation. This form completely characterizes the error process and hence allows for detailed insight into the decoherence mechanisms of the operation.

Concretely, we consider a system described by the stochastic Hamilto-

[40]: Hangleiter, Cerfontaine, and Bluhm (2024), *Erratum: Filter-function Formalism and Software Package to Compute Quantum Processes of Gate Sequences for Classical Non-Markovian Noise [Phys. Rev. Research 3, 043047 (2021)]*

nian

$$H(t) = H_c(t) + H_n(t), \tag{11.2}$$

$$H_n(t) = \sum_\alpha b_\alpha(t) B_\alpha(t). \tag{11.3}$$

$H_c(t)$ is implemented by the experimentalist to generate the desired control operation during the time $t \in [0, \tau]$ and $H_n(t)$ describes classical fluctuating noise environments $b_\alpha(t) \in \mathbb{R}$ that couple to the quantum system via the Hermitian noise operators $B_\alpha(t) \in \mathsf{L}(\mathscr{H})$. These may carry a general, deterministic time dependence and without loss of generality, we can require them to be traceless since any contributions proportional to the identity do not contribute to noisy evolution in any case.[1] The $b_\alpha(t)$ are random variables drawn from (not necessarily Gaussian) distributions with zero mean that are assumed to be independent and identically distributed (i.i.d.) both with respect to repetitions of the experiment. Note that this concept of independence does not preclude correlations between different noise sources $\alpha \neq \beta$ nor between one noise source at different times $t \neq t'$, but only serves to obtain a well-defined ensemble average. Lastly, to be able to later on relate the correlation functions of the $b_\alpha(t)$ to their spectral density, we require the noise fields to be wide-sense stationary, meaning that their correlation function depends only on the time difference.[2]

For noise operators without explicit time dependence, Equation 11.3 constitutes a universal decomposition as can be seen by choosing the B_α from an orthonormal basis for $\mathsf{L}(\mathscr{H})$. To motivate the time-dependent form of Equation 11.3, assume the true Hamiltonian is a function of a set of noisy parameters $\tilde{\boldsymbol{\lambda}}(t) = \boldsymbol{\lambda}(t) + \boldsymbol{\delta\lambda}(t)$ where $\boldsymbol{\delta\lambda}(t) = \text{vec}(\{b_\alpha(t)\}_\alpha)$ are the stochastic variables. Expanding the Hamiltonian in an orthonormal operator basis yields $H(\tilde{\boldsymbol{\lambda}}(t)) = \sum_\alpha f_\alpha(\boldsymbol{\lambda}(t), \boldsymbol{\delta\lambda}(t)) B_\alpha$. In general, however, the expansion coefficients f_α will be arbitrary functions of both the deterministic parameters $\boldsymbol{\lambda}(t)$ and the stochastic noises $\boldsymbol{\delta\lambda}(t)$, which prohibits a factorized form like Equation 11.3. We can address this problem by first expanding H around $\boldsymbol{\lambda}(t)$ for small fluctuations $\boldsymbol{\delta\lambda}(t)$. Then, the Hamiltonian approximately becomes $H(\tilde{\boldsymbol{\lambda}}(t)) \approx H(\boldsymbol{\lambda}(t)) + \boldsymbol{\delta\lambda}(t) \cdot \nabla_\lambda H(\boldsymbol{\lambda}(t))$, where we can define the control Hamiltonian as $H_c(t) := H(\boldsymbol{\lambda}(t))$. Expanding the second term in the operator basis now results in the form (11.3) for the noise Hamiltonian as it is linear in $\boldsymbol{\delta\lambda}(t)$ and the deterministic time dependence is contained in $\nabla_\lambda H(\boldsymbol{\lambda}(t))$ alone.

This permits us to model complex relations between physical noise sources and the noise operators that capture the coupling to the quantum system, arising for example through control hardware or effective Hamiltonians obtained from *e.g.* Schrieffer-Wolff transformations. While the linearization is in most cases an approximation, it does not impose significant constraints since the noise is typically weak compared to the control.[3] As an example, we could capture a dependence of the device sensitivity on external controls (see also Reference 66). In a widely used setting electrons confined in solid-state quantum dots are manipulated using the exchange interaction J that depends non-linearly on the potential difference ϵ between two dots. Since the dominant physical noise source affecting this control is charge noise, one could include the effect on $J(\epsilon)$ to first order with $s_\epsilon(t) = \partial J(\epsilon(t))/\partial\epsilon(t)$ so that $H_n(t) = b_\epsilon(t) B_\epsilon(t) = b_\epsilon(t) s_\epsilon(t) B_\epsilon$ for some operator B_ϵ which represents the exchange coupling.

We proceed in our derivation by noting that the control Hamiltonian H_c

gives rise to the noise-free Liouville–von Neumann equation

$$\frac{\mathrm{d}\rho(t)}{\mathrm{d}t} = -i[H_{\mathrm{c}}(t), \rho(t)] = -i\mathcal{L}_{\mathrm{c}}(t)\rho(t) \tag{11.4}$$

on the Hilbert space $\mathcal{H}$ with the Liouvillian superoperator $\mathcal{L}_{\mathrm{c}}(t)$ representing the control. Analogous to the Schrödinger equation we may also write this differential equation in terms of time evolution superoperators (superpropagators), $\mathrm{d}\mathcal{U}_{\mathrm{c}}(t)/\mathrm{d}t = -i\mathcal{L}_{\mathrm{c}}(t)\mathcal{U}_{\mathrm{c}}(t)$ where the action of $\mathcal{U}_{\mathrm{c}}$ on a state ρ is to be understood as $\mathcal{U}_{\mathrm{c}}: \rho \to U_{\mathrm{c}}\rho U_{\mathrm{c}}^{\dagger}$ with U_{c} the usual time evolution operator satisfying the corresponding Schrödinger equation. This allows us to write the superpropagator for the total Liouvillian $\mathcal{L} = \mathcal{L}_{\mathrm{c}} + \mathcal{L}_{\mathrm{n}}$ as $\mathcal{U}(t) = \mathcal{U}_{\mathrm{c}}(t)\tilde{\mathcal{U}}(t)$ where the unitary error superpropagator $\tilde{\mathcal{U}}(t)$ contains the effect of a specific noise realization in Equation 11.3. Next, we transform the noise Liouvillian $\mathcal{L}_{\mathrm{n}}$ to the interaction picture with respect to the control Liouvillian $\mathcal{L}_{\mathrm{c}}$ so that $\tilde{\mathcal{U}}(t)$ satisfies the modified Liouville–von Neumann equation

$$\frac{\mathrm{d}\tilde{\mathcal{U}}(t)}{\mathrm{d}t} = -i\tilde{\mathcal{L}}_{\mathrm{n}}(t)\tilde{\mathcal{U}}(t), \tag{11.5}$$

$$\tilde{\mathcal{L}}_{\mathrm{n}}(t) = \mathcal{U}_{\mathrm{c}}^{\dagger}(t)\mathcal{L}_{\mathrm{n}}(t)\mathcal{U}_{\mathrm{c}}(t). \tag{11.6}$$

Equation 11.5 may be formally solved using the Magnus expansion [68] so that at time $t = \tau$

$$\tilde{\mathcal{U}}(\tau) = \exp\{-i\tau\mathcal{L}_{\mathrm{eff}}(\tau)\} \tag{11.7}$$

with $\mathcal{L}_{\mathrm{eff}}(\tau) = \sum_{n=1}^{\infty} \mathcal{L}_{\mathrm{eff},n}(\tau)$. A sufficient criterion for the convergence of the expansion is given by Moan, Oteo, and Ros [91] as $\int_0^{\tau} \mathrm{d}t \|\tilde{\mathcal{L}}_{\mathrm{n}}(t)\| < \pi$ where $\|\bullet\| = \sqrt{\langle \bullet, \bullet \rangle}$ is the Frobenius (Hilbert-Schmidt) norm. The first and second terms of the ME are given by [68, 69]

$$\mathcal{L}_{\mathrm{eff},1}(\tau) = \frac{1}{\tau} \int_0^{\tau} \mathrm{d}t\, \tilde{\mathcal{L}}_{\mathrm{n}}(t), \tag{11.8a}$$

$$\mathcal{L}_{\mathrm{eff},2}(\tau) = -\frac{i}{2\tau} \int_0^{\tau} \mathrm{d}t_1 \int_0^{t_1} \mathrm{d}t_2 \left[\tilde{\mathcal{L}}_{\mathrm{n}}(t_1), \tilde{\mathcal{L}}_{\mathrm{n}}(t_2)\right]. \tag{11.8b}$$

The nth term of the expansion contains n factors of the noise variables $b_\alpha(t)$ and scales with n factors of the control duration τ, suggesting that higher-order terms can be neglected if their product is small. In the Bloch sphere picture this corresponds to requiring that the angle by which the Bloch vector is rotated away from its intended trajectory due to the noise be small. Below, we will use the parameter ξ to denote the magnitude of this deviation. It is properly defined in **??** where also bounds for the convergence of the ME are discussed. Here, we only state that $\mathcal{L}_{\mathrm{eff},n} \sim \xi^n$ (see also Reference 65).

We have suggestively written the ME in terms of an effective Liouvillian $\mathcal{L}_{\mathrm{eff}} = [H_{\mathrm{eff}}, \bullet]$ to interpret it as the generator of a *time*-averaged evolution of a single noise realization up to time τ. In order to obtain the *ensemble*-averaged evolution of many realizations of the stochastic Hamiltonian in Equation 11.3, we apply the cumulant expansion to $\tilde{\mathcal{U}}$ (see also Refences 29 and 92),

$$\langle \tilde{\mathcal{U}}(\tau) \rangle = \langle \exp\{-i\tau\mathcal{L}_{\mathrm{eff}}(\tau)\} \rangle =: \exp \mathcal{K}(\tau) \tag{11.9}$$

with $\langle \bullet \rangle$ denoting the ensemble average[4] and the cumulant function [38]

4: The ensemble average represents the expectation value over identical repetitions of an operation in an experiment. It can be taken to be a spatial ensemble of many identical systems, *e.g.* an NMR system, or, for ergodic systems, a time ensemble of a single system under stationary noise as would be the case for a single spin measured repeatedly, for instance.

$$\mathcal{K}(\tau) = \sum_{k=1}^{\infty} \frac{(-i\tau)^k}{k!} \left\langle \mathcal{L}_{\text{eff}}(\tau)^k \right\rangle_{\text{c}} \tag{11.10}$$

$$= \sum_{k=1}^{\infty} \frac{(-i\tau)^k}{k!} \left\langle \left[\sum_{n=1}^{\infty} \mathcal{L}_{\text{eff},n}(\tau) \right]^k \right\rangle_{\text{c}} . \tag{11.11}$$

The notation $\langle \cdot \rangle_{\text{c}}$ denotes the cumulant average which prescribes a certain averaging operation. The first cumulant of a set of random variables $\{X_i(t)\}_i$ is simply the expectation value, $\langle X_i(t)\rangle_{\text{c}} = \langle X_i(t)\rangle$, whereas the second cumulant corresponds to the covariance, $\langle X_i(t)X_j(t)\rangle_{\text{c}} = \langle X_i(t)X_j(t)\rangle - \langle X_i(t)\rangle \langle X_j(t)\rangle$. Remarkably, third and higher-order cumulants vanish for commuting Gaussian processes [10, 75],[5] making Equation 11.11 exact by truncating the sums already at $k = 2$ and $n = 2$. In this case, the convergence radius of the ME becomes infinite. In the following, we assume this truncation to be a good approximation of the exact dynamics. We investigate this assumption in more detail in Chapter 12 for non-commuting Gaussian noise. For non-Gaussian noise, we note that the approximation error depends on the degree of non-Gaussianity. Due to the central-limit theorem, we may expect corrections to become smaller the more two-level fluctuators (TLFs), whose individual statistics are highly non-Gaussian, couple to a qubit, for example. In general, all we can say is that the error is of $\mathcal{O}(\xi^2)$ and higher order terms include both higher orders of the ME and the cumulant expansion.

We continue by pointing out that the terms with $k = n = 2$ involve fourth-order cumulants and are thus of $\mathcal{O}(\xi^4)$. Since furthermore we assume that the noise fields $b_\alpha(t)$ have zero mean, also the terms with $k = n = 1$ vanish and $\langle X_i(t)X_j(t)\rangle_{\text{c}} = \langle X_i(t)X_j(t)\rangle$. We can hence write the cumulant function succinctly as

$$\mathcal{K}(\tau) = -i\tau \left\langle \mathcal{L}_{\text{eff},2}(\tau) \right\rangle - \frac{\tau^2}{2} \left\langle \mathcal{L}_{\text{eff},1}(\tau)^2 \right\rangle. \tag{11.12}$$

Equations 11.9 and 11.12 allow us to compute the full quantum process $\langle \tilde{\mathcal{U}} \rangle : \rho \to \langle \tilde{\mathcal{U}}(\rho) \rangle$ for noise with arbitrary spectral density. Inspecting Equation 11.12, we observe that the first term is anti-Hermitian as it is a pure Magnus term[6] and thus generates unitary, coherent time evolution. Conversely, the second term is Hermitian and thus generates decoherence.[7] The former is more difficult to compute than the latter because the second order of the ME, Equation 11.8b, contains nested time integrals. Arguments can be made [36], however, that for single gates in an experimental context the coherent errors captured by this term can be calibrated out to a large degree [93, 94]. Moreover, many of the central quantities of interest that can be extracted from the quantum process, among which are gate fidelities and certain measurement probabilities, are functions of only the diagonal elements of $\mathcal{K}$. By virtue of the antisymmetry of the second order terms, they do not contribute to these quantities to leading order as we show in Section 11.4.

While we will also lay out how to compute the second order, our discussion will therefore focus on contributions from the incoherent term below. As it turns out, this term can be computed using a filter-function formalism based on that by Green et al. [65]. To see this, we insert the explicit forms of the ME given in Equation 11.8 and the noise Hamiltonian given in Equation 11.3 into Equation 11.12. Together with $[\mathcal{L}, \mathcal{L}'] =$

5: By *commuting* noise we mean that $[H_{\text{c}}(t), H_{\text{n}}(t)] = 0 \forall t$. The prototypical example of this is the pure-dephasing Hamiltonian $H(t) = [\Omega(t) + \delta\omega(t)] \sigma_z/2$.

6: Remember that the ME preserves algebraic structure to every order.

7: In the Liouville representation, the first term is an antisymmetric matrix that generates a rotation and the second a symmetric matrix that generates a deformation of the generalized, $d^2 - 1$-dimensional Bloch sphere.

$[[H, H'], \bullet]$ and $\mathcal{L}\mathcal{L}' = [H, [H', \bullet]]$, we find that

$$\mathcal{K}(\tau) = -\frac{1}{2} \sum_{\alpha\beta} \left(\int_0^\tau dt_1 \int_0^{t_1} dt_2 \, \langle b_\alpha(t_1) b_\beta(t_2) \rangle \left[\left[\tilde{B}_\alpha(t_1), \tilde{B}_\beta(t_2) \right], \bullet \right] \right.$$

$$\left. + \int_0^\tau dt_1 \int_0^\tau dt_2 \, \langle b_\alpha(t_1) b_\beta(t_2) \rangle \left[\tilde{B}_\alpha(t_1), \left[\tilde{B}_\beta(t_2), \bullet \right] \right] \right), \quad (11.13)$$

where $\tilde{B}_\alpha(t) = U_c^\dagger(t) B_\alpha(t) U_c(t)$ are the noise operators of Equation 11.3 in the interaction picture. $\langle b_\alpha(t_1) b_\beta(t_2) \rangle$ is the cross-correlation function of noise sources α and β which we will later relate to the spectral density. For now, we stay in the time domain and introduce an orthonormal and Hermitian operator basis for the Hilbert space $\mathscr{H}$ to define the Liouville representation,

$$\mathsf{C} = \left\{ C_k \in \mathsf{L}(\mathscr{H}) : C_k^\dagger = C_k \text{ and } \mathrm{tr}(C_k C_l) = \delta_{kl} \right\}_{k=0}^{d^2-1}, \quad (11.14)$$

where we choose $C_0 = d^{-1/2} \mathbb{1}$ for convenience so that the remaining elements are traceless. In order to separate the commutators from the time-dependence and hence the integral in Equation 11.13, we expand the noise operators in this basis so that

$$\tilde{B}_\alpha(t) =: \sum_k \tilde{\mathcal{B}}_{\alpha k}(t) C_k. \quad (11.15)$$

The expansion coefficients $\tilde{\mathcal{B}}_{\alpha k}(t) \in \mathbb{R}$ are given by the inner product of a noise operator in the interaction picture on the one hand and a basis element on the other:

$$\tilde{\mathcal{B}}_{\alpha k}(t) = \langle \tilde{B}_\alpha(t), C_k \rangle = \mathrm{tr}\left(U_c^\dagger(t) B_\alpha(t) U_c(t) C_k \right). \quad (11.16)$$

In line with Green et al. [65], we call these coefficients the control matrix (see also Refences 95 and 71). In the transfer matrix (superoperator) picture we can take up the following interpretation for the control matrix by virtue of the cyclicity of the trace: it describes a mapping of a state, represented by the basis element C_k and subject to the control operation $\mathcal{U}_c(t) : C_k \to U_c(t) C_k U_c^\dagger(t)$, onto the noise operator $B_\alpha(t)$. That is, we can write the αth row of the control matrix as $\langle\!\langle \tilde{B}_\alpha(t) | = \langle\!\langle B_\alpha(t) | \, \mathcal{U}_c(t)$. In this connection lies the power of the FF formalism as will become clear shortly; we can first determine the ideal evolution without noise and subsequently evaluate the error process by linking the unitary control operation to the noise operators.

Having expanded the noise operators in the basis C, we can already anticipate that upon substituting them, Equation 11.13 will separate into a time-dependent part involving on one hand the control matrix and cross-correlation functions and on the other a time-independent part involving commutators of basis elements. This will simplify our calculations in the following. To see this, we recall the definition of the Liouville representation in Equation 11.1 and apply it to the cumulant function so that $\mathcal{K}_{ij} = \mathrm{tr}\left(C_i \mathcal{K}[C_j] \right) \in \mathcal{L}$, where the notation $\mathcal{K}[C_j]$ means substituting C_j for the placeholder $\bullet$ in the commutators in Equation 11.13 and we suppressed the time argument for legibility. Finally, we insert the expanded noise operators given by Equation 11.15 and obtain the Liouville representation of the cumulant function,

$$\mathcal{K}_{ij}(\tau) =: -\frac{1}{2} \sum_{\alpha\beta} \sum_{kl} \left(f_{ijkl} \Delta_{\alpha\beta,kl} + g_{ijkl} \Gamma_{\alpha\beta,kl} \right). \quad (11.17)$$

Here, we captured the ordering of the noise operators due to the commutators in Equation 11.13 in the coefficients f_{ijkl} and g_{ijkl}. These are trivial functions of the fourth order trace tensor[8]

$$T_{ijkl} = \text{tr}\big(C_i C_j C_k C_l\big) \tag{11.18}$$

given by

$$f_{ijkl} = T_{klji} - T_{lkji} - T_{klij} + T_{lkij} \quad \text{and} \tag{11.19a}$$

$$g_{ijkl} = T_{klji} - T_{kjli} - T_{kilj} + T_{kijl}. \tag{11.19b}$$

Furthermore, we introduced the frequency (Lamb) shifts Δ and decay amplitudes Γ which contain all information on the noise and qubit dynamics as captured by the control matrix $\tilde{\mathcal{B}}(t)$:

$$\Delta_{\alpha\beta,kl} = \int_0^\tau dt_1 \int_0^{t_1} dt_2 \left\langle b_\alpha(t_1) b_\beta(t_2) \right\rangle \tilde{\mathcal{B}}_{\alpha k}(t_1) \tilde{\mathcal{B}}_{\beta l}(t_2), \tag{11.20}$$

$$\Gamma_{\alpha\beta,kl} = \int_0^\tau dt_1 \int_0^\tau dt_2 \left\langle b_\alpha(t_1) b_\beta(t_2) \right\rangle \tilde{\mathcal{B}}_{\alpha k}(t_1) \tilde{\mathcal{B}}_{\beta l}(t_2). \tag{11.21}$$

The frequency shifts Δ correspond to the first term in Equation 11.12, hence incurring coherent errors, *i.e.* generalized axis and overrotation errors. They reflect a perturbative correction to the quantum evolution due to a change of the Hamiltonian at two points in time, and thus time ordering matters. Conversely, the decay amplitudes Γ correspond to the second term and capture the decoherence. These terms are due to an incoherent average that only takes classical correlations into account, so that time ordering does not play a role. Note that Equation 4 from Reference 36 is obtained from Equations 11.9 and 11.17 by expanding the exponential to linear order and neglecting the second order terms Δ.

For a single qubit and C the Pauli basis one can make use of the simple commutation relations so that the cumulant function takes the form (see ??)

$$\mathcal{K}_{ij}(\tau) = \begin{cases} -\sum_{k \neq i} \Gamma_{kk} & \text{if} \quad i = j, \\ -\Delta_{ij} + \Delta_{ji} + \Gamma_{ij} & \text{if} \quad i \neq j, \end{cases} \tag{11.22}$$

for $i, j > 0$ and any α, β. As mentioned in Section 11.1 the cases $j = 0$ and $i = 0$ encode trace-preservation and unitality, respectively, and as such $\mathcal{K}_{0j} = \mathcal{K}_{i0} = 0$ since our model is both trace-preserving and unital.[9]

11.2 Calculating the decay amplitudes

In order to evaluate the cumulant function $\mathcal{K}(\tau)$ given by Equation 11.17 and thus the transfer matrix $\langle \tilde{\mathcal{U}}(\tau) \rangle$ from Equation 11.9 for a given control operation, we solely require the decay amplitudes Γ_{kl} and frequency shifts Δ_{kl} since the trace tensor T_{ijkl} depends only on the choice of basis and is therefore trivial (although quite costly for large dimensions, *cf.* Section 11.8) to calculate. In this section, we describe simple methods for calculating Γ_{kl} using an extension of the filter-function formalism developed by Green et al. [65] that we introduced in Reference 36. The central quantity of interest will be the control matrix that we already introduced above. It relates the interaction picture noise operators to the operator basis and we will compute it in Fourier space in order to identify the cross-correlation functions with the noise spectral density

8: Note the similarity to the relationship of a transfer matrix with the χ–matrix, $\mathcal{E}_{ij} = \sum_{kl} \chi_{kl} T_{ikjl}$, with χ_{kl} defined by $\mathcal{E}(\rho) = \sum_{kl} \chi_{kl} C_k \rho C_l$ or, in terms of the Kraus operators K_i of the quantum operation, $\chi_{kl} = \sum_i \text{tr}(K_i C_k) \text{tr}(K_i^\dagger C_l) = \left[\sum_i |K_i\rangle\!\rangle\langle\!\langle K_i| \right]_{kl}$ [85].

9: Unital quantum operations map the identity to the identity (*i.e.*, the identity is a fixed point of $\mathcal{E}$). To violate unitality, the quantum system on $\mathcal{H}$ needs to exchange energy with another system $\mathcal{H}'$, *e.g.* T_1-relaxation, a process which cannot be described by unitary dynamics on $\mathcal{H}$ alone. Because we average over strictly unitary operations on $\mathcal{H}$ to obtain $\langle \tilde{\mathcal{U}} \rangle$, our model cannot capture such processes. The same line of reasoning holds for trace preservation.

in Equation 11.21. We distinguish between a sequence of quantum gates, as already presented in Reference 36, and a single gate. In the first case the control matrix of the entire sequence can be calculated from those of the individual gates, greatly simplifying the calculation if the latter have been precomputed. This approach gives rise to correlation terms in the expression for Γ_{kl} that capture the effects of sequencing gates. In the second case, as was shown by Green et al. [65], one can calculate the control matrix for arbitrary single pulses under the assumption of piecewise-constant control and we lay out how to adapt the approach for numerical applications.

We start by noting that, because we assumed the noise fields $b_\alpha(t)$ to be wide-sense stationary, that is to say the cross-correlation functions evaluated at two different points in time t_1 and t_2 depend only on their difference $t_1 - t_2$, we can define the two-sided noise power spectral density (PSD) $S_{\alpha\beta}(\omega)$ as the Fourier transform of the cross-correlation functions $\langle b_\alpha(t_1)b_\beta(t_2) \rangle$ (see also Equation 2.11),

$$\left\langle b_\alpha(t_1)b_\beta(t_2) \right\rangle = \int_{-\infty}^{\infty} \frac{\mathrm{d}\omega}{2\pi} S_{\alpha\beta}(\omega)e^{-i\omega(t_1-t_2)}. \tag{11.23}$$

Note that the spectrum only characterizes the noise fully in the case of Gaussian noise. For non-Gaussian components in the noise, additional polyspectra have in principle to be considered for higher-order correlation functions [33]. However, since we only discuss second-order contributions which involve two-point correlation functions here, we only need to take $S_{\alpha\beta}(\omega)$ into account. Inserting the definition of the spectral density into Equation 11.21, one finds

$$\Gamma_{\alpha\beta,kl} = \int_{-\infty}^{\infty} \frac{\mathrm{d}\omega}{2\pi} \tilde{\mathcal{B}}_{\alpha k}^*(\omega)S_{\alpha\beta}(\omega)\tilde{\mathcal{B}}_{\beta l}(\omega) \tag{11.24}$$

with $\tilde{\mathcal{B}}(\omega) = \int_0^\tau \mathrm{d}t\, \tilde{\mathcal{B}}(t)e^{i\omega t}$ the frequency-domain control matrix. Note that $\tilde{\mathcal{B}}^*(\omega) = \tilde{\mathcal{B}}(-\omega)$ because $\tilde{\mathcal{B}}(t)$ is real due to our choice of a Hermitian basis C. In the above equation, the fourth-order tensor[10]

$$\mathcal{F}_{\alpha\beta,kl}(\omega) := \tilde{\mathcal{B}}_{\alpha k}^*(\omega)\tilde{\mathcal{B}}_{\beta l}(\omega) \tag{11.25}$$

is the generalized filter function that captures the susceptibility of the decay amplitudes to noise at frequency ω. For $\alpha = \beta, k = l$, and by summing over the basis elements,

$$\mathcal{F}_\alpha(\omega) = \sum_k \left| \tilde{\mathcal{B}}_{\alpha k}(\omega) \right|^2 = \mathrm{tr}\left(\tilde{B}_\alpha^\dagger(\omega)\tilde{B}_\alpha(\omega) \right), \tag{11.26}$$

and this tensor reduces to the canonical *fidelity* filter function [64] from which the entanglement fidelity can be obtained, see Subsection 11.4.1. Thus, if the frequency-domain control matrix $\tilde{\mathcal{B}}_{\alpha k}(\omega)$ for noise source α and basis element k is known, the transfer matrix can be evaluated by integrating Equation 11.24. Moreover, one can study the contributions of each pair of noise sources (α, β) both separately or, at virtually no additional cost and to leading order, collectively by summing over them, $\Gamma_{kl} = \sum_{\alpha\beta} \Gamma_{\alpha\beta,kl}$.

We now discuss how to calculate the control matrix $\tilde{\mathcal{B}}(\omega)$ in frequency space for a given control operation. We focus first on sequences of quantum gates, assuming that the control matrices $\tilde{\mathcal{B}}^{(g)}(\omega)$ for each gate g have been calculated before.

10: Of course, we can also interpret $\mathcal{F}_{\alpha\beta}(\omega) \in \mathscr{L}$ as a linear operator (matrix) in Liouville space, and similarly $\Gamma_{\alpha\beta} \in \mathscr{L}$.
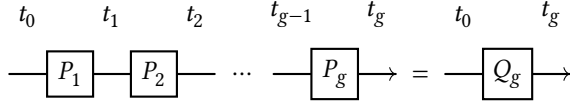
Figure 11.1: Illustration of a sequence of G gates. Individual gates with propagators P_g start at time t_{g-1} and complete at time t_g. The total action from t_0 to t_g is given by Q_g.

11.2.1 Control matrix of a gate sequence

For a sequence of gates with precomputed interaction picture noise operators the approach developed by Green et al. [65] based on piecewise-constant control can be adapted to yield an analytical expression for those of the composite gate sequence that is computationally efficient to evaluate [36]. Here we review these results to give a complete picture of the formalism. While our results are general and apply to any superoperator representation, we employ the Liouville representation here for its simple composition operation: matrix multiplication. Computationally, this is not the most efficient choice since transfer matrices have dimension $d^2 \times d^2$ and thus their matrix multiplication scales unfavorably compared to, for example, left-right conjugation by unitaries (*cf.* Section 11.9). However, because the structure of the control matrix $\tilde{\mathcal{B}}$ is similar to that of a transfer matrix,[11] we will obtain a particularly concise expression for the sequence in the following. For a perhaps more intuitive description employing exclusively conjugation by unitaries, we refer the reader to Reference 36.

11: Remember that it corresponds to a basis expansion of the interaction picture noise operators

We consider a sequence of G gates with propagators $P_g = U_c(t_g, t_{g-1})$, $g \in \{1, \dots, G\}$ that act during the gth time interval $(t_{g-1}, t_g]$ with $t_0 = 0, t_G = \tau$ as illustrated in Figure 11.1. The cumulative propagator of the sequence up to time t_g is then given by $Q_g = \prod_{g'=g}^{0} P_{g'}$ with $P_0 = \mathbb{1}$ and its Liouville representation denoted by $\mathcal{Q}^{(g)}$. Furthermore, the control matrix of the gth pulse at the time $t - t_{g-1}$ relative to the start of segment g is

$$\tilde{\mathcal{B}}_{\alpha k}^{(g)}(t - t_{g-1}) = \mathrm{tr}\Big(U_c^\dagger(t, t_{g-1})B_\alpha(t - t_{g-1})U_c(t, t_{g-1})C_k\Big). \quad (11.27)$$

We can now exploit the fact that in the transfer matrix picture quantum operations compose by matrix multiplication to write the total control matrix at time $t \in (t_{g-1}, t_g]$ as

$$\tilde{\mathcal{B}}(t) = \tilde{\mathcal{B}}^{(g)}(t - t_{g-1})\mathcal{Q}^{(g-1)} \quad (11.28)$$

since $\mathcal{U}_c(t, t_0) = \mathcal{U}_c(t, t_{g-1})\mathcal{Q}^{(g-1)}$ and we have that $\langle\!\langle \tilde{B}(t)| = \langle\!\langle B(t)| \, \mathcal{U}_c(t, t_0) = \langle\!\langle B(t - t_{g-1})| \, \mathcal{Q}^{(g-1)}$. The Fourier transform of Equation 11.28 can then be obtained by evaluating the transform of each gate separately,

$$\tilde{\mathcal{B}}(\omega) = \sum_{g=1}^{G} e^{i\omega t_{g-1}} \tilde{\mathcal{B}}^{(g)}(\omega)\mathcal{Q}^{(g-1)}, \quad (11.29)$$

$$\tilde{\mathcal{B}}^{(g)}(\omega) = \int_{0}^{\Delta t_g} dt\, e^{i\omega t} \tilde{\mathcal{B}}^{(g)}(t), \quad (11.30)$$

with $\Delta t_g = t_g - t_{g-1}$ the duration of gate g. Hence, calculating the control matrix of the full sequence requires only the knowledge of the temporal positions, encoded in the phase factors $e^{i\omega t_{g-1}}$, and the total intended action $\mathcal{Q}^{(g-1)}$ of the individual pulses if their control matrices have been precomputed or obtained otherwise.[12] The sequence structure can thus be exploited to one's benefit. If the same gates appear multiple times during the sequence one can reuse control matrices for equal pulses to

12: Such as analytically.

facilitate calculating filter functions for complex sequences with modest computational effort. Most importantly, Equation 11.29 is independent of the inner structure of the individual pulses and therefore takes the same time to evaluate whether they are highly complex or very simple. In Section 11.9, we will analyze the computational efficiency of capitalizing on this feature in more detail.

As we have seen, the total control matrix of a composite pulse sequence is given by a weighted sum over the individual control matrices. Since $\tilde{\mathcal{B}}(\omega)$ enters Equation 11.24 twice, this leads to correlation terms between two gates at different positions in the sequence when computing the total decay amplitudes Γ. Inserting Equation 11.29 into Equation 11.24 gives

$$
\Gamma_{\alpha\beta,kl} = \sum_{g,g'=1}^{G} \int_{-\infty}^{\infty} \frac{\mathrm{d}\omega}{2\pi} \big[\mathcal{Q}^{(g'-1)\dagger} \tilde{\mathcal{B}}^{(g')\dagger}(\omega) \big]_{k\alpha} S_{\alpha\beta}(\omega) \big[\tilde{\mathcal{B}}^{(g)}(\omega) \mathcal{Q}^{(g-1)} \big]_{\beta l}
$$
$$
\times e^{i\omega(t_{g-1}-t_{g'-1})}
$$
$$
=: \sum_{g,g'=1}^{G} \int_{-\infty}^{\infty} \frac{\mathrm{d}\omega}{2\pi} S_{\alpha\beta}(\omega) \mathcal{F}^{(gg')}_{\alpha\beta,kl}(\omega) \tag{11.31}
$$
$$
=: \sum_{g,g'=1}^{G} \Gamma^{(gg')}_{\alpha\beta,kl} \tag{11.32}
$$

where we defined the pulse correlation filter function $\mathcal{F}^{(gg')}(\omega)$ that captures the temporal correlations between pulses at different positions g and g' in the sequence as well as the corresponding decay amplitudes $\Gamma^{(gg')}$. Unlike regular filter functions, these can be negative for $k = l, g \neq g'$ and therefore reduce the overall noise susceptibility of a sequence given by $\mathcal{F}(\omega) = \sum_{gg'} \mathcal{F}^{(gg')}(\omega)$. By expanding the exponential in Equation 11.9 to linear order, the individual contributions of the pulse correlation FFs can also be traced through to derived quantities such as the infidelity [36, Equation 11]. We have thus gained a concise description of the noise-cancelling properties of gate sequences: in this picture, they arise purely from the concatenation of different pulses, quantifying, for instance, the effectiveness of DD sequences [36].

11.2.2 Control matrix of a single gate

Previous efforts have derived the control matrix analytically for selected pulses such as DD sequences [59], special dynamically corrected gates (DCGs) [66], as well as developed a general analytical framework [64, 65]. However, analytical solutions might not always be accessible, *e.g.* for numerically optimized pulses, and are generally laborious to obtain. Therefore, we now detail a method to obtain the control matrix numerically under the assumption of piecewise-constant control. Our method is similar in spirit to that of Green, Uys, and Biercuk [64] for single qubits with $d = 2$, but whereas those authors computed analytical solutions to the relevant integrals during each time step, here we use matrix diagonalization to obtain the propagator of a control operation to make the approach amenable to numerical implementation. This allows carrying out the Fourier transform of the control matrix Equation 11.16 analytically by writing the control propagators in terms of their eigenvalues in diagonal form.

We divide the total duration of the control operation, τ, into G intervals $(t_{g-1}, t_g]$ of duration Δt_g with $g \in \{0, \dots, G\}$ and $t_0 = 0, t_G = \tau$. We then

approximate the control Hamiltonian as constant within each interval so that within the g

$$H_c(t) = H_c^{(g)} = \text{const.} \tag{11.33}$$

and similarly the deterministic time dependence of the noise operators as $B_\alpha(t) = s_\alpha(t)B_\alpha = s_\alpha^{(g)}B_\alpha$. Under this approximation we can diagonalize the time-independent Hamiltonians $H_c^{(g)}$ with eigenvalues $\omega_i^{(g)}$ numerically and write the time evolution operator that solves the noise-free Schrödinger equation as $U_c(t, t_{g-1}) = V^{(g)}D^{(g)}(t, t_{g-1})V^{(g)\dagger}$. Here, $V^{(g)}$ is the unitary matrix of eigenvectors of $H_c^{(g)}$ and the diagonal matrix $D_{ij}^{(g)}(t, t_{g-1}) = \delta_{ij}\exp\{-i\omega_i^{(g)}(t - t_{g-1})\}$ contains the time evolution of the eigenvalues. Using this result together with Q_{g-1}, the cumulative propagator up to time t_{g-1}, we can acquire the total time evolution operator at time t from $U_c(t) = U_c(t, 0) = U_c(t, t_{g-1})Q_{g-1}$. We then substitute this relation into the definition of the control matrix, Equation 11.16, and obtain

$$\tilde{\mathcal{B}}_{\alpha k}(t) = s_\alpha^{(g)}\text{tr}\Big(Q_{g-1}^\dagger V^{(g)}D^{(g)\dagger}(t, t_{g-1})V^{(g)\dagger}B_\alpha \tag{11.34}$$
$$\times V^{(g)}D^{(g)}(t, t_{g-1})V^{(g)\dagger}Q_{g-1}C_k\Big)$$
$$=: s_\alpha^{(g)}\sum_{ij}\bar{B}_{\alpha,ij}^{(g)}\bar{C}_{k,ji}^{(g)}e^{i\Omega_{ij}^{(g)}(t - t_{g-1})}, \tag{11.35}$$

where we defined $\Omega_{ij}^{(g)} = \omega_i^{(g)} - \omega_j^{(g)}$, $\bar{C}_k^{(g)} = V^{(g)\dagger}Q_{g-1}C_k Q_{g-1}^\dagger V^{(g)}$, and $\bar{B}_\alpha^{(g)} = V^{(g)\dagger}B_\alpha V^{(g)}$. Carrying out the Fourier transform of Equation 11.35 to get the frequency-domain control matrix of the pulse generated by the Hamiltonian from Equation 11.33 is now straightforward since the integrals involved are over simple exponential functions. We obtain

$$\tilde{\mathcal{B}}_{\alpha k}(\omega) = \sum_{g=1}^{G} s_\alpha^{(g)}e^{i\omega t_{g-1}}\text{tr}\Big(\big[\bar{B}_\alpha^{(g)} \circ I^{(g)}(\omega)\big]\bar{C}_k^{(g)}\Big) \tag{11.36}$$

with $I_{ij}^{(g)}(\omega) = -i(e^{i(\omega + \Omega_{ij}^{(g)})\Delta t_g} - 1)/(\omega + \Omega_{ij}^{(g)})$ and the Hadamard product $(A \circ B)_{ij} := A_{ij} \times B_{ij}$. Equation 11.36 is readily evaluated on a computer and thus enables the calculation of filter functions of arbitrary control sequences, either on its own or in conjunction with Equation 11.29. A similar expression is obtained for representations other than the Liouville representation.

11.3 Calculating the frequency shifts

The frequency shifts $\Delta_{\alpha\beta,kl}$ in Equation 11.17 correspond to the second order of the ME and thus involve a double integral with a nested time dependence. This makes their evaluation more involved than that of the decay amplitudes $\Gamma_{\alpha\beta,kl}$ and, in contrast to the previous section, we cannot single out correlation terms as in Equation 11.31. Moreover, since the integrals do not factorize we also cannot derive a concatenation rule that is entirely independent of the internal structure of the constituent gates as before. However, we can still apply the approximation of piecewise-constant control and follow a similar approach as in Subsection 11.2.2 to compute Δ in Fourier space. In ??, we also lay out a concatenation rule for the second-order terms that contains only a minimal contribution from

the internal dynamics of the constituent gates for completeness. Since these terms correspond to a coherent gate error that can in principle be calibrated out to leading order in experiments we will not go into much detail here.

We follow the arguments made above for the decay amplitudes and express the cross-correlation functions $\langle b_\alpha(t) b_\beta(t') \rangle$ by their Fourier transform, the spectral density $S_{\alpha\beta}(\omega)$, using Equation 11.23. Inserting this equation into the definition of the frequency shifts in the time domain, Equation 11.20, yields

$$\Delta_{\alpha\beta,kl} = \int_{-\infty}^{\infty} \frac{\mathrm{d}\omega}{2\pi} S_{\alpha\beta}(\omega) \int_0^\tau \mathrm{d}t\, \tilde{\mathcal{B}}_{\alpha k}(t) e^{-i\omega t} \int_0^t \mathrm{d}t'\, \tilde{\mathcal{B}}_{\beta l}(t') e^{i\omega t'}. \qquad (11.37)$$

We again assume piecewise-constant time segments so that the inner time integral can be split up into a sum of integrals over complete constant segments $(t_{g'-1}, t_{g'}]$ as well as a single integral that contains the last, incomplete segment up to time t. That is, taking the time t of the outer integral to be within the interval $(t_{g-1}, t_g]$ we perform the replacement

$$\int_0^t \mathrm{d}t' \to \sum_{g'=1}^{g-1} \int_{t_{g'-1}}^{t_{g'}} \mathrm{d}t' + \int_{t_{g-1}}^t \mathrm{d}t'. \qquad (11.38)$$

We have thus divided our task into two: The first term allows, as before in Subsections 11.2.1 and 11.2.2, to identify the Fourier transform of the control matrix during time steps g' and g for both the inner and the outer integral according to Equation 11.36. The second term remains a nested double integral, but now the integrand contains only products of complex exponentials because we assume the control to be constant within the limits of integration. As a next step, we also replace the outer time integral by a sum of integrals over single segments, $\int_0^\tau \mathrm{d}t \to \sum_{g=1}^G \int_{t_{g-1}}^{t_g} \mathrm{d}t$, to obtain

$$\Delta_{\alpha\beta,kl} = \int_{-\infty}^{\infty} \frac{\mathrm{d}\omega}{2\pi} S_{\alpha\beta}(\omega) \sum_{g=1}^G \int_{t_{g-1}}^{t_g} \mathrm{d}t$$

$$\times e^{-i\omega t} \tilde{\mathcal{B}}_{\alpha k}(t) \left\{ \sum_{g'=1}^{g-1} \int_{t_{g'-1}}^{t_{g'}} \mathrm{d}t' + \int_{t_{g-1}}^t \mathrm{d}t' \right\} e^{i\omega t'} \tilde{\mathcal{B}}_{\beta l}(t'). \quad (11.39)$$

Before continuing, we ease notation and define $\tilde{\mathcal{B}}(\omega) =: \sum_g \mathcal{G}^{(g)}(\omega)$ with $\mathcal{G}^{(g)}(\omega)$ obtained from Equation 11.36 and furthermore adopt the Einstein summation convention for the remainder of this section, meaning multiple subscript indices that appear on only one side of an equality are summed over implicitly. We now proceed like in Subsection 11.2.2 and make use of the piecewise-constant approximation to diagonalize the control Hamiltonian during each segment. For the nested integrals, we obtain $\tilde{\mathcal{B}}_{\alpha k}(t)$ from Equation 11.35, whereas the remaining integrals factorize and we can identify the Fourier-transformed quantity $\mathcal{G}^{(g)}(\omega)$. Equation 11.39 then becomes

$$\Delta_{\alpha\beta,kl} = \int_{-\infty}^{\infty} \frac{\mathrm{d}\omega}{2\pi} S_{\alpha\beta}(\omega) \sum_{g=1}^G \left[\mathcal{G}_{\alpha k}^{(g)*}(\omega) \sum_{g'=1}^{g-1} \mathcal{G}_{\beta l}^{(g')}(\omega) \right.$$

$$\left. + s_\alpha^{(g)} \bar{B}_{\alpha,ij}^{(g)} \bar{C}_{k,ji}^{(g)} I_{ijmn}^{(g)}(\omega) \bar{C}_{l,nm}^{(g)} \bar{B}_{\beta,mn}^{(g)} s_\beta^{(g)} \right] \qquad (11.40)$$

with $\bar{B}_{\alpha,ij}^{(g)}, \bar{C}_{k,ij}^{(g)}, \Omega_{ij}^{(g)}$ as defined above in Subsection 11.2.2 and

$$I_{ijmn}^{(g)}(\omega) = \int_{t_{g-1}}^{t_g} \mathrm{d}t\, e^{i\Omega_{ij}^{(g)}(t-t_{g-1})-i\omega t} \int_{t_{g-1}}^{t} \mathrm{d}t'\, e^{i\Omega_{mn}^{(g)}(t'-t_{g-1})+i\omega t'}. \qquad (11.41)$$

Explicit results for the integration in Equation 11.41 are given in **??**. To calculate the frequency shifts Δ, we can thus reuse the quantity $\mathcal{G}^{(g)}(\omega)$ also required for the decay amplitudes Γ. The only additional computation, apart from contraction, involves the G integrations $I_{ijmn}^{(g)}(\omega)$. Importantly, Equation 11.40 has the same structure as the corresponding Equation 11.24 for Γ in that the individual entries of Δ are given by an integral over the spectral density of the noise multiplied with a – in this case second-order – filter function that describes the susceptibility to noise at frequency ω:

$$\Delta_{\alpha\beta,kl} = \int_{-\infty}^{\infty} \frac{\mathrm{d}\omega}{2\pi} S_{\alpha\beta}(\omega) \mathcal{F}_{\alpha\beta,kl}^{(2)}(\omega). \qquad (11.42)$$

11.4 Computing derived quantities

By means of Equations 11.29, 11.36 and 11.40, one can obtain the cumulant function $\mathcal{K}(\tau)$ from Equation 11.17 and hence the error process $\langle \tilde{\mathcal{U}}(\tau) \rangle$ from Equation 11.9 for an arbitrary sequence of gates. From this, several quantities of interest for the characterization of a given control operation can be extracted. We explicitly review the average gate and state fidelities as well as expressions to quantify leakage here, but emphasize that this is not exhaustive. Because for many applications the noise is weak and hence the parameter $\xi \ll 1$, we will in the following expand the exponential in Equation 11.9 to leading order in ξ. That is, we approximate[13]

$$\langle \tilde{\mathcal{U}}(\tau) \rangle \approx \mathbb{1} + \mathcal{K}(\tau). \qquad (11.43)$$

13: Remember that $\mathcal{K}(\tau) \in \mathcal{O}(\xi^2)$.

Higher order corrections can be obtained either by explicitly calculating higher powers of $\mathcal{K}$ or by numerically evaluating the exponential of the cumulant function (potentially including higher-order terms from ME and cumulant expansions). The former method often leads to simpler expressions than Equation 11.17 for which the trace tensor T_{ijkl} need not be computed directly. In the weak-noise regime, one can also define specific filter functions for each derived quantity that are given in terms of linear combinations of the generalized filter functions $\mathcal{F}_{\alpha\beta,kl}(\omega)$. The ensemble expectation value of the quantity can then be obtained directly from the overlap with the spectral density, $\int \mathrm{d}\omega / 2\pi\, \mathcal{F}(\omega) S(\omega)$. Finally, we will drop the averaging brackets and the argument of the error transfer matrix $\langle \tilde{\mathcal{U}}(\tau) \rangle$ for brevity in the following.

11.4.1 Average gate and entanglement fidelity

The average gate fidelity is a commonly-quoted figure of merit used to characterize physical gate implementations [46, 49, 96–98]. It represents the fidelity between an implementation $\mathcal{U}$ and the ideal gate $\mathcal{Q}$ averaged over the uniform Haar measure. Since $F_{\mathrm{avg}}(\mathcal{U}, \mathcal{Q}) = F_{\mathrm{avg}}(\mathcal{Q}^\dagger \circ \mathcal{U}, \mathbb{1}) = F_{\mathrm{avg}}(\tilde{\mathcal{U}})$, the average gate fidelity can be obtained from the error channel

$\tilde{\mathcal{U}}$ as [99, 100]

$$F_{\text{avg}}(\tilde{\mathcal{U}}) = \frac{\operatorname{tr}\tilde{\mathcal{U}} + d}{d(d+1)} \tag{11.44}$$

$$=: \frac{d \times F_{\text{ent}}(\tilde{\mathcal{U}}) + 1}{d+1}, \tag{11.45}$$

where d is the system dimension and $F_{\text{ent}}(\tilde{\mathcal{U}}) = d^{-2}\operatorname{tr}\tilde{\mathcal{U}}$ is the entanglement fidelity. In the low-noise regime where Equation 11.43 holds, we can write the entanglement fidelity in terms of the cumulant function $\mathcal{K}_{\alpha\beta}$ approximately as

$$F_{\text{ent}}(\tilde{\mathcal{U}}) = 1 + \frac{1}{d^2}\sum_{\alpha\beta}\operatorname{tr}\mathcal{K}_{\alpha\beta} \tag{11.46}$$

$$=: 1 - \sum_{\alpha\beta}I_{\alpha\beta}(\tilde{\mathcal{U}}). \tag{11.47}$$

Here, we defined $I_{\alpha\beta}$, the infidelity due to a pair of noise sources (α, β). As we show in ??, we can simplify the trace of the cumulant function so that the infidelity reads

$$I_{\alpha\beta} = \frac{1}{d}\operatorname{tr}\Gamma_{\alpha\beta}. \tag{11.48}$$

Equation 11.48 reduces to Equation 32 from Reference 64 for a single qubit ($d = 2$) and pure dephasing noise up to a different normalization convention; by pulling the trace through to the generalized filter function $\mathcal{F}_{\alpha\beta,kl}(\omega)$ in Equation 11.24, we recover the relation (setting $\alpha = \beta$ for simplicity)

$$I_\alpha = \frac{1}{d}\int_{-\infty}^{\infty}\frac{\mathrm{d}\omega}{2\pi}S_\alpha(\omega)\mathcal{F}_\alpha(\omega) \tag{11.49}$$

with the fidelity filter function $\mathcal{F}_\alpha(\omega)$ given by Equation 11.26. Notably, only the decay amplitudes Γ contribute to the fidelity to leading order since the frequency shifts Δ are antisymmetric and therefore vanish under the trace.

11.4.2 State fidelity and measurements

In the context of quantum information processing we are often interested in the probability of measuring the expected state during readout. We can extract this projective readout probability from the transfer matrix in Equation 11.7 by inspecting the transition probability, or state fidelity, between a pure state $\rho = |\psi\rangle\langle\psi|$ and an arbitrary state σ that evolves according to the quantum operation $\mathcal{E} : \sigma \to \mathcal{E}(\sigma)$. Using the double braket notation introduced at the beginning of Chapter 11 we then define the state fidelity as

$$\begin{aligned} F(|\psi\rangle, \mathcal{E}(\sigma)) &= \operatorname{tr}(\rho\mathcal{E}(\sigma)) \\ &= \langle\!\langle\rho|\mathcal{E}(\sigma)\rangle\!\rangle \\ &= \langle\!\langle\rho|\mathcal{E}|\sigma\rangle\!\rangle, \end{aligned} \tag{11.50}$$

where we have expressed the density matrices by vectors and $\mathcal{E}$ as a transfer matrix on the Liouville space $\mathcal{L}$. We can thus calculate arbitrary pure state fidelities by simple matrix-vector multiplications of the transfer matrices $\mathcal{E} = \mathcal{Q}\tilde{\mathcal{U}}$ and the vectorized density matrices $|\rho\rangle\!\rangle$ and $|\sigma\rangle\!\rangle$. In Section 14.3 we employ this measure to simulate a RB experiment where return probabilities are of interest so that $F(|\psi\rangle, \mathcal{E}(\rho)) = \langle\!\langle\rho|\mathcal{Q}\tilde{\mathcal{U}}|\rho\rangle\!\rangle$.

General measurements can be incorporated in the superoperator formalism we have employed here in a straightforward manner using the positive operator-valued measure (POVM) formalism [85, 101]. POVMs constitute a set of Hermitian, positive semidefinite operators $\{E_i\}_i$ (in contrast to the projective measurement $\{|\psi\rangle\langle\psi|, \mathbb{1} - |\psi\rangle\langle\psi|\}$) that fulfill the completeness relation $\sum_i E_i = \mathbb{1}$ and in the double braket notation may be represented as the row vectors $\{\langle\!\langle E_i|\}_i$ in Liouville space. Consequently, the measurement probability for outcome E_i is given by $\langle\!\langle E_i|\mathcal{E}(\sigma)\rangle\!\rangle = \langle\!\langle E_i|\mathcal{E}|\sigma\rangle\!\rangle$ if the system was prepared in the state σ and evolved according to $\mathcal{E}$.

11.4.3 Leakage

In many physical implementations qubits are not encoded in real two-level systems but in two levels of a larger Hilbert space (superconducting transmon [102] or singlet-triplet [103] spin qubits for example) such that population can leak between this computational subspace and other energy levels. Thus, it is often of interest to quantify leakage when assessing gate performance. Recently, Wood and Gambetta [104] have suggested two separate measures for quantifying leakage out of the computational subspace on the one hand and seepage into the subspace on the other. With the filter-function formalism and the transfer matrix of the error process given by Equations 11.7 and 11.17, we can easily extract these quantities.

Using the definitions from Reference 104 and the double braket notation we can write the leakage rate generated by a quantum operation $\mathcal{E}$ as

$$L_c(\mathcal{E}) := \frac{1}{d_c} \langle\!\langle \Pi_\ell| \, \mathcal{E} \, |\Pi_c\rangle\!\rangle \tag{11.51a}$$

and the seepage rate as

$$L_\ell(\mathcal{E}) := \frac{1}{d_\ell} \langle\!\langle \Pi_c| \, \mathcal{E} \, |\Pi_\ell\rangle\!\rangle. \tag{11.51b}$$

Here, $\Pi_{c,\ell}$ are projectors onto the computational and leakage subspaces, respectively, and $d_{c,\ell}$ the corresponding dimensions. For unital channels the leakage and seepage rates are not independent but satisfy $d_c L_c = d_\ell L_\ell$ [104] so that we only need to consider one of the above expressions here (*cf.* Subsection 11.1.2).

Equations 11.51a and 11.51b can be used to determine both coherent and incoherent leakage separately by substituting $\mathcal{Q}$ or $\tilde{\mathcal{U}}$, respectively, for $\mathcal{E}$. While the former is due to systematic errors of the applied pulse and could thus be corrected for by calibration, the latter is induced by noise only. Alternatively, the leakage from both contributions can also be determined collectively by substituting $\mathcal{U}$ for $\mathcal{E}$.

11.5 Performance analysis and efficiency improvements

In this section we focus on computational aspects of the formalism, remarking first on several mathematical simplifications that make the calculation of control matrices and decay amplitudes more economical. Following this, we investigate the computational complexity of the method

in comparison with MC techniques and show that our software implementation surpasses the latter's performance in relevant parameter regimes.

11.6 Periodic Hamiltonians

If the control Hamiltonian is periodic, that is $H_c(t) = H_c(t + T)$, we can reduce the computational effort of calculating the control matrix by potentially orders of magnitude (see Section 14.2 for an application in Rabi driving). We start by making the following observations: First, the frequency-domain control matrix of every period of the control is the same so that $\tilde{\mathcal{B}}^{(g)}(\omega) = \tilde{\mathcal{B}}^{(1)}(\omega)$. Moreover, $e^{i\omega\Delta t_g} = e^{i\omega T}$ for all g so that $e^{i\omega t_{g-1}} = e^{i\omega T(g-1)}$ and by the composition property of transfer matrices $Q^{(g-1)} = [Q^{(1)}]^{g-1}$ where the superscript without parentheses denotes matrix power. We can then simplify Equation 11.29 to read

$$\tilde{\mathcal{B}}(\omega) = \tilde{\mathcal{B}}^{(1)}(\omega) \sum_{g=0}^{G-1} \left[e^{i\omega T} Q^{(1)} \right]^g . \tag{11.52}$$

Furthermore, if the matrix $\mathbb{1} - e^{i\omega T} Q^{(1)}$ is invertible, which is typically the case for the vast majority of values of ω, the previous expression can be rewritten as

$$\tilde{\mathcal{B}}(\omega) = \tilde{\mathcal{B}}^{(1)}(\omega) \left(\mathbb{1} - e^{i\omega T} Q^{(1)} \right)^{-1} \left(\mathbb{1} - \left[e^{i\omega T} Q^{(1)} \right]^G \right) \tag{11.53}$$

by evaluating the sum as a finite Neumann series. Equation 11.53 offers a significant performance benefit over regular concatenation in the case of many periods G as we will show in Section 11.9. Beyond numerical advantages, it also provides an analytical method for studying filter functions of periodic driving Hamiltonians.

11.7 Extending Hilbert spaces

Examining Equation 11.16, we can see that the columns of the control matrix and therefore also the filter function are invariant (up to normalization) under an extension of the Hilbert space. This allows parallelizing pulses with precomputed control matrices in a very resource-efficient manner if one chooses a suitable operator basis. Note that the same also applies to other representations of quantum operations.

Suppose we extend the Hilbert space $\mathscr{H}_1$ of a gate for which we have already computed the control matrix by a second Hilbert space $\mathscr{H}_2$ so that $\mathscr{H}_{12} = \mathscr{H}_1 \otimes \mathscr{H}_2$. If we can find an operator basis whose elements separate into tensor products themselves, *i.e.* $\mathsf{C}_{12} = \mathsf{C}_1 \otimes \mathsf{C}_2$ as for the Pauli basis (*cf.* Section 11.8), the control matrix of the composite gate defined on $\mathscr{H}_{12}$ has the same non-trivial columns as that of the original gate on $\mathscr{H}_1$ up to a different normalization factor. The remaining columns are simply zero. This is because the trace over a tensor product factors into traces over the individual subsystems so that $\tilde{\mathcal{B}}_{\alpha k}(t) \propto \mathrm{tr}([U_1^\dagger \otimes U_2^\dagger][B_\alpha \otimes \mathbb{1}][U_1 \otimes U_2][\mathbb{1} \otimes C_k]) = \mathrm{tr}(U_1^\dagger B_\alpha U_1 \mathbb{1})\mathrm{tr}(U_2^\dagger \mathbb{1} U_2 C_k) = 0$ since we assumed that the noise operators B_α are traceless (*cf.* Subsection 11.1.2).

Generalizing this result to multiple originally disjoint Hilbert spaces we write the composite space as $\mathscr{H} = \bigotimes_i \mathscr{H}_i$ and the corresponding basis as $\mathsf{C} = \bigotimes_i \mathsf{C}_i$. The control matrix of the composite pulse on $\mathscr{H}$ is then

a combination of the columns of the control matrices on $\mathcal{H}_i$ for noise operators B_α that are non-trivial, *i.e.* not the identity, only on their original space. For noise operators defined on more than one subspace, *e.g.* $B_{ij} = B_i \otimes B_j, B_i \in \mathcal{H}_i, B_j \in \mathcal{H}_j$, this evidently holds only for those basis elements that are trivial on either of the subspaces and the columns in the composite control matrix corresponding to non-trivial basis elements $(C_k \otimes C_l : C_k, C_l \neq \mathbb{1})$ need to be computed from scratch.

One can thus reuse precomputed control matrices beyond the concatenation laid out above when studying multi-qubit pulses or algorithms. For concreteness, consider a set of one- and two-qubit pulses whose control matrices have been precomputed. We can then remap those control matrices to any other qubit in a larger register if the entire Hilbert space is defined by the tensor product of the single-qubit Hilbert spaces, and even map the control matrices of two different pulses to the same time slot on different qubits. Thus, we do not need to perform the possibly costly computation of the control matrices again but instead only need to remap the columns of $\tilde{\mathcal{B}}$ to the equivalent basis elements in the basis of the complete Hilbert space, making the assembly of algorithms that consist of a limited set of gates which are used at several points in the algorithm more efficient. In Section 14.4 we simulate a four-qubit QFT algorithm making use of the shortcuts described here.

11.8 Operator bases

Up to this point, we have not explicitly specified the basis that defines the Liouville representation. The only conditions imposed by Equation 11.14 are orthonormality with respect to the Hilbert-Schmidt product and that the basis elements are Hermitian. Yet, the choice of operator basis can have a large impact on the time it takes to compute the control matrix as discussed in the previous section. We therefore give a short overview over two possible choices in the following. As we are mostly interested in the computational properties, we represent linear operators in $\mathsf{L}(\mathcal{H})$ as matrices on $\mathbb{C}^{d \times d}$.

The n-qubit Pauli basis fulfills the requirements set by Equation 11.14 and furthermore allows for the simplifications described before. In our normalization convention where $\langle C_i, C_i \rangle = \mathbb{1}$ it can be written as

$$\mathsf{P}_n := \{\sigma_i\}_{i=0}^{d^2-1} = 2^{-\frac{n}{2}} \times \left\{\mathbb{1}, \sigma_x, \sigma_y, \sigma_z\right\}^{\otimes n} \tag{11.54}$$

with the Pauli matrices σ_x, σ_y and σ_z. While it is obvious that it is separable, meaning it factors into tensor products of the single-qubit Pauli matrices, the dimension of the Pauli basis is restricted to powers of two, $d = 2^n$. An operator basis without this restriction is the generalized Gell-Mann (GGM) basis [105, 106]. In the following we will discuss optimizations pertaining to this basis that are also implemented in the software (see Chapter 13).

The GGM matrices are a generalization of the Gell-Mann matrices known from particle physics to arbitrary dimensions. In our normalization convention, the basis (excluding the identity element) is given by [107]

$$\Lambda_d := \{\Lambda_i\}_{i=1}^{d^2-1} = \left\{u_{jk}, v_{jk}, w_l\right\}_{j,k,l} \tag{11.55}$$

with

$$u_{jk} = \frac{1}{\sqrt{2}} \left(|j\rangle\langle k| + |k\rangle\langle j| \right), \tag{11.55a}$$

$$v_{jk} = -\frac{i}{\sqrt{2}} \left(|j\rangle\langle k| - |k\rangle\langle j| \right), \tag{11.55b}$$

$$w_l = \frac{1}{\sqrt{l(l+1)}} \left(\sum_{m=1}^{l} |m\rangle\langle m| - l|l+1\rangle\langle l+1| \right), \tag{11.55c}$$

for $1 \leq j < k \leq d$, $1 \leq l \leq d-1$, and an orthonormal vector basis $\{|j\rangle\}_{j=1}^{d}$ of the Hilbert space. Expanding an arbitrary matrix $A \in \mathbb{C}^{d \times d}$ in the basis of Equation 11.55 is then simply a matter of adding up the corresponding matrix elements of A according to Equations 11.55a to 11.55c. For instance, the expansion coefficient for the first symmetric basis element can simply be read off to be $\langle u_{12}, A \rangle = 2^{-1/2}(\langle 1|A|2\rangle + \langle 2|A|1\rangle)$. The explicit construction prescription of the GGM basis thus allows calculating inner products of the form $\langle \Lambda_j | A \rangle$ at constant cost instead of the quadratic cost of the trace of a matrix product, speeding up the computation of the transfer matrix from Equation 11.1 (in which case $A = \mathcal{E}(\Lambda_k)$). In numerical experiments, calculating the transfer matrix of a unitary U with dimension d and precomputed matrix products $A_k = U\Lambda_k U^\dagger$ scaled as $\sim d^{4.16}$. This agrees with the expected scaling of $\sim d^4$ (a transfer matrix has $d^2 \times d^2$ elements) and presents a significant improvement over the explicit calculation with trace overlaps $\mathrm{tr}(\Lambda_j A_k)$ that we observed to scale as $\sim d^{5.93}$ (we expected $\sim d^6$).

Further inspection of the GGM basis additionally reveals an increasing sparsity for large d (the density scales asymptotically as d^{-2}), so that it is well suited for computing the trace tensor Equation 11.18. Since this tensor has d^8 elements, the amount of memory required for a dense representation becomes unreasonably large quite quickly. To overcome this constraint, we can use a GGM basis instead of a comparably dense basis like the Pauli basis. In this case, the resulting tensor is also sparse because the overlap between different basis elements is small.[14] This not only enables storing the tensor in memory but also makes the calculation much faster since one can employ algorithms optimized for operations on sparse arrays (see Chapter 13).

As an illustration, consider a system of four qubits so that the Hilbert space has dimension $d = 2^4$. An operator basis for this space has $d^2 = 2^8$ elements and consequently the tensor T_{ijkl} has $(2^8)^4 = 2^{32}$ entries. Using 128 bit complex floats to represent the entries the tensor would take up $\approx 68\,\text{GB}$ of memory in a dense format. Conversely, for a GGM basis stored in a sparse data structure, the resulting trace tensor only takes up $\approx 100\,\text{MB}$ of memory. Furthermore, calculating T takes $\approx 2.89\,\text{s}$ on an Intel® Core™ i9-9900K eight-core processor since a GGM basis has a low density. By contrast, the same calculation with a Pauli basis takes $\approx 217\,\text{s}$. This is due to the larger density on the one hand and because sparse matrix multiplication algorithms perform poorly with dense matrices on the other.

14: The Pauli basis has a density of $1/d$, compared to the GGM's of $\sim 1/d^2$. This results in trace tensors with density $1/d^2$ and $\sim 1/d^4$, respectively.

11.9 Computational complexity

In order to assess the performance of FFs for computing fidelities compared to MC methods, we determine each method's asymptotic scaling

behavior as a function of the system dimension d. For the filter functions, we calculate the fidelities using Equations 11.26 and 11.49 in our software implementation, described in more detail in Chapter 13, and hence neglect contributions of $\mathcal{O}(\xi^4)$ from the frequency shifts Δ. Additionally, we distinguish between three different approaches for calculating the control matrix; first, for a single pulse following Equation 11.36, second for an arbitrary sequence of pulses following Equation 11.29, and third for a periodic sequence of pulses following Equation 11.53. For the single pulse, we run benchmarks using exemplary values for the various parameters on a machine with an AMD FX™-6300 processor with six logical cores and 24 GB of memory. We also discuss the filter function method using left-right conjugation by unitaries instead of the Liouville representation. The latter has higher memory requirements and is expected to perform poorly for large system dimensions d since one deals with $d^2 \times d^2$ transfer matrices on a Liouville space $\mathscr{L}$ instead of $d \times d$ unitaries on a Hilbert space $\mathscr{H}$. In the software package, the calculations are currently implemented in Liouville space and calculation by conjugation is only partially supported through the low-level API. However, both representations perform similarly for small dimensions as we show below. Note that for a fair performance comparison the different nature of errors needs to be kept in mind. MC becomes less costly if larger statistical errors can be tolerated, whereas the filter-function formalism is typically limited by higher order errors. For reference, the following considerations are summarized in Table 11.1 for each approach and a representative set of parameters.

The MC algorithm is laid out in detail in **??**. To calculate the fidelity using MC, we generate n_{MC} different noise traces that slice every time step Δt of the pulse into $n_{\mathrm{seg}} = f_{\mathrm{UV}}\Delta t$ segments to appropriately sample the spectral density with f_{UV} being the ultraviolet cutoff frequency. In total, there are $n_{\Delta t}n_{\mathrm{MC}}n_{\mathrm{seg}}$ noise samples for each of which the Hamiltonian is diagonalized, exponentiated, and the resulting propagators multiplied to get the final, noisy unitary. The entanglement fidelity is then obtained by averaging the trace overlap $d^{-1}\mathrm{tr}(Q^\dagger U)$ of ideal and noisy unitary over all noise realizations. Taking the complexity of matrix diagonalization to be $\mathcal{O}(d^3)$ and matrix multiplication to be $\mathcal{O}(d^b)$ with $b = 3$ for a naive algorithm and $b = 2.376$ for the Coppersmith-Winograd algorithm [108], we expect MC to scale with the dimension d of the problem as $\sim n_{\Delta t}n_{\mathrm{MC}}n_{\mathrm{seg}}(d^b + d^3)$. For simplicity, we use a white noise spectrum for which $S(\omega) = \mathrm{const.}$ but note that sampling arbitrary spectra induces additional overhead for MC, depending on which method is used to generate the noise traces. Typical time-domain methods include the simulation of the underlying physical process (like two-state fluctuators) or the application of an inverse Fourier transform to white noise multiplied by a frequency-domain transfer function.

By contrast, the computational cost of the filter-function formalism as realized by Equation 11.36 is independent of the form of the spectrum. For this approach we find the leading terms to scale as $\sim n_{\Delta t}n_\omega n_\alpha d^4 + n_{\Delta t}d^{b+2}$ with n_α the number of noise operators and n_ω the number of frequency samples. Here, the first term is due to the trace in Equation 11.36 which boils down to the trace of a matrix product, $\sum_{ij}A_{ij}B_{ji}$, that scales with d^2 and is performed once for each of the d^2 basis elements, n_α noise operators, $n_{\Delta t}$ time steps, and n_ω frequency points. The second term is due to the transformation $C_k \to \tilde{C}_k^{(g)}$ which requires multiplication of $d \times d$ matrices for every time step and basis element. As $n_\alpha n_\omega < n_{\mathrm{MC}}n_{\mathrm{seg}}$ for realistic parameters because the ultraviolet cutoff frequency needs to be chosen sufficiently high and the relative error of the method de-

Table 11.1: Complexity scaling of the three approaches for calculating average gate fidelities discussed in the text. "FF (explicit)" stands for calculating filter functions from scratch following Equation 11.36, "FF (concat.)" for sequences following Equation 11.29, and "FF (periodic)" for periodic Hamiltonians following Equation 11.53. $\mathcal{H}$ and $\mathcal{L}$ designate the vector space on which calculations are performed. Example values for the dominant contributions listed in the table are given for matrix multiplication exponent $b = 2.376$, dimension $d = 2$, number of time steps $n_{\Delta t} = 1000$, and number of gates $G = 100$ (corresponding to a sequence of 100 single-qubit gates with 10 time steps each) with the remaining parameters as in Figure 11.2. For increasing d the computational advantage of FF ($\mathcal{L}$) over MC diminishes but is conserved for FF ($\mathcal{H}$).

Method	Reference	Dominating scaling	Example values
MC ($\mathcal{H}$)	??	$n_{\Delta t}n_{\mathrm{MC}}n_{\mathrm{seg}}(d^b + d^3)$	1.3×10^8
FF ($\mathcal{L}$, explicit)	Equation 11.36	$n_{\Delta t}n_{\omega}n_{\alpha}d^4 + n_{\Delta t}d^{b+2}$	2.4×10^7
FF ($\mathcal{H}$, explicit)	Equation 11.36	$n_{\Delta t}n_{\omega}n_{\alpha}(d^2 + d^b)$	1.4×10^7
FF ($\mathcal{L}$, concat.)	Equation 11.29	$Gn_{\omega}n_{\alpha}d^4 + Gd^{2b}$	2.4×10^6
FF ($\mathcal{H}$, concat.)	Equation 11.29	$Gn_{\omega}n_{\alpha}d^b$	7.8×10^5
FF ($\mathcal{L}$, periodic)	Equation 11.53	$n_{\omega}(n_{\alpha}d^4 + d^{2b}[1 + \log G])$	1.0×10^5

creases with $1/\sqrt{n_{\mathrm{MC}}}$, we expect that in the case of a single pulse the filter-function formalism in Liouville representation should outperform Monte Carlo calculations for reasonably small dimensions d. Using left-right conjugation, this advantage should hold also for large d. In this case the Hadamard product ($\sim d^2$) as well as matrix multiplication ($\sim d^b$) are carried out for each frequency, noise operator, and time step to calculate the interaction picture noise operators $\bar{B}_{\alpha}(\omega)$. We thus find this method to scale with $\sim n_{\Delta t}n_{\omega}n_{\alpha}(d^2 + d^b)$.

Figure 11.2 shows exemplary wall times for both methods and $d \in [2, 120]$ that confirm our expectation. Only for about $d \approx 100$ the overhead from the extra time steps and trajectories over which is averaged is compensated for MC. For smaller dimensions the calculation using FFs is faster by almost two orders of magnitude (see the inset showing the same data in a log-log plot). The lines show fits to $t = ad^b$. The data is not quite in the asymptotic regime due to limited memory so that even for large dimension terms of lower power in d contribute significantly to the run time. Even though this causes the fits to underestimate the exponent b, the general trend agrees with our expectation. Note that the crossover does not always occur at the same dimension d. On a different system with an Intel® Core™ i9-9900K eight-core processor the FF method outperformed MC even for $d = 120$ beyond which available memory limited the simulation.

Quantifying the performance gain from using the control matrices' concatenation property to calculate fidelities of gate sequences is more difficult since it strongly depends on the number of gates occurring multiple times in the sequence (enabling reuse of precomputed control matrices) as well as the complexity of the individual gates. The evaluation using the concatenation rule Equation 11.29 performs asymptotically worse than the evaluation for a complete pulse according to Equation 11.36 because of higher powers of d dominating the calculation in the former case. Performing the G matrix multiplications $\tilde{\mathcal{B}}^{(g)}(\omega)\mathcal{Q}^{(g-1)}$ from Equation 11.29 is of order $\sim Gn_{\omega}n_{\alpha}d^4$, with G the number of pulses in the sequence. Furthermore, calculating the transfer matrix of the total propagators Q_{g-1} involves multiplication of $d \times d$ matrices for all d^4 combinations of basis elements amounting to $\sim Gd^{b+4}$. In case the Liouville representation of the individual pulses' total propagators P_g, $\mathcal{P}^{(g)}$, have been precomputed, the latter computation can be made more efficient since one can just propagate the transfer matrices $\mathcal{P}^{(g)}$ to obtain the cumulative transfer matrices for the sequence, $\mathcal{Q}^{(g)} = \prod_{g'=g}^{0} \mathcal{Q}^{(g')}$, at cost
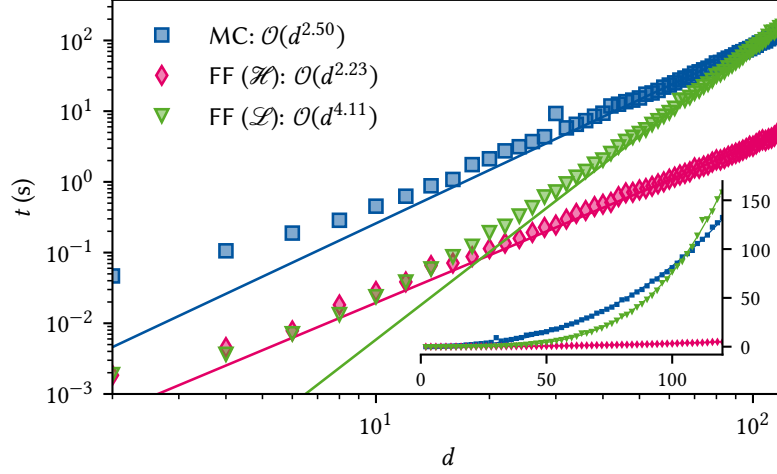
Figure 11.2: Performance of the formalism using Equation 11.36 compared to a Monte Carlo method for a single gate as a function of problem dimension d. Parameters are: $n_{\Delta t} = 1, n_\alpha = 3, n_{\text{MC}} = 100, f_{\text{UV}} = 10^2/\Delta t, n_\omega = 500$ where n_α is the number of noise operators considered, n_{MC} the number of Monte Carlo trajectories over which is averaged, and n_ω the number of frequency samples. The calculation using filter functions clearly outperforms MC for small system sizes. For dimensions larger than $d \approx 100$ (roughly equivalent to 7 qubits) Monte Carlo (blue squares) performs better than the FF calculation with transfer matrices (green triangles) for this set of parameters and processor due to the better scaling behavior. Using conjugation by unitaries (orange diamonds) significantly outperforms MC also for large dimensions. While the fits to $t = ad^b$ (lines) underestimate the leading order exponent due to the data not being in the asymptotic regime, they support the expected relationship of complexity between the approaches. The inset shows the same data on a linear scale, highlighting the different scaling behaviors for large d.

$\sim Gd^{2b}$. The restriction to small dimensions does not apply for conjugation by unitaries as in this case the matrix multiplications involve $d \times d$ matrices and we do not have to compute the Liouville representation. We thus obtain a more favorable asymptotic scaling of $\sim Gn_\omega n_\alpha d^b$.

Utilizing the concatenation property in the Liouville representation thus corresponds to effectively reducing the number of times the calculations scaling with $\sim n_\omega n_\alpha d^4$ have to be carried out but incurs additional calculations scaling with $\sim d^{2b}$. Accordingly, it provides a performance benefit if a sequence consists of either very complex pulses, in which case single repetitions already make the calculation much more efficient, or of few pulses that occur many times. In the extremal case of G repetitions of a single gate the benefit of employing the concatenation property is most pronounced and can be improved even further utilizing the simplifications laid out in Section 11.6. Since matrix inversion has the same complexity as matrix multiplication and taking a matrix to the Gth power requires $\mathcal{O}(\log G)$ matrix multiplications, Equation 11.53 should scale with $\sim n_\omega(n_\alpha d^4 + d^{2b} + d^{2b} \log G)$ (the first two terms are due to the final matrix multiplications and are independent of G). It hence allows for a vast speedup over Equation 11.29 in that the asymptotic behavior as a function of the number of gates changes from $\sim G$ to $\sim \log G$. An example of this is presented in Section 14.2 for the context of Rabi driving. Note that this closed form is a unique feature of the transfer matrix representation and not applicable to conjugation by unitaries.

Filter functions from random sampling

12

IN our derivation of the average error map $\langle\tilde{\mathcal{U}}\rangle$, Equation 11.9, we employed the cumulant expansion due to Kubo [38, 75]. In his papers, Kubo makes the claim that this expansion is exact for Gaussian noise when truncating after the second order, even for *q-numbers*, *i.e.*, linear operators. For *c-numbers* – scalars – this is a well-known result in statistics; the Gaussian probability distribution is fully described by its first two cumulants, the mean μ and variance σ^2. However, Fox [39] showed many years later that Kubo's claim for *q*-numbers does not hold, and that non-commutativity in the Gaussian variables can cause higher-order cumulants to not vanish. There are two limiting cases in which the expansion remains exact; first, for white noise, whose auto-correlation function is singular at $t = 0$, and thus "decouples" higher-order cumulants, and second, commuting noise, for which $[H_\mathrm{c}(t), H_\mathrm{n}(t)] = 0 \forall t$. Beyond these two cases, we must therefore assume that the map given by Equation 11.9 is merely approximate when including only up to second-order terms from the Magnus expansion.[1] In this chapter, we investigate the extent of this error. To this end, we compute the *exact* filter function (FF) using a Monte Carlo (MC) approach by randomly sampling monochromatic noise fields.

1: Note that the cluster property still holds in all cases, and hence for Gaussian noise only even-order cumulants do not vanish [39, 76, 109, 110].

12.1 Reconstruction by frequency-comb time domain simulation

For a given interaction-picture quantum operation $\langle\tilde{\mathcal{U}}(\tau)\rangle$ resulting from the quantum system's evolution under the noise fully characterized by its PSD $S(\omega)$, we *define* the filter function $\mathcal{F}(\omega; \tau)$ by

$$\langle\tilde{\mathcal{U}}(\tau)\rangle = \exp\mathcal{K}(\tau) = \exp\left\{-\int\frac{\mathrm{d}\omega}{2\pi}\mathcal{F}(\omega;\tau)S(\omega)\right\}. \qquad (12.1)$$

Now, suppose that

$$S(\omega) = 2\pi\sigma_i^2\delta(\omega - \omega_i) =: S_i(\omega), \qquad (12.2)$$

that is, the PSD of a monochromatic sinusoid of frequency ω_i and root mean square (RMS) σ_i.[2] Equation 12.1 then becomes

2: Equation 12.2 discretizes $S(\omega)$ by sampling it at points ω_i, *i.e.*,

$$S(\omega) \sim \lim_{n\to\infty}\sum_{i=1}^{n} S_i(\omega).$$

See also Sidenote 12.

$$\langle\tilde{\mathcal{U}}_i(\tau)\rangle := \langle\tilde{\mathcal{U}}(\tau)\rangle = \exp\left\{-2\pi\sigma_i^2\int\frac{\mathrm{d}\omega}{2\pi}\mathcal{F}(\omega;\tau)\delta(\omega - \omega_i)\right\} \qquad (12.3)$$

$$= \exp\left\{-\sigma_i^2\mathcal{F}(\omega_i;\tau)\right\}, \qquad (12.4)$$

where $\langle\tilde{\mathcal{U}}_i(\tau)\rangle$ is the noisy quantum operation generated by monochromatic noise with PSD $S_i(\omega)$ according to Equation 12.2. It is now easy to invert Equation 12.4, and we obtain

$$\mathcal{F}(\omega_i;\tau) = -\sigma_i^{-2}\log\langle\tilde{\mathcal{U}}_i(\tau)\rangle. \qquad (12.5)$$

Because we represent quantum operations as matrices in Liouville space, Equation 12.5 is straightforward to implement on a computer; to sample the exact FF at the set of discrete frequencies $\{\omega_i\}_i$ we simply need to

compute $\langle\tilde{\mathcal{U}}_i(\tau)\rangle$ using a time-domain simulation method of our choice and take the logarithm![3]

Indeed, we can go a step further and split apart the coherent and incoherent contributions to the noisy evolution. Since (in-)coherent quantum operations are represented by (anti-)symmetric matrices in Liouville space, we may define the incoherent and coherent FFs by

$$
\begin{aligned}
\mathcal{F}_\Gamma(\omega_i;\tau) &= \frac{1}{2}\left(\mathcal{F}(\omega_i;\tau) + \mathcal{F}(\omega_i;\tau)^\top\right) \\
&= -\frac{1}{2\sigma_i^2}\left(\log\langle\tilde{\mathcal{U}}_i(\tau)\rangle + \log\langle\tilde{\mathcal{U}}_i(\tau)\rangle^\top\right),
\end{aligned}
\tag{12.6}
$$

and

$$
\begin{aligned}
\mathcal{F}_\Delta(\omega_i;\tau) &= \frac{1}{2}\left(\mathcal{F}(\omega_i;\tau) - \mathcal{F}(\omega_i;\tau)^\top\right) \\
&= -\frac{1}{2\sigma_i^2}\left(\log\langle\tilde{\mathcal{U}}_i(\tau)\rangle - \log\langle\tilde{\mathcal{U}}_i(\tau)\rangle^\top\right),
\end{aligned}
\tag{12.7}
$$

respectively. In the filter-function formalism presented in Chapter 11, Equations 12.6 and 12.7 correspond – up to corrections from non-vanishing higher cumulants – to linear combinations of the generalized filter functions from second- and first-order Magnus expansion, respectively. To be more precise, let us again consider Equation 11.17. Rather than first performing the integrations of Equations 11.20 and 11.21 to obtain the decay amplitudes Γ and frequency shifts Δ, and then the contractions with the trace tensor functions g_{ijkl} and f_{ijkl}, first contract the latter with the control matrices to obtain the time-domain filter functions[4]

$$
\mathcal{F}_{ij}^{(\Gamma)}(t_1, t_2) = \frac{1}{2}\sum_{kl} g_{ijkl}\tilde{\mathcal{B}}_k(t_1)\tilde{\mathcal{B}}_l(t_2),
\tag{12.8}
$$

$$
\mathcal{F}_{ij}^{(\Delta)}(t_1, t_2) = \frac{1}{2}\sum_{kl} f_{ijkl}\tilde{\mathcal{B}}_k(t_1)\tilde{\mathcal{B}}_l(t_2).
\tag{12.9}
$$

Again moving to Fourier space and following the same procedure as in Sections 11.2 and 11.3 leads to the coherent and incoherent frequency-domain filter functions $\mathcal{F}_{kl}^{(\Gamma)}(\omega;\tau)$ and $\mathcal{F}_{kl}^{(\Delta)}(\omega;\tau)$ that we must simply integrate over to obtain the average error process $\langle\tilde{\mathcal{U}}(\tau)\rangle$,[5]

$$
\langle\tilde{\mathcal{U}}(\tau)\rangle = \exp\left\{-\int\frac{d\omega}{2\pi}S(\omega)\left[\mathcal{F}^{(\Gamma)}(\omega;\tau) + \mathcal{F}^{(\Delta)}(\omega;\tau)\right]\right\}.
\tag{12.10}
$$

This allows us to analyze in detail deviations of the closed-form expression obtained by means of the cumulant expansion, Equation 12.10, from the exact filter function sampled at discrete ω_i by Equation 12.5. In the following, we will lay out explicitly how the latter can be computed in the time domain using a MC method.[6]

To begin with, observe that

$$
\langle\tilde{\mathcal{U}}_i(\tau)\rangle = \mathcal{Q}^\top\langle\mathcal{U}_i(\tau)\rangle,
\tag{12.11}
$$

where as usual $\mathcal{Q}$ is the complete superpropagator of the noise-free time evolution and $\mathcal{U}_i(\tau)$ that of the noisy time evolution generated by a single realization of the noise $b(t)$, both of which are orthogonal, *i.e.*, the corresponding Hilbert-space operators are unitary. In MC, we generate N realizations of this noise process in the time domain, compute the full time evolution superpropagator $\mathcal{U}_i(\tau)$, and then evaluate the expectation value $\langle\,\bullet\,\rangle$ as the ensemble average to obtain $\langle\mathcal{U}_i(\tau)\rangle$.[7] Inserting into Equa-

tion 12.4, we find that

$$\mathcal{F}(\omega_i; \tau) = -\sigma_i^{-2} \log \langle \tilde{\mathcal{U}}_i(\tau) \rangle = -\sigma_i^{-2} \log \mathcal{Q}^\top \langle \mathcal{U}_i(\tau) \rangle. \tag{12.12}$$

If we evaluate Equation 12.12 for a set of frequencies $\{\omega_i\}_i$ sampling the true spectrum $S(\omega)$ sufficiently well, we thus obtain the exact filter function $\mathcal{F}(\omega; \tau)$ (within the accuracy of MC), allowing us to compare the accuracy of the formalism developed in Chapter 11.

So what does a single noise realization of Equation 12.2 in the time domain look like? It is a sinusoid with amplitude $A_i \sim \mathrm{Rayleigh}(\sigma_i)$,[8] frequency ω_i, and phase $\phi \sim \mathrm{Unif}(0, 2\pi)$,[9]

$$b(t) = A_i \sin(\omega_i t + \phi). \tag{12.13}$$

To obtain the MC estimate of $\langle \tilde{\mathcal{U}}(\tau) \rangle$, we therefore draw N noise traces according to Equation 12.13, solve the Schrödinger equation, and finally perform the ensemble average from which we can deduce the filter function using Equation 12.12. From the spread of the individual MC samples we obtain confidence intervals on the mean of the error transfer matrix by bootstrapping, which we propagate to the filter function by taking the Fréchet derivative of the matrix logarithm in Equation 12.12 [113].

12.2 Case studies

Let us now turn to applying the method to a few select case studies. First, we consider a pure-dephasing Hamiltonian with

$$
\begin{aligned}
H_c(t) &= \Omega \frac{\sigma_z}{2}, \\
H_n(t) &= b(t) \frac{\sigma_z}{2}.
\end{aligned}
\tag{12.14}
$$

Specifically, we let the system evolve under the Hamiltonian in Equation 12.14 for $\tau = \pi/\Omega$ to undergo a π-rotation around the z-axis of the Bloch sphere. For this model, we expect the cumulant expansion to terminate after the second order because control and noise commute, and hence the interaction-picture noise Hamiltonian, $\tilde{H}_n(t)$, always commutes with itself, and therefore the filter-function formalism of Chapter 11 should give the exact result. Equation 12.14 can be solved ana-

8: Rayleigh(σ) is the Rayleigh distribution with probability density function [112]

$$\rho(x) = \frac{x}{\sigma^2} \exp\left\{-\frac{x^2}{2\sigma^2}\right\}.$$

It describes the probability distribution of the distance from the origin of a point drawn from a bivariate normal distribution with mean 0 and standard deviation σ.

9: The probability density function of the uniform distribution $\mathrm{Unif}(a, b)$ is

$$\rho(y) = \begin{cases} (b-a)^{-1} & \text{if} \quad a \leq y < b, \\ 0 & \text{else} \end{cases}$$
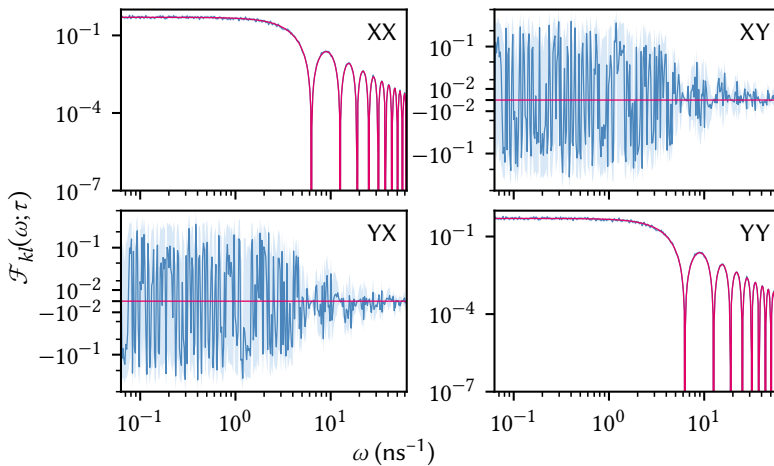
Figure 12.1: Non-zero components of the FF in the Pauli basis P_1 for the pure dephasing Hamiltonian in Equation 12.14. Magenta lines are from the cumulant expansion, Equation 12.10, blue lines the mean of the MC simulation, Equation 12.12, and light blue shaded areas the 95 % confidence interval. The diagonal elements (XX and YY) agree within the MC confidence intervals, with the zeros at $2\pi n/\tau, n \in \{1, 2, \dots\}$ agreeing down to 10^{-15} where we can expect numerical errors to be limiting. The off-diagonal elements are quite noisy in the MC simulation, but fluctuate about the expected value of zero.
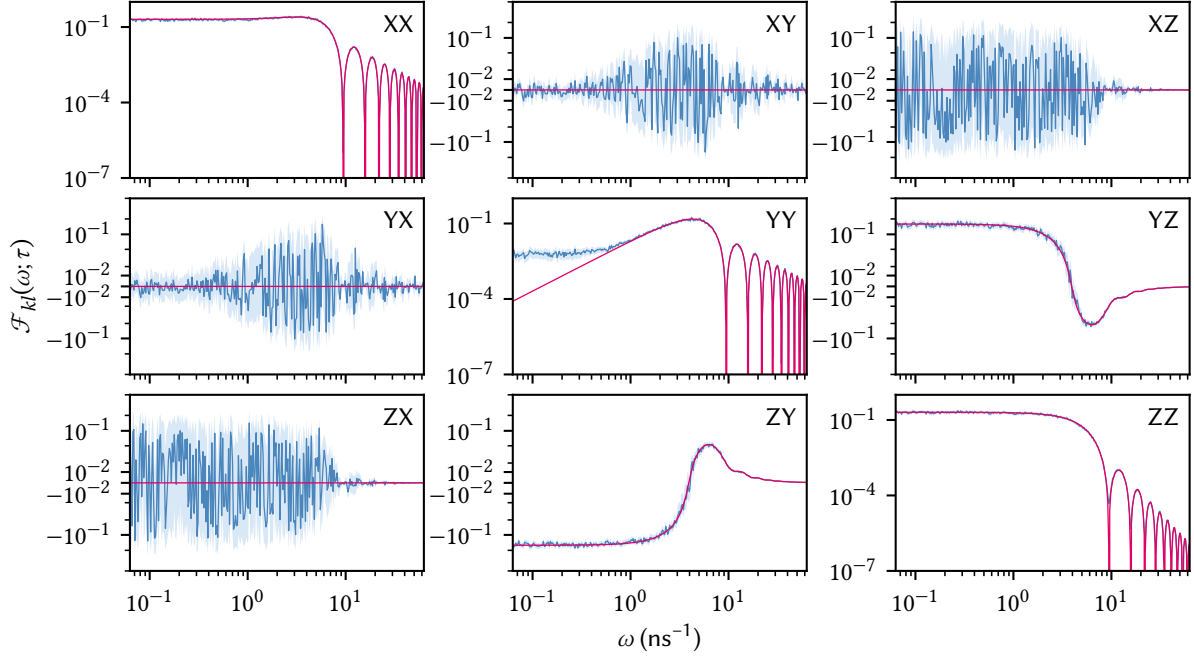
Figure 12.2: FFs for the non-commuting Hamiltonian in Equation 12.15. Cumulant expansion calculation is shown in magenta, MC in blue with light blue shaded areas the confidence intervals. Again, the nominally-zero off-diagonals are susceptible to numerical noise in the MC method. The YY- and ZZ-terms show a deviation of the cumulant expansion calculation, while all others, including the coherent YZ- and ZY-terms appear to be exact up to the numerical uncertainty.

lytically, and gives rise to an ideal dephasing channel whose PTM representation is diagonal, $\langle \tilde{\mathcal{U}}(\tau) \rangle = \mathrm{diag}(1, 1 - p, 1 - p, 1)$ with p the dephasing probability whose precise value depends on the form of the PSD $S(\omega)$. Accordingly, the FF $\mathcal{F}_{kl}(\omega; \tau)$ should be zero everywhere but at $k = l \in \{1, 2\} \equiv \{x, y\}$ for the Pauli basis P_1. Figure 12.1 shows the total "error transfer matrix filter functions" (Equations 12.10 and 12.12) computed with both methods; magenta for the cumulant expansion and blue for the exact MC method. The diagonals agree perfectly within the confidence intervals, while the off-diagonals are dominated by numerical noise in the MC approach. Since the off-diagonals are zero, only the first-order Magnus terms contribute.[10]

10: Recall that $\mathcal{F}^{(\Delta)}(\omega; \tau)$ is antisymmetric.

The opposite extreme to the pure-dephasing Hamiltonian is obtained when changing the control to be transverse to the noise,

$$
\begin{aligned}
H_{\mathrm{c}}(t) &= \Omega \frac{\sigma_x}{2}, \\
H_{\mathrm{n}}(t) &= b(t) \frac{\sigma_z}{2}.
\end{aligned}
\tag{12.15}
$$

In this case, control and noise Hamiltonian maximally do not commute at any time ($\tilde{H}_{\mathrm{n}}(t) = \sigma_z \cos \Omega t + \sigma_y \sin \Omega t$) and we should expect the largest deviations from the exact filter functions in the approximation by truncating the cumulant function after the second order. Figure 12.2 shows the FF for a π-rotation around the x-axis of the Bloch sphere (*i.e.*, $\tau = \pi/\Omega$ once again). This time, all diagonal elements are nonzero, and the YY-term ($\mathcal{F}_{22}(\omega; \tau)$ with $\sigma_2 \equiv \sigma_y$) displays a deviation between cumulant expansion and MC simulation towards low frequencies! This is exactly what we would expect according to Fox [39], namely that the more correlated the noise is, the larger contributions from higher orders will be.[11] Also deviating is the ZZ-term, although not towards DC but where the filter function computed from the approximated cumulant function drops

11: Quasistatic noise is perfectly correlated—it assumes a single value for all times.
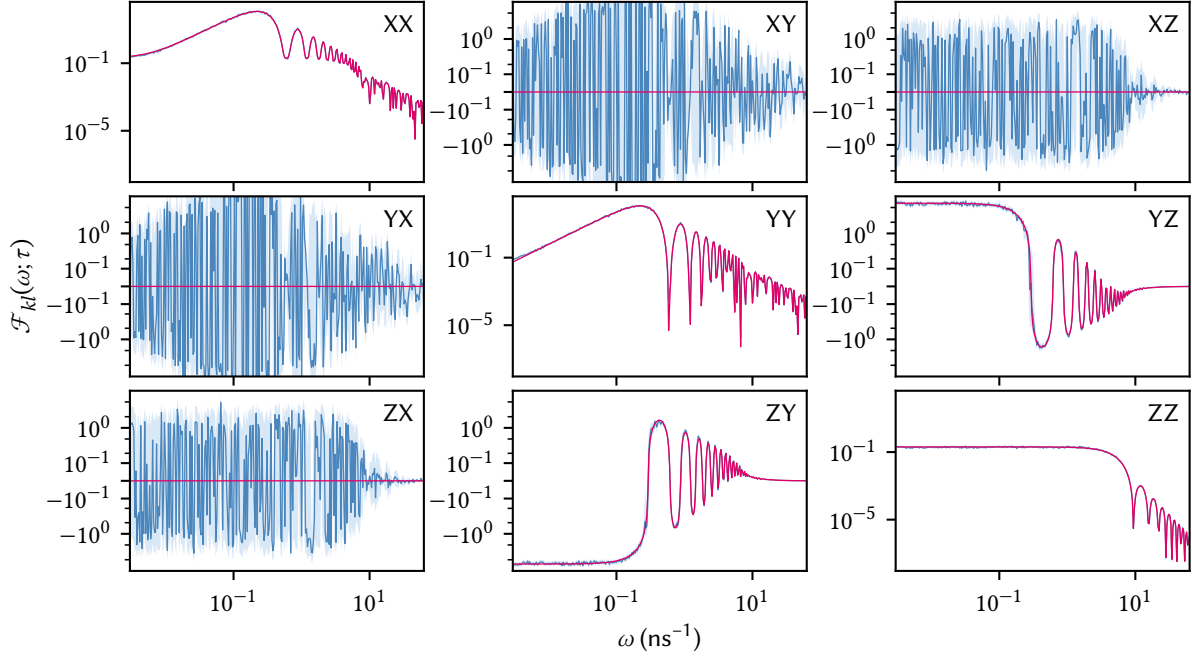
Figure 12.3: FFs for the spin echo (SE) Hamiltonian in Equation 12.16. Cumulant expansion calculation is shown in magenta, MC in blue with light blue shaded areas the confidence intervals. Both coherent and incoherent terms show excellent agreement between both methods.

to zero. By contrast, the XX-term shows good agreement between both methods. Finally, two non-diagonal elements are nonzero, YZ and ZY, anti-symmetric terms which arise from the second-order Magnus and incur coherent errors. For these, the cumulant approximation is excellent, showing no deviation within the confidence intervals.

Finally, as a last example we consider the prototypical filter-function use case: the spin echo (SE). Here, the qubit idles for a time τ_0 both before and after a π rotation around the *x*-axis of the Bloch sphere, so that the Hamiltonian is given by

$$
\begin{aligned}
H_{\mathrm{c}}(t) &= \Omega(t)\frac{\sigma_x}{2}, \\
H_{\mathrm{n}}(t) &= b(t)\frac{\sigma_z}{2},
\end{aligned}
\tag{12.16}
$$

with $\Omega(t) = \pi/\tau_\pi$ if $t \in [\tau_0, \tau_0 + \tau_\pi]$ and zero else. This pulse sequence is known to cancel quasistatic dephasing noise as the phase picked up on the equator of the Bloch sphere during the first period of free evolution is exactly cancelled by the phase picked up during the second period after the π-pulse. Since the previous example demonstrated that the filter-function formalism based on the second-order cumulant expansion neglects contributions from higher orders in the case of transverse noise, we might expect the SE sequence to show similar behavior. Figure 12.3 shows the results of the simulation. The picture is similar – albeit more complex – to before, with nominally-zero terms suffering from numerical noise. However, in contrast to the simple π-pulse Hamiltonian in Equation 12.15 and Figure 12.2, the YY and ZZ terms show excellent agreement between the exact MC method and the cumulant expansion. We may speculate that the higher-order contributions not captured by the cumulant method in the previous case drop out due to the symmetry of the Hamiltonian.

In conclusion, we have developed a method to numerically compute the exact filter functions of the quantum process description of arbitrary Gaussian noise, and compared the thus obtained filter functions with those from the second-order truncation of the ME and cumulant expansions given in Chapter 11. The approach samples the Liouville-space filter function at discrete frequencies ω_i by simulating the unitary dynamics under monochromatic noise at that frequencies and averaging over the outcomes. We found excellent agreement between the nominally exact and approximate methods in the case of commuting noise as well as the SE DD sequence. For non-commuting noise, we observed the expected deviation at very low frequencies that arises from non-vanishing higher order cumulants.

Rather than random sampling using MC, this average could also be performed deterministically as the expectation value over the probability distributions governing A_i and ϕ,

$$\mathbb{E}_{A_i,\phi}[\mathcal{U}] = \int \mathrm{d}x \, \rho_{A_i}(x) \int \mathrm{d}y \, \rho_{\phi}(y) \mathcal{U}[x, y], \qquad (12.17)$$

where we wrote $\mathcal{U}[x, y]$ for the Liouville representation of the propagator for single x and y drawn from their respective distributions, and $\mathbb{E}_X[A]$ denotes the expectation value of an observable A with respect to the random variable X with probability density function ρ_X. This technique allows the expectation value $\mathbb{E}[\mathcal{U}] \equiv \langle \mathcal{U} \rangle$ to be evaluated to arbitrary precision numerically, but is typically less efficient than MC. It would be interesting to see if the numerical noise observed in off-diagonal elements of the filter functions in Figures 12.1 to 12.3 persists with this method.

The `filter_functions` software package | 13

I N this section we give a brief overview over the `filter_functions` software package implementing the main features of the formalism derived above.[1] This includes the calculation of the decay amplitudes Γ, frequency shifts Δ, and fidelities as well as the calculation of the control matrices for single gates and both generic and periodic sequences of gates. Moreover, control matrices may be efficiently extended to and merged on larger Hilbert spaces. Calculations using unitary conjugation instead of transfer matrices are implemented but at this point not available in the high-level API.

Our software is written in Python and published under the GPLv3 license [77]. It features a broad coverage through unit tests and extensive API documentation as well as didactic examples (see also Chapter 14). The package relies on the `NumPy` [114] and `SciPy` [115] libraries for vectorized array operations. Data visualization is handled by `matplotlib` [116]. For tensor multiplications with optimized contraction order we use `opt_⌋ einsum` [117] for which `sparse` [118], a library aiming to extend the `SciPy` sparse module to multi-dimensional arrays, serves as a backend in the calculation of the trace tensor from Equation 11.18. Lastly, the package is written to interface with qopt [79] and `QuTiP` [78], frameworks for the simulation and optimization of open quantum systems, and mirrors the latter's data structure for Hamiltonians ensuring easy interoperability between the two.

13.1 Package overview

In the `filter_functions` package all operations are understood as sequences of pulses that are applied to a quantum system. These pulses are represented by instances of the `PulseSequence` class which holds information about the physical system (control and noise Hamiltonians) as well as the mathematical description (*e.g.* the basis used for the Liouville representation). As indicated above, the Hamiltonians $H_c(t)$ and $H_n(t)$ are given in a similar structure as in `QuTiP`. That is, a Hamiltonian is expressed as a sum of Hermitian operators with the time dependence encoded in piecewise constant coefficients so that

$$H_c(t) = \sum_i a_i^{(g)} A_i = \text{const.} \tag{13.1a}$$

$$H_n(t) = \sum_\alpha s_\alpha^{(g)} B_\alpha = \text{const.} \tag{13.1b}$$

for $t \in (t_{g-1}, t_g], g \in \{1, \dots, G\}$ and where the $a_i^{(g)}$ are the amplitudes of the ith control field. Note that the noise variables $b_\alpha(t)$ are missing from Equation 13.1b because they are captured by the spectral density $S(\omega)$. In the software, Equations 13.1a and 13.1b are represented as lists whose ith element corresponds to a sublist of two elements: the ith operator and the ith coefficients $[a_i^{(0)}, \dots, a_i^{(G)}]$.

The `PulseSequence` class provides methods to calculate and cache the filter function according to Equation 11.30. Alternatively, filter functions

may also be cached manually to permit using the package with analytical solutions for the control matrix. Concatenation of pulses is implemented by the functions `concatenate()` and `concatenate_periodic()` which will attempt to use the cached attributes of the `PulseSequence` instances representing the pulses to efficiently calculate the filter function of the composite pulse following Equation 11.29 and Equation 11.53, respectively.

Operator bases fulfilling Equation 11.14 are implemented by the `Basis` class. There are two predefined types of bases:

1. Pauli bases P_n for $n = 2^d$ qubits from Equation 11.54 and
2. GGM bases Λ_d of arbitrary dimension d from Equation 11.55.

The Pauli basis is both unitary and separable while the GGM basis is sparse for large dimensions but neither unitary nor separable. As mentioned in Section 11.7 (see also Section 14.4), using a separable basis can provide significant performance benefits for calculating the filter functions of algorithms. On the other hand, a sparse basis makes the calculation of the trace tensor T_{ijkl} and therefore also of the error transfer matrix $\tilde{\mathcal{U}}$ much faster (*cf.* Section 11.8). Additionally, the user can define custom bases using the class constructor.

The error transfer matrix $\tilde{\mathcal{U}}$ can be calculated for a given pulse and noise spectrum using the `error_transfer_matrix()` function. Various other quantities can be computed from $\tilde{\mathcal{U}}$ as outlined in Section 11.4. Furthermore, the package includes a plotting module that offers several functions, *e.g.* for the visualization of filter functions or the evolution of the Bloch vector using `QuTiP`.

13.2 Workflow

We now give a short introduction into the workflow of the `filter_` `functions` package by showing how to calculate the dephasing filter function of a simple Hahn SE sequence [119] as an example. The sequence consists of a single π-pulse of finite duration around the x-axis of the Bloch sphere in between two periods of free evolution. We can hence divide the control fields into three constant segments and write the control Hamiltonian as

$$H_{\mathrm{c}}^{(\mathrm{SE})}(t) = \frac{\sigma_x}{2} \times \begin{cases} \pi/t_\pi\,, & \text{if } \tau \leq t < \tau + t_\pi \\ 0, & \text{otherwise} \end{cases} \tag{13.2}$$

with τ the duration of the free evolution period and t_π that of the π pulse. For the noise Hamiltonian we only need to define the deterministic time dependence $s_\alpha(t)$ and operators B_α since the noise strength is captured by the spectrum $S(\omega)$. Thus we have $s_z(t) = 1$ and $B_z = \sigma_z/2$ for pure dephasing noise that couples linearly to the system.

In the software, we first define a `PulseSequence` object representing the SE sequence. As was already mentioned, the control and noise Hamiltonians are given as a list containing lists for every control or noise operator that is considered. These sublists consist of the respective operator as a `NumPy` array or `QuTiP` `Qobj` and the amplitudes ($a_i^{(g)}$ or $s_\alpha^{(g)}$) in an iterable data structure such as a list. We can hence instantiate the `PulseSequence` with the following code:

```python
import filter_functions as ff
import qutip as qt
from math import pi
tau, t_pi = (1, 1e-3)
# Control Hamiltonian for pi rotation in 2nd time step
H_c = [[qt.sigmax()/2, [0, pi/t_pi, 0]]]
# Pure dephasing noise Hamiltonian with linear coupling
H_n = [[qt.sigmaz()/2, [1, 1, 1]]]
# Durations of piecewise constant segments
dt = [tau, t_pi, tau]
ECHO = ff.PulseSequence(H_c, H_n, dt)
```

where a basis is automatically chosen since we did not specify it in the constructor in the last line. Calculating the filter function of the pulse for a given frequency vector omega can then be achieved by calling

```python
F = ECHO.get_filter_function(omega)
```

where F is the dephasing filter function $\mathcal{F}_{zz}(\omega)$ as we only defined a single noise operator. Finally, we calculate the error transfer matrix $\tilde{\mathcal{U}}$ for the noise spectral density $S_{zz}(\omega) = \omega^{-2}$,

```python
S = 1/omega**2
U = ff.error_transfer_matrix(ECHO, S, omega)
```

This code uses the control matrix previously cached when the filter function was first computed. Therefore, only the integration in Equation 11.24 and the calculation of the trace tensor in Equation 11.18 are carried out in the last line.

An alternative approach to calculate the spin echo filter function is to employ the concatenation property. For this, we interpret the SE as a sequence consisting of three separate pulses. Each of the pulses has a single time segment during which a constant control is applied and concatenating the separate `PulseSequence` instances yields the `PulseSequence` representing a spin echo. This way analytical control matrices may be used to calculate the control matrix of the composite sequence. Pulses can be concatenated by using either the `concatenate()` function or the overloaded `@` operator:

```python
# Define PulseSequence objects as shown above
FID = ff.PulseSequence(...)
NOT = ff.PulseSequence(...)
# Cache the analytical control matrices at frequency omega
FID.cache_control_matrix(omega, B_FID)
NOT.cache_control_matrix(omega, B_NOT)
# Concatenate the pulses
ECHO = FID @ NOT @ FID
```

Since we have cached the control matrices of the FID and NOT pulses, that of the ECHO object is also automatically calculated and stored. Concatenating `PulseSequence` objects is implemented as an arithmetic operator of the class to reflect the intrinsic composition property of the control matrices.

Further development of the software has focused on making it available in a gate optimization and simulation framework [120]. Besides using it to compute decoherence effects and fidelities, analytical derivatives of the filter functions have been implemented to allow for optimizing pulse parameters in the presence of non-Markovian noise within the framework of quantum optimal control [79, 121].

Additionally, building an interface with `qupulse` [122, 123], a software toolkit for parametrizing and sequencing control pulses and relaying them to control hardware, would implement the capability to compute filter functions of pulses assembled in `qupulse`, thereby allowing a user in the lab to easily inspect the noise susceptibility characteristics of the pulse they are currently applying to their device.

Example applications | 14

W<small>E</small> now present example applications of the software package and the formalism. As stated before, we focus on the decay amplitudes Γ and its associated filter functions and assume that the unitary errors generated by the frequency shifts Δ are either small (as is the case for gate fidelities) or calibrated out. All of the examples shown below are part of the software documentation as either interactive Jupyter notebooks [124] or Python scripts. In the following, we give angular frequencies and energies in units of inverse times (*e.g.* s^{-1}) while ordinary frequencies are given in Hz and we write $\langle \tilde{\mathcal{U}}(\tau) \rangle = \tilde{\mathcal{U}}$ for legibility.

14.1 Singlet-triplet two-qubit gates

In order to benchmark fidelity predictions of our implementation as well as demonstrate its application to nontrivial pulses, we compute the first-order infidelity of the two-qubit gates presented in Reference 125 and compare the results to the reference's Monte Carlo calculations. There, a numerically optimized gate set consisting of $\{X_{\pi/2} \otimes I, Y_{\pi/2} \otimes I, \text{CNOT}\}$ for exchange-coupled singlet-triplet spin qubits is introduced, taking into account different noise spectra and realistic control hardware.

For readers unfamiliar with the reference we briefly summarize the physical system and noise model entering the optimization. The authors consider four electrons confined in a linear array of four quantum dots in a semiconductor heterostructure. Each electron $i \in \{1, 2, 3, 4\}$ experiences a different static magnetic field B_i so that there is a gradient $b_{ij} = B_i - B_j$ between two adjacent dots i and j. This gives rise to spin quantization along the magnetic field axis and defines the eigenstates $\{|\uparrow\downarrow\rangle, |\downarrow\uparrow\rangle\}$ that span the computational subspace of a single qubit so that the accessible Hilbert space of the two-qubit system is spanned by $\{|\uparrow\downarrow\rangle, |\downarrow\uparrow\rangle\}^{\otimes 2}$. The magnitude of the exchange interaction J_{ij} between two adjacent dots i and j is controlled via gate electrodes located on top of the heterostructure that can be pulsed on a nanosecond timescale with an arbitrary waveform generator (AWG). Changing the gate voltages changes the detuning ϵ_{ij} of the electrochemical potential between dots and in turn leads to a change in exchange coupling according to the phenomenological model $J_{ij}(\epsilon_{ij}) \propto \exp(\epsilon_{ij})$.

The pulses are defined by a set of discrete detuning voltages ϵ_{ij} passed to an AWG with a sample rate of $1\,\text{GS/s}$ and constant magnetic field gradients b_{ij} are assumed. To reflect the fact that the qubits experience a different pulse than what is programmed into the AWG due to cable dispersion and non-ideal control hardware, the detunings are convoluted with an experimental impulse response [125]. Finally, the signal is discretized as piecewise constant by slicing each segment into five steps, yielding a time increment of $\Delta t = 0.2\,\text{ns}$.

To find optimal detuning pulses, a Levenberg-Marquardt algorithm iteratively minimizes the infidelity, leakage, and trace distance from the target unitary. For the infidelity, contributions from quasistatic magnetic field noise as well as quasistatic and white charge noise are taken into account during each iteration. Because treating colored (correlated) noise using
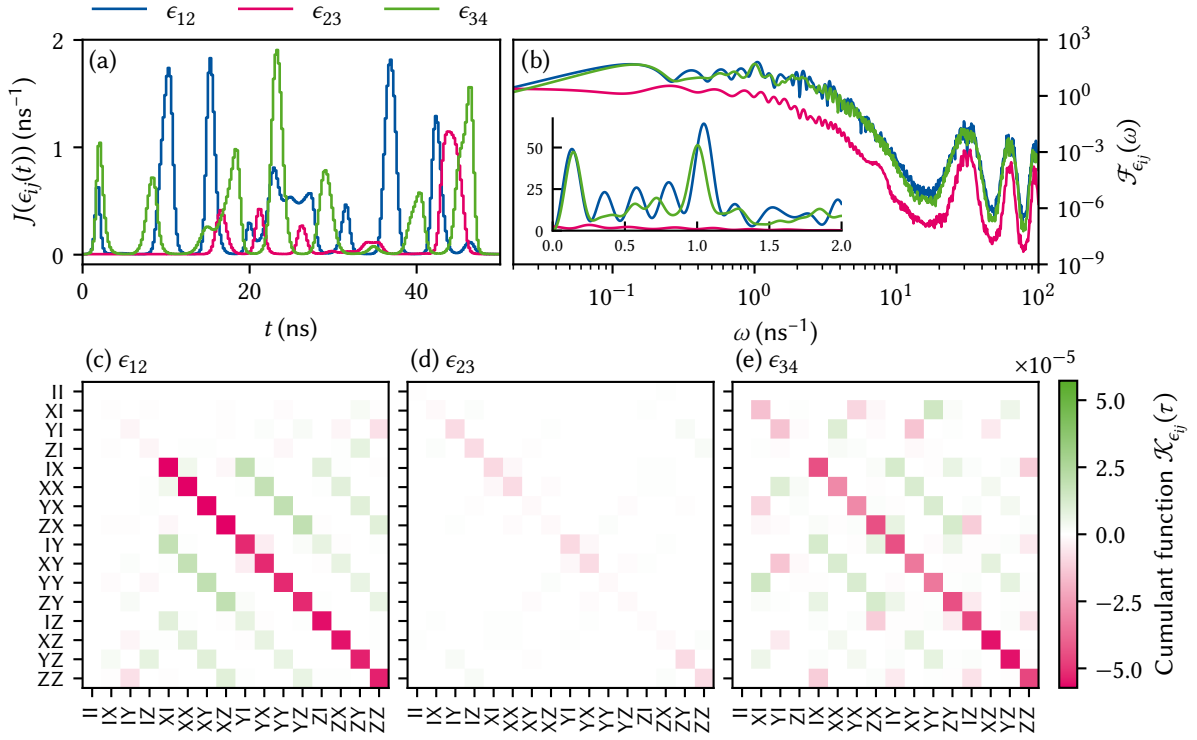
Figure 14.1: (a) Exchange interaction $J(\epsilon_{ij})$ for the CNOT gate presented in Reference 125 as function of time. (b) Filter functions $\mathcal{F}_{\epsilon_{ij}}$ for noise in the detunings evaluated on the computational subspace. The filter functions are modulated by oscillations at high frequencies due to numerical artifacts of the finite step size for the time evolution. The inset shows the filter functions in the DC regime on a linear scale with distinct peaks around $\omega = 2\pi/\tau$ and $\omega = 50/\tau$ ($\tau = 50\,\mathrm{ns}$). (c)–(e) Computational subspace block of the first order approximation of the error transfer matrix, given by the cumulant function $\mathcal{K}_{\alpha\alpha}$ excluding second order contributions, for the CNOT gate and the three detunings $\alpha \in \{\epsilon_{12}, \epsilon_{23}, \epsilon_{34}\}$. Note that in panel (e) the order of the rows and columns was permuted for better comparability.

Monte Carlo methods is computationally expensive (*cf.* Section 11.9), the infidelity due to fast $1/f$-like noise is only computed for the final gate and not used during the optimization.

Two-qubit interactions are mediated via the exchange J_{23} that makes the states $|\uparrow\uparrow\downarrow\downarrow\rangle$ and $|\downarrow\downarrow\uparrow\uparrow\rangle$ accessible. They constitute levels outside of the computational subspace that ideally should only be occupied during an entangling gate operation. A non-vanishing population of these states after the operation has ended is therefore unwanted and considered leakage, the magnitude of which we could quantify following Subsection 11.4.3. However, here we limit ourselves to determine the infidelity contribution from fast, *viz.* non-quasistatic, charge noise entering the system through ϵ_{ij}. That is, we consider noise sources $\alpha \in \{\epsilon_{12}, \epsilon_{23}, \epsilon_{34}\}$. We take the non-linear dependence of the Hamiltonian on the detunings ϵ_{ij} into account by setting $s_{\epsilon_{ij}}(t) = \partial J_{ij}(\epsilon_{ij}(t))\big/\partial\epsilon_{ij}(t) \propto J_{ij}(\epsilon_{ij}(t))$.

Figure 14.1 shows the filtered (convoluted) exchange interaction J_{ij} between each pair of dots during the pulse sequence in panel (a) and filter functions plotted as function of frequency in panel (b) for the three different detunings. For a detailed description on how the filter functions were computed in the presence of additional leakage levels refer to **??**. As one would expect from the fact that the intermediate (inter-qubit) exchange interaction J_{23} (orange dash-dotted lines) is only turned on for short times to entangle the qubits, the filter function for ϵ_{23} is smaller by roughly an order of magnitude than the intra-qubit exchange filter functions. Notably, the filter functions for ϵ_{12} and ϵ_{34} show clear charac-

	THIS WORK		REFERENCE 125	
a	0	0.7	0	0.7
$X_{\pi/2} \otimes I$	1.7×10^{-3}	5.8×10^{-5}	1.9×10^{-3}	5.7×10^{-5}
$Y_{\pi/2} \otimes I$	1.6×10^{-3}	5.7×10^{-5}	1.7×10^{-3}	5.6×10^{-5}
CNOT	1.4×10^{-3}	6.3×10^{-5}	1.6×10^{-3}	6.3×10^{-5}

Table 14.1: Fast charge noise infidelity contributions to the total average gate fidelity of the two-qubit gate set from Reference 125 without capacitive coupling for GaAs S-T$_0$ qubits compared to the original results. The fidelities are consistent with results from the reference within the uncertainty bounds of 3 % of the Monte Carlo calculation. The infidelities presented here are all average gate infidelities (cf. Equation 11.44, Refences 99 and 100).

teristics of DCGs, that is they drop to zero as $\omega \to 0$, and decouple from quasistatic noise with an error suppression $\propto \omega^2$. This is not unexpected as the optimization minimizes quasistatic noise contributions to the infidelity. In addition, one can also observe small oscillations with period $5\,\mathrm{ns}^{-1}$ in frequency space that arise as a numerical artifact of the piecewise constant discretization of the control parameters as investigations have shown. If high-frequency spectral components are expected to play a significant role, one needs to be aware of these effects and adjust the simulation parameters appropriately.

The inset of Figure 14.1(b) shows the same filter functions for the DC tail on a linear scale. Most notably, $\mathcal{F}_{\epsilon_{12}}$ and $\mathcal{F}_{\epsilon_{34}}$ have maxima around $\omega = 2\pi/\tau$, *i.e.* exactly the frequency matching the pulse duration, and around $\omega = 50/\tau = 1\,\mathrm{ns}^{-1}$ with $\tau_{\mathrm{CNOT}} = 50\,\mathrm{ns}$. The former is the typical window in which a pulse is most susceptible to noise whereas the latter matches the absolute value of the magnetic field gradients, $b_{12} = -b_{34} = 1\,\mathrm{ns}^{-1}$, indicating that the peak corresponds to the qubit dynamics generated by the magnetic field gradients. Panels (c)–(e) show the cumulant functions $\mathcal{K}_{\epsilon_{ij}}(\tau)$ of the detuning error channels ϵ_{ij} on the computational subspace. $\mathcal{K}_{\epsilon_{12}}$ displays clear characteristics of a Pauli channel with only elements on the diagonal and secondary diagonals deviating from zero significantly whereas $\mathcal{K}_{\epsilon_{34}}$ (the target qubit) possesses a more complicated structure.

We now compute the infidelity contribution originating from fast charge noise using Equation 11.44 but tracing only over the computational subspace to compare to the Monte Carlo calculations of Reference 125 (see **??** for further details). Like the reference, we use a noise spectrum $S_{\epsilon,a}(f) \propto 1/f^a$ with $S_{\epsilon,a}(1\,\mathrm{MHz}) = 4\times10^{-20}\,\mathrm{V^2/Hz}$ and consider white noise ($a = 0$) and correlated noise with $a = 0.7$ [11] with infrared and ultraviolet cutoffs $1/\tau$ and $100\,\mathrm{ns}^{-1}$, respectively. Table 14.1 compares the results in this work with the reference. The values computed here are consistent with the more elaborate Monte Carlo calculations within a few percent. Notably, the deviation is smaller for the smaller noise levels with $a = 0.7$, in line with the fact that we have only computed the contributions from the decay amplitudes Γ and thus the leading order perturbation.

14.2 Rabi driving

A widely used method for qubit control is Rabi driving [49, 53, 63, 126]. If we restrict ourselves to the resonant case for simplicity, the control Hamiltonian takes on the general form $H_{\mathrm{c}} = \omega_0 \sigma_z/2 + A \sin(\omega_0 t + \phi)\sigma_x$. Here, ω_0 is the resonance frequency, A the drive amplitude corresponding to the Rabi frequency in the weak driving limit $A/\omega_0 \ll 1$, $\Omega_{\mathrm{R}} \approx A$, and ϕ an adjustable phase giving control over the rotation axis in the

xy-plane of the Bloch sphere. This Hamiltonian and associated decoherence mechanisms are well-studied in the weak driving regime, where the rotating-wave approximation (RWA) can be applied to remove fast-oscillating terms in the rotating frame [127, 128]. There is a comprehensive understanding of how spectral densities transform to this frame and which frequencies are most relevant to loss of coherence [129].

By contrast, the description of a system in the strong driving regime, where $A/\omega_0 \sim 1$, is more complicated since the RWA cannot be applied without making large errors. Yet, an improved understanding is desirable because strong driving allows for much shorter gate times and thus shifts the window of relevant noise frequencies towards higher energies where the total noise power is typically lower, *e. g.* for $1/f$ noise. Conversely, faster control also requires more accurate timing to prevent rotation errors. It is therefore of interest to have tools that can provide a comprehensive picture for Rabi pulses over a wide range of driving amplitudes. By making use of the concatenation property of the filter functions, our formalism can do just that.

The problem that arises when trying to numerically investigate Rabi pulses in the weak driving regime in the lab frame is that typical control operations have a duration $\tau \gg T$ with $T = 2\pi/\omega_0$. Since the sampling time step Δt should additionally be chosen much smaller than a single drive period in order to sample the time evolution accurately ($\Delta t \ll T$), brute-force simulations are costly.

For $T/\Delta t = 100$ samples per period and assuming Rabi and drive frequencies in typical regimes for SiGe and metal-oxide-semiconductor (MOS) quantum dots [130, 131] or trapped ions [63], $\Omega_R = 1\,\mu s^{-1}$ and $\omega_0 = 20\,ns^{-1}$, a Monte Carlo simulation of a π-rotation with approximately $3\,\%$ relative error would require 10^9 samples in total. Using the filter-function formalism, we can drastically reduce the simulation time even beyond the improvement gained from concatenating precomputed filter functions of individual drive periods using Equation 11.29. This can be achieved with Equation 11.53, which simplifies the calculation of the control matrix for periodic Hamiltonians.

To benchmark our implementation, we use the parameters from above and calculate the control matrix of a NOT gate generated by a Rabi Hamiltonian with three different methods on an Intel® Core™ i9-9900K eight-core processor. First, we use Equation 11.29 in a brute force approach. Second, we utilize the concatenation property following Equation 11.36. Third, we employ the simplified expression given by Equation 11.53. The brute force approach takes 250 s of wall time whereas calculating the filter function using the standard concatenation is faster by two orders of magnitude, taking 1.5 s to run. Lastly, the calculation utilizing the optimized method is faster again by two orders of magnitude and is completed in 0.056 s.

As an example application, we calculate the filter functions for continuous Rabi driving in the weak and strong driving regimes. For weak driving, we use the parameters from the benchmark above for a pulse of duration $\tau_{weak} \approx 20\,\mu s$ that corresponds to 20 identity rotations in total. For the strong driving regime, we use the approximate analytical solution for a flux qubit biased at its symmetry point from Reference 132 with $A = \omega_0/4$ to drive the qubit for $\tau_{strong} \approx 4\,ns$ so that we achieve the same amount of identity rotations as in the weak driving case. In the reference, strong driving in this regime is shown to give rise to non-negligible counterrotating terms that modulate the Rabi oscillations and which are well-described by Floquet theory applied to the Rabi driving
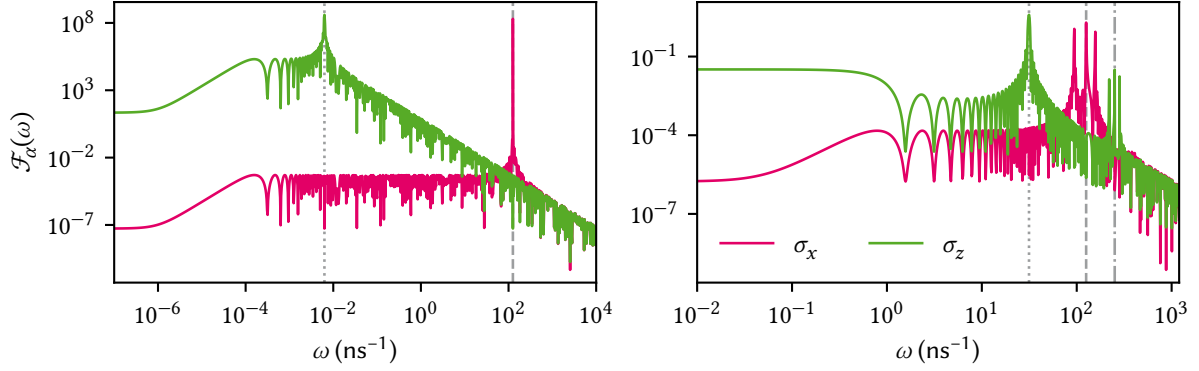
Figure 14.2: Filter functions for weak (a) and strong (b) Rabi driving (20 identity gates in total). gray dashed (dotted) lines indicate the respective drive (Rabi) frequencies ω_0 (Ω_R). (a) Weak driving with $A/\omega_0 \ll 1$. The filter function $\mathscr{F}_x$ for noise operator σ_x is approximately constant up to the resonance frequency where it peaks sharply and then aligns with the filter function $\mathscr{F}_z$ for σ_z. $\mathscr{F}_z$ peaks at the Rabi frequency before rolling off with ω^{-2} and a DC level that is almost ten orders of magnitude larger than the DC level of the transverse filter function $\mathscr{F}_x$. (b) Strong driving with $A/\omega_0 \sim 1$. Again $\mathscr{F}_z$ peaks at Ω_R whereas $\mathscr{F}_x$ has three distinct peaks at ω_0 and $\omega_0 \pm \Omega_R$. These features also appear at $2\omega_0$ in $\mathscr{F}_z$ due to the strong coupling (dash-dotted line).

Hamiltonian. While for the regime studied here only two additional modes appear, the results extend to the regime where $A > \omega_0$ and up to eight different frequency components were observed.

Figure 14.2 shows the filter functions $\mathscr{F}_x$ and $\mathscr{F}_z$ for the σ_x and σ_z noise operators in the weak (a) and the strong (b) driving regime. Both display sharp peaks at their Rabi frequencies and the resonance frequency for $\mathscr{F}_z$ and $\mathscr{F}_x$, respectively. We expect these features as they correspond to perturbations of the qubit Hamiltonian that are resonant with the qubit dynamics about an axis orthogonal to them. For weak driving, $\mathscr{F}_x$ is constant up to the resonance frequency where it peaks sharply and then aligns with $\mathscr{F}_z$. The latter has a peak at the Rabi frequency before rolling off with ω^{-2} and a DC level that is almost ten orders of magnitude larger than that of the transverse filter function. This behavior is consistent with the results by Yan et al. [129], who show that the noise sources dominating decoherence during driven evolution are $S_x(\omega_0)$ and $S_z(\Omega_R)$. Note that the piecewise-constant control approximation causes the weak driving filter functions to level off towards low frequencies after an initial roll-off (here at $\omega \sim 1\,\mathrm{ms}^{-1}$). By decreasing the discretization time step Δt, one can shift the frequency at which this effect occurs to lower frequencies and thus attribute the feature to a numerical artefact of the approximation. However, the decoupling properties depend quite sensitively on the pulse duration.

In case of strong driving, the two filter functions are closer in amplitude for lower frequencies. In addition, $\mathscr{F}_x$ also peaks at $\omega = \omega_0 \pm \Omega_R$. These peaks also show up at higher frequencies in the dephasing filter function $\mathscr{F}_z$, reflecting frequency mixing in the strong coupling regime. While both filter functions show characteristics of a DCG in the weak driving regime, that is they drop to zero as $\omega \to 0$, this is not the case in the strong driving regime. Instead, there they approach a constant level for small frequencies. On top of rotation errors from timing inaccuracies, we may thus expect naive strong driving gates to be more susceptible to quasistatic noise than weak driving gates. By shaping the pulse envelope of the strong driving gate the decoupling properties could be recovered.

14.3 Randomized Benchmarking

Standard randomized benchmarking (SRB) and related methods, for example interleaved randomized benchmarking (IRB), are popular tools to assess the quality of a qubit system and the operations used to control it [86, 133, 134]. The basic protocol consists of constructing K random sequences of varying length m of gates drawn from the Clifford group,[1] and appending a final inversion gate so that the identity operation should be performed in total. Each of these pulse sequences is applied to an initial state $|\psi\rangle$ in order to measure the survival probability $p(|\psi\rangle)$ after the sequence. In reality, the applied operations are subject to noise and experimental imprecisions. This renders them imperfect and results in a survival probability smaller than one. Assuming gate-independent errors, the average gate fidelity F_{avg} is then obtained by fitting the measured survival probabilities for each sequence length to the zeroth-order exponential model [86]

$$p(|\psi\rangle) = A\left(1 - \frac{dr}{d-1}\right)^m + B, \qquad (14.1)$$

where $r = 1 - F_{\mathrm{avg}}$ is the average error per single gate to be extracted from the fit, A and B are parameters capturing state preparation and measurement (SPAM) errors, and d is the dimensionality of the system.

One of the main assumptions of the SRB protocol is that temporal correlations of the noise are small on timescales longer than the average gate time [86]. If this requirement is not satisfied, *e.g.* if $1/f$ noise plays a dominant role, the decay of the sequence fidelity can have nonexponential components [136–138] and a single exponential fit will not produce the true average gate fidelity [139, 140]. The filter-function formalism suggests itself to numerically probe RB experiments in such systems for two reasons. First, it enables the study of gate performance subject to noise with correlation times longer than individual gate times. This regime, where a simple description in terms of individual, isolated quantum operations fails, is accessible in the filter-function formalism because universal classical noise can be included by the power spectral density $S(\omega)$. Second, the simulation of a RB experiment can be performed efficiently by using the concatenation property. Because RB sequences are compiled from a limited set of gates whose filter functions may be precomputed, one only needs to concatenate m filter functions for a single sequence of length m to gain access to the survival probability.

Since for sufficiently long RB sequences $r \in \mathcal{O}(1)$, and we would need to include the frequency shifts Δ in a full simulation following Equation 11.9 because the low-noise approximation Equation 11.43 does not hold in this regime. Unfortunately, the concatenation property does not hold for Δ. Therefore, we focus on the high-fidelity regime where the exponential decay of the sequence fidelity may be approximated to linear order and only the decay amplitudes Γ need to be considered.

In order to evaluate the survival probability of a RB experiment using filter functions, we employ the state fidelity from Subsection 11.4.2 and focus on the single-qubit case with $d = 2$ and the (normalized) Pauli basis from Equation 11.54. Because the ideal action of a RB sequence is the identity we have $\mathcal{Q} = \mathbb{1}$. Assuming we prepare and measure in the computational basis, $|\psi\rangle \in \{|0\rangle, |1\rangle\}$ so that $\sqrt{2}\,|\rho\rangle\!\rangle = |\sigma_0\rangle\!\rangle \pm |\sigma_3\rangle\!\rangle$, we

1: The Clifford group is a subgroup of the special unitary group with the advantage that compositions are easy to compute and that averaging over all unitaries can under reasonable assumptions be replaced by averaging over all Cliffords. This makes the Clifford gates a convenient choice for benchmarking. For a nice, short introduction as well as further references, see [135]

simplify Equation 11.50 to

$$F(|\psi\rangle, \mathcal{U}_{\mathrm{RB}}(|\psi\rangle\langle\psi|)) = \frac{1}{2}(\tilde{\mathcal{U}}_{00} + \tilde{\mathcal{U}}_{33} \pm \tilde{\mathcal{U}}_{03} \pm \tilde{\mathcal{U}}_{30}) = \frac{1 + \tilde{\mathcal{U}}_{33}}{2}$$
$$\approx 1 - \frac{1}{2}\sum_{k\neq 3}\Gamma_{kk}.$$
(14.2)

For the second equality we used that $\tilde{\mathcal{U}}$ is trace-preserving and unital (*cf.* Subsection 11.1.2) while in the last step we approximated the expression using Equations 11.22 and 11.43. For our simulation, we neglect SPAM errors so that $A = B = 0.5$, choose $|\psi\rangle = |0\rangle$, and approximate Equation 14.1 as

$$p(|0\rangle) = F(|0\rangle, \mathcal{U}_{\mathrm{RB}}(|0\rangle\langle 0|)) \approx 1 - rm$$
(14.3)

for small gate errors $r \ll 1$ since this is the regime which we can efficiently simulate using the concatenation property.

We simulate single-qubit SRB experiments using three different gate sets to generate the 24 elements of the Clifford group. For the first gate set we implement the group by naive "single" rotations about the symmetry axes of the cube. Each pulse corresponds to a single time segment during which one rotation is performed so that the jth element is given by $Q_j = \exp(-i\phi_j\mathbf{n}_j \cdot \boldsymbol{\sigma})$. We compile the other two gate sets from primitive $\pi/2$ x- and y-rotations so that on average each Clifford gate consists of 3.75 primitive gates (see Reference 141). For the specific implementation of the primitive $\pi/2$-gates we compare "naive" rotations, *i.e.* with a single time segment so that $Q_j = \exp(-i\pi\sigma_j/4)$ for $j \in \{x, y\}$, and the "optimized" gates from Reference 125. Pulse durations are chosen such that the average duration of all 24 Clifford gates generated from a single gate set is equal for all three gate sets. This is to ensure that the different implementations of the Clifford gates are sensitive to the same noise frequencies.

We investigate white noise and correlated noise with $S(\omega) \propto \omega^{-0.7}$ assuming the same noise spectrum on each Cartesian axis of the Bloch sphere and normalize the noise power for each gate set and noise type (white and correlated) so that the average Clifford infidelity r is the same throughout. We then randomly draw $K = 100$ sequences for 11 different lengths $m \in [1, 101]$ and concatenate the m Clifford gates using Equation 11.29 to compute the control matrix of the entire sequence. For the integral in Equation 11.24 we choose the ultraviolet cutoff frequency two orders of magnitude above the inverse duration of the shortest pulse, $f_{\mathrm{UV}} = 10^2/\tau_{\mathrm{min}}$. Similarly, the infrared cutoff is chosen as $f_{\mathrm{IR}} = 10^{-2}/m_{\mathrm{max}}\tau_{\mathrm{max}}$ with $m_{\mathrm{max}} = 101$ and $\tau_{\mathrm{max}} = 7\tau_{\mathrm{min}}$ (since the longest gate is compiled from seven primitive gates with duration τ_{min}) to guarantee that all nontrivial structure of the filter functions is adequately resolved at small frequencies.[2] Finally, we fit Equation 14.3 to the infidelities computed for the different noise spectra.

The results of the simulation are shown in Figure 14.3(a) and (b) for white and correlated noise, respectively. For white noise, the survival probability agrees well with the SRB prediction for all gate types whereas for $1/f$-like noise the "single" gates (green pluses) deviate considerably. Hence, fitting the zeroth-order SRB model to such data will not reveal the true average gate fidelity although errors are of order unity. We note that Refences 136 and 73 found similar results using different methods for $1/f$ and perfectly correlated DC noise, respectively. The former observed SRB to estimate r within 25 % and the latter found the mean of the

2: For a precise fidelity estimate, the infrared cutoff should be extended to $f = 0$. However, we are only interested in a qualitative picture and neglect this part of the spectrum here. At frequencies much smaller than $\approx 1/\tau$ where τ is the duration of the entire control operation, the filter function is constant and we therefore do not disregard any interesting features by setting $f_{\mathrm{IR}} = 10^{-2}/\tau = 10^{-2}/m_{\mathrm{max}}\tau_{\mathrm{max}}$.
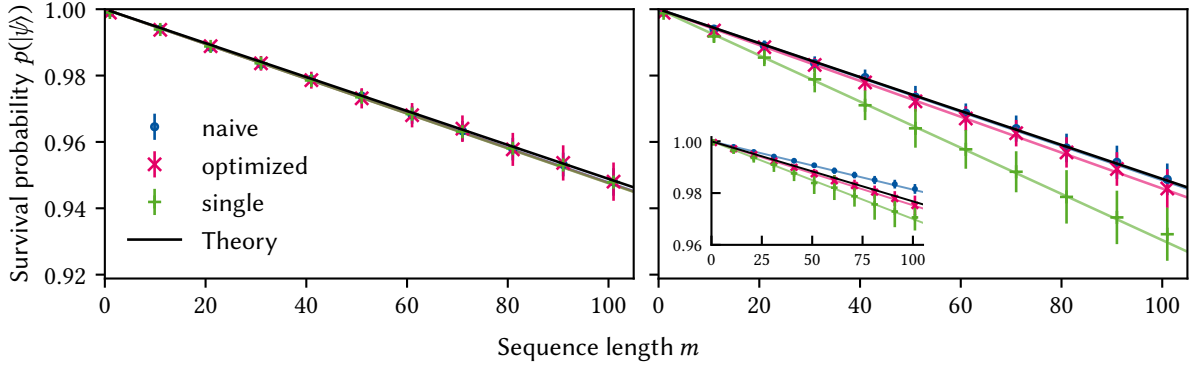
Figure 14.3: Simulation of a SRB experiment using 100 random sequences per point for different gate and noise types (see the main text for an explanation of the gate type monikers). Dashed lines are fits of Equation 14.3 to the data while the solid black lines correspond to a zeroth-order SRB model with $A = B = 0.5$ and the true average gate infidelity per Clifford r. Errorbars show the standard deviation of the SRB sequence fidelities, illustrating that for the "single" gate set noise correlations can lead to amplified destructive and constructive interference of errors. The same noise spectrum is used for all three error channels (σ_x, σ_y, σ_z) and the large plots show the sum of all contributions. (a) Uncorrelated white noise with the noise power adjusted for each gate type so that the average error per gate r is constant over all gate types. No notable deviation is seen between different gate types. (b) Correlated $1/f$-like noise with noise power adjusted to match the average Clifford fidelity in (a). The decay of the "single" gate set differs considerably from that of the other gate sets and the SRB decay expected for the given average gate fidelity, whereas "naive" and "optimized" gates match the zeroth order SRB model well, indicating that correlations in the noise affect the relation between SRB decay and average gate fidelity in a gate-set–dependent way. Inset: contributions from σ_z-noise show that the sequence fidelity can be better than expected for certain gate types and noise channels.

SRB fidelity distribution to deviate from the mode, thereby giving rise to incorrectly estimated fidelities.

On top of affirming the findings by the references, our results demonstrate that the accuracy of the predictions made by SRB theory, *i.e.* that the RB decay rate directly corresponds to the average error rate of the gates, not only depends on the gate implementation but also on which error channels are assumed. This can be seen from the inset of Figure 14.3(b), where only dephasing noise (σ_z) contributions are shown. For this noise channel and the "naive" gates (blue points), one finds a slower RB decay than expected from the actual average gate fidelity, so that the latter would be overestimated by an RB experiment, whereas the "single" gates show the opposite behavior. Depending on the gate set and relevant error channels, non-Markovian noise may thus even lead to improved sequence fidelities due to errors interfering destructively. This behavior is captured by the pulse correlation filter functions whose contributions to the sequence fidelity lead to the deviations from the SRB prediction.

Notably, the data for the "optimized" gates (magenta crosses) agree with the prediction for every noise channel individually which implies that correlations between pulses are suppressed. This highlights the formalism's attractiveness for numerical gate optimization as the pulse correlation filter functions $\mathcal{F}^{(gg')}(\omega)$ may be exploited to suppress correlation errors. To be more explicit, the correlation decay amplitudes $\Gamma^{(gg')}$ from Equation 11.31 can be used to construct cost functions for quantum optimal control algorithms like gradient ascent pulse engineering (GRAPE) [142, 143] or chopped random-basis (CRAB) [144]. By constructing linear combinations of $\Gamma^{(gg')}$ with different pulse indices g and g', correlations between any number of pulses can be specifically targeted and suppressed using numerical pulse optimization.

14.4 Quantum Fourier transform

To demonstrate the flexibility of our software implementation, we calculate filter functions for a four-qubit quantum Fourier transform (QFT) [81, 145] circuit. The QFT routine plays an important role in many quantum algorithms such as Shor's algorithm [146] and quantum phase estimation [81]. For the underlying gate set, we assume a standard Rabi driving model with in-phase/quadrature (IQ) control and nearest neighbor exchange. That is, we assume full control of the x- and y-axes of the individual qubits as well as the exchange interaction mediating coupling between two neighboring qubits. This system allows for native access to the minimal gate set $\mathbb{G} = \{X_i(\pi/2), Y_i(\pi/2), CR_{ij}(\pi/2^3)\}$ where $CR_{ij}(\phi)$ denotes a controlled rotation by ϕ about z with control qubit i and target qubit j. Controlled-z rotations by angles $\pi/2^m$ as required for the QFT can thus be obtained by concatenating 2^{3-m} minimal gates $CR_{ij}(\pi/2^3)$.

Despite native access to all necessary gates, we employ `QuTiP`'s implementation [78] of the GRAPE algorithm [142, 143] to generate the gates in order to highlight our method's suitability for numerically optimized pulses. For the optimization we choose a time step of $\Delta t = 1\,\text{ns}$ and a total gate duration of $\tau = 30\,\text{ns}$. For completeness, see **??** for details on the optimized gates. We then construct the remaining required gates by sequencing these elementary gates, *i.e.* the Hadamard gate $H_i = X_i(\pi/2) \circ X_i(\pi/2) \circ Y_i(\pi/2)$, where $B \circ A$ denotes the composition of gates A and B such that gate A is executed before gate B. To map the canonical circuit [81] onto our specific qubit layout with only nearest-neighbor coupling, we furthermore introduce SWAP operations to couple distant qubits. These gates can be implemented by three CNOTs, $SWAP_{ij} = CNOT_{ij} \circ CNOT_{ji} \circ CNOT_{ij}$. The CNOTs in turn are obtained by a Hadamard transform of the controlled phase gate, $CNOT_{ij} = H_j \circ CR_{ij}(\pi) \circ H_j$. The complete quantum circuit is shown at the top of Figure 14.4; for the canonical circuit with all-to-all connectivity refer to Reference 81. In total, there are 442 elementary pulses, 198 of which are required for the three SWAPs on the first two qubits, so that the entire algorithm would take $\sim 13\,\mu\text{s}$ to run. Note that the circuit could be compressed in time by parallelizing some operations but for simplicity we only execute gates sequentially and do not execute dedicated idling gates.

In order to leverage the extensibility of the filter function approach (see Section 11.7), we use a Pauli basis for the pulses and proceed as follows:

1. Instantiate the `PulseSequence` objects for the elementary gates $\mathbb{G}$ for the first two qubits and cache the control matrices.
2. Compile all required single- and two-qubit pulses by concatenating the `PulseSequences` that implement $\mathbb{G}$.
3. Extend the `PulseSequences` to the full four-qubit Hilbert space.
4. Recursively concatenate recurring gate sequences by concatenating four-qubit `PulseSequences`, *e.g.* $SWAP_{10} \circ CR_{10}(\pi/2^1) \circ H_0$, in order to optimally use the performance benefit offered by Equation 11.29.
5. Concatenate the last `PulseSequences` to get the complete QFT pulse.

For our gate parameters and 400 frequency points, this procedure takes around $5\,\text{s}$ on an Intel® Core™ i9-9900K eight-core processor, whereas computing the filter functions naively using Equation 11.36 takes around $4\,\text{min}$. The resulting filter functions are shown in Figure 14.4 for the noise operators affecting the first qubit. Evidently, the fidelity of the algorithm is most susceptible to DC noise; below roughly $1\,\mu\text{s}^{-1}$ the filter
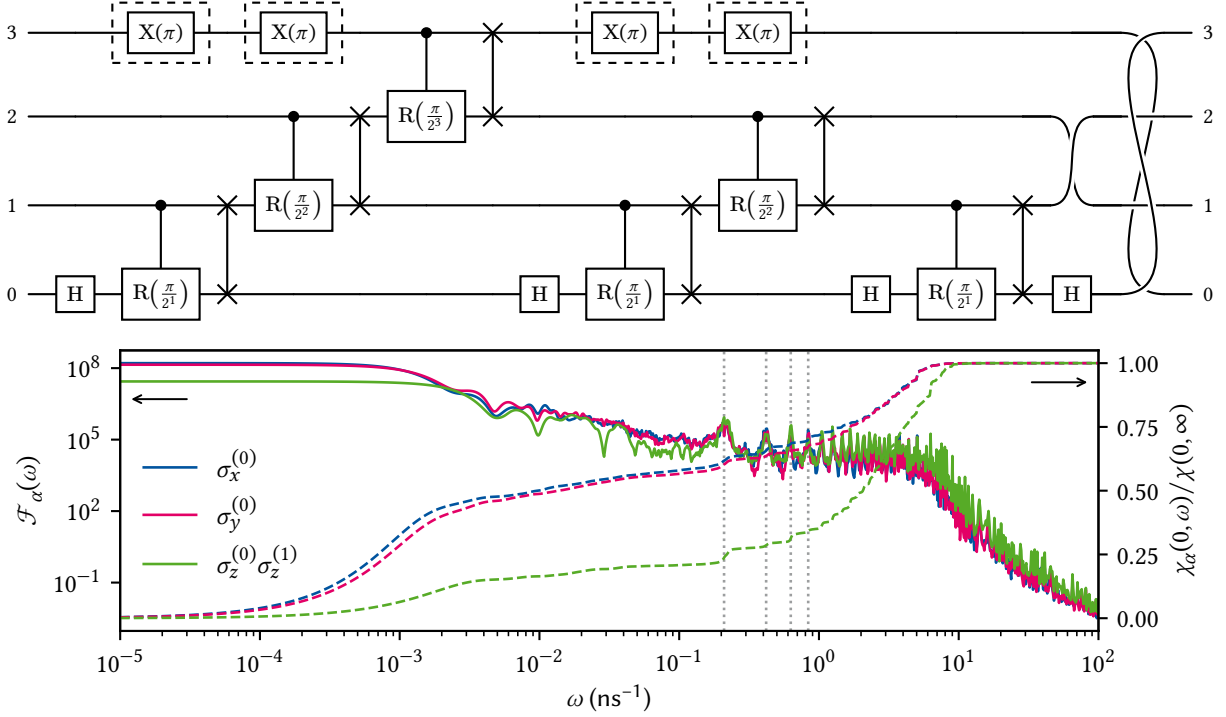
Figure 14.4: Top: Circuit for a QFT on four qubits with nearest-neighbor coupling. Labels next to the wires indicate the qubit index with the permutations at the end of the circuit replacing the final SWAP operations. X-gates in dashed boxes indicate optional echo pulses that leave the action nominally unchanged. Bottom: Filter functions for noise operators on the first qubit ($i = 0$) without echoes. Dotted gray lines indicate the positions of the nth harmonic, $\omega_n = 2\pi n/\tau$ with $\tau = 30\,\text{ns}$ the duration of the gates in $\mathbb{G}$, for $n \in \{1, 2, 3, 4\}$. The filter functions have a baseline of around 10^4 in the range $\omega \in [10^{-1}, 10^1]\,\text{ns}^{-1}$ before they drop down to follow the usual $1/\omega^2$ behavior. The dashed lines show the error sensitivities $\chi_\alpha(\omega_1, \omega_2) := \int_{\omega_1}^{\omega_2} \mathrm{d}\omega \, \mathcal{F}_\alpha(\omega)$ in the frequency band $[0, \omega]$ as a fraction of the total sensitivity $\chi_\alpha(0, \infty)$. These are closely related to the entanglement fidelity (*cf.* Equations 11.26 and 11.49) and suggest that high frequencies up to the knee at $\omega \approx 10\,\text{ns}^{-1}$ cannot be neglected if the cutoff frequency of the noise is sufficiently high or the spectrum does not drop off quickly enough (note the linear scale as opposed to the logarithmic scale for the filter functions).

functions level off at their maximum value. In the GHz range there is a plateau with sharp peaks corresponding to the n harmonics of the inverse pulse duration $\omega_n = 2\pi n/\tau$, where the leftmost belongs to $n = 1$. The dashed lines show the error sensitivities $\chi_\alpha(\omega_1, \omega_2) := \int_{\omega_1}^{\omega_2} \mathrm{d}\omega \, \mathcal{F}(\omega)$ in the frequency band $[0, \omega]$ relative to the total sensitivity $\chi_\alpha(0, \infty)$. For a white spectrum, *i.e.* $S(\omega) = $ const., this quantifies the fraction of the total entanglement infidelity that is accumulated up to frequency ω (*cf.* Equations 11.26 and 11.49). Thus, to obtain a precise estimate of the algorithm's fidelity, five frequency decades need to be taken into account.

To obtain insight into the efficacy of running DD sequences on idling qubits in an algorithm, we insert spin echoes (two $\text{X}(\pi)$ gates amounting to an identity gate) on the fourth qubit before and after the gate operations taking place on this qubit. Exploiting the fact that we assemble the final filter function by concatenating the filter functions of each of the 16 clock cycles, we compute the pulse correlation infidelities (*cf.* Equations 11.31 and 11.48 as well as Equation 11 of Reference 36),

$$I_{\alpha\beta}^{(gg')} = \frac{1}{d} \operatorname{tr} \Gamma_{\alpha\beta}^{(gg')}, \quad g, g' \in \{0, 1, \dots, 15\} \tag{14.4}$$

for $\alpha = \beta \equiv \sigma_y^{(3)}$. The off-diagonal elements of this matrix ($g \neq g'$) capture correlation effects that arise from the concatenation operation alone, while the diagonal elements correspond to the contributions from each single pulse[3] individually. In particular, off-diagonal contributions

3: Or here rather: each single clock cycle of the circuit.
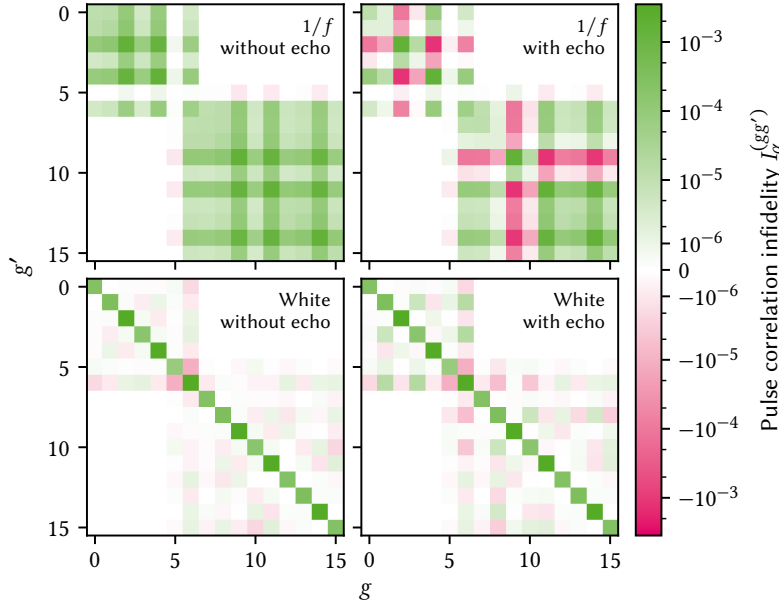
Figure 14.5: Pulse correlation infidelity contributions $I^{(gg')}$ for the noise operator $\sigma_y^{(3)}$ and different noise types (rows) and circuits (columns). The right column corresponds to the circuit with the $X(\pi)$ pulses indicated with dashed boxes in Figure 14.4 inserted, causing echo effects that reduce the overall infidelity for correlated noise. For uncorrelated noise, their effect is negligible.

can be negative, leading to a reduction in infidelity (an enhancement in fidelity) compared to the naive picture of simply adding all individual infidelities,[4] $I = \sum_g I^{(gg)}$. For uncorrelated (white) noise, we expect $I^{(gg')} \approx 0$ for $g \neq g'$ because the noise has no "memory", that is, cannot transport effects from one time step to another. Indeed, the sum rule for fidelity filter functions, which we prove in **??**, states that for white noise the fidelity depends only on the total duration τ and can therefore not be influenced by whichever control operation happened before or after. This stands in contrast to correlated (*e.g.*, $1/f$) noise, where interference can cause random phases picked up at one point in the sequence be reversed at another [36].

In Figure 14.5, we show the correlation infidelities $I^{(gg')}$ computed for the QFT algorithm shown in Figure 14.4. The figure shows results for $1/f$ noise in the top row, and white noise in the bottom, while the first column shows the algorithm without the echo pulses and the second with. To facilitate a qualitative comparison, the noise level in the simulation was adjusted so that for white noise the total infidelity without echoes was the same as for $1/f$ noise. The infidelity in the case of white noise is indeed dominated by the diagonal elements as we would expect. Adding decoupling pulses does not change the fidelity significantly as the addition does not change the total duration of the circuit. In the case of $1/f$ noise, however, the picture is quite different. Here, the overall fidelity is reduced in the circuit without echos as there are significant contributions from correlations at $g \neq g'$. Adding the echo pulses causes some of these contributions to change sign and lead to a reduction in total infidelity of this noise channel by a factor of five. In **??**, we perform MC and GKSL master equation simulations of the QFT circuit to validate the fidelity predictions made by the filter-function formalism.

These insights demonstrate that our method represents a useful tool to analyze how and to which degree small algorithms are affected by correlated errors, and how this effect depends on the gate implementation. It could thus also be used to choose or optimize gates in an algorithm-specific way.

4: Recall that we are approximating the error process to linear order so that $F \sim \prod_g \exp(1 - \epsilon_g) \approx 1 - \sum_g \epsilon_g$.

Conclusion and outlook $\big|$ **15**

Before we conclude, let us address two possible avenues for future work, one for the formalism itself and one for its application.

To extend our approach to the filter-function formalism beyond the scope discussed in this work, the most evident path forward is to allow for quantum mechanical baths instead of purely classical ones. Such an extension would facilitate studying for example non-unital T_1-like processes. In fact, the filter-function formalism was originally introduced considering quantum baths such as spin-boson models [57, 58] or more general baths [7, 56, 147], but it remains an open question whether this can be applied to our presentation of the formalism and the numerical implementation in particular. In a fully quantum-mechanical treatment, (sufficiently weak) noise coupling into the quantum system can be modelled via a set of bath operators $\{D_\alpha(t)\}_\alpha$ so that $H_{\mathrm{n}}(t) = \sum_\alpha B_\alpha(t) \otimes D_\alpha(t)$ (the classical case is recovered by replacing $D_\alpha(t) \to b_\alpha(t)\mathbb{1}$) [148]. Accordingly, the ensemble average over the stochastic bath variables $\{b_\alpha(t)\}_\alpha$ needs to be replaced by the quantum expectation value $\mathrm{tr}_B(\,\cdot\,\rho_B)$ with respect to the state ρ_B of the bath B. One therefore needs to deal with correlation functions of bath operators instead of stochastic variables. An immediate consequence for numerical applications is hence an increased dimensionality of the system, which could be dealt with by using analytical expressions for the partial trace over the bath.

For future applications of our method, it would be interesting to study the effects of noise correlations in quantum error correction (QEC) schemes [149–153]. While extensive research has been performed on QEC, noise is usually assumed to be uncorrelated between error correction cycles. In this respect, our formalism may shed light on effects that need to be taken into account for a realistic description of the protocol. As outlined above, we can compute expectation values of (stabilizer) measurements in a straightforward manner from the error transfer matrix. Unfortunately, this implies performing the ensemble average over different noise realizations, therefore removing all correlations between subsequent measurement outcomes for a given noise realization. Hence, the same feature that allows us to calculate the quantum process for correlated noise, namely that we compute only the final map by averaging over all "paths" leading to it, prevents us from studying correlations between consecutive cycles. To overcome this limitation in the context of quantum memory one could invoke the principle of deferred measurement [81] and move all measurements to the end of the circuit, replacing classically controlled operations dependent on the measurement outcomes by conditional quantum operations. Alternatively, to incorporate the probabilistic nature of measurements, one could devise a branching model that implements the classically controlled recovery operation by following both conditional branches of measurement outcomes with weights corresponding to the measurement probabilities as computed from the ensemble-averaged error transfer matrix. An intriguing connection also exists to the quantum Zeno effect, for which quantum systems subject to periodic projective measurements have been identified with a filter function [56, 154, 155] and which recently has been shown to *improve* error correction in the presence of non-Markovian noise [156].

As quantum control schemes become more sophisticated and take into account realistic hardware constraints and sequencing effects, their ana-

lytical description becomes cumbersome, making numerical tools invaluable for analyzing pulse performance. In the above, we have shown that the filter-function formalism lends itself naturally to these tasks since the central objects of our formulation, the interaction picture noise operators, obey a simple composition rule which can be utilized to efficiently calculate them for a sequence of quantum gates. Because the nature of the noise is encoded in a power spectral density in the frequency domain, its effects are isolated from the description of the control until they are evaluated by the overlap integral of noise spectrum and filter function. Hence, the noise operators are highly reusable in calculations and can serve as an economic way of simulating pulse sequences.

Building on the results of Reference 36, we have presented a general framework to study decoherence mechanisms and pulse correlations in quantum systems coupled to generic classical noise environments. By combining the quantum-operations and filter-function formalisms, we have shown in Chapter 11 how to compute the Liouville representation of the error channel of an arbitrary control operation in the presence of Gaussian noise. This expression is exact in the case of commuting noise Hamiltonians, and we have investigated the error of the perturbative expansion in all other cases in Chapter 12, finding that the filter functions for single elements of the error transfer matrix deviate from the exact results at very low frequency and close to zeros of the functions. Furthermore, we have introduced the `filter_functions` Python software package that implements the aforementioned method in Chapter 13. We showed both analytically and numerically that our software implementation can outperform Monte Carlo techniques by orders of magnitude. By employing the formalism and software to study several examples in Chapter 14, we demonstrated the wide range of possible applications.

The capacity for applications in quantum optimal control has already been established above. In Reference 121, we presented analytical derivatives for the fidelity filter function, Equation 11.26, and their implementation in the software package. Together with the infidelity, Equation 11.49, they can serve as efficient cost functions for pulse optimization in the presence of realistic, correlated noise [79]. Since our method offers insight into correlations between pulses at different positions in a sequence, the pulse correlation filter function $F^{(gg')}(\omega)$ with $g \neq g'$ can additionally serve as a tool for studying under which conditions pulses decouple from noise with long correlation times. Such insight would be valuable to design pulses for algorithms. Another interesting application could be quantum error correction in the regime of long-time correlated noise as outlined above, where we also briefly touched upon a possible extension of the framework to quantum mechanical baths.

The tools presented here, both analytical and numerical as implemented in the `filter_functions` software package [77], provide an accessible way for computing filter functions in generic control settings across the different material platforms employed in quantum technologies and beyond.

APPENDIX

Bibliography

[1] Hendrik Bluhm, Tobias Hangleiter, Malte Neul, Eugen Kammerloher, Lino Visser, Max Beer, Alexander Willmes, Tom Struck, Till Huckemann, Daniel Grothe, Simon Humpohl, Ran Xue, Paul Surrey, Han Na We, and Lars Schreiber. "Research Techniques for Advanced Solid State Device Experiments." Course material. Aachen, 2022 (cited on pages 2, 3).

[2] Jonathan P. Dowling and Gerard J. Milburn. "Quantum Technology: The Second Quantum Revolution." In: *Philosophical Transactions of the Royal Society of London. Series A: Mathematical, Physical and Engineering Sciences* 361.1809 (Aug. 15, 2003). Ed. by A. G. J. MacFarlane, pp. 1655–1674. DOI: 10.1098/rsta.2003.1227 (cited on page 2).

[3] Alain Aspect. *Einstein and the Quantum Revolutions*. Trans. by David Kaiser Translated by Teresa Lavender Fagan. The France Chicago Collection. Chicago, IL: University of Chicago Press, Oct. 2024. 112 pp. (cited on page 2).

[4] A. A. Clerk, M. H. Devoret, S. M. Girvin, Florian Marquardt, and R. J. Schoelkopf. "Introduction to Quantum Noise, Measurement, and Amplification." In: *Reviews of Modern Physics* 82.2 (Apr. 15, 2010), pp. 1155–1208. DOI: 10.1103/RevModPhys.82.1155 (cited on pages 2, 4).

[5] Hendrik Bluhm. "High Frequency Experiments and Methods." Lecture notes. Aachen, 2021 (cited on page 3).

[6] Tobias Hangleiter, Simon Humpohl, Max Beer, Paul Surrey, and René Otten, *Python-Spectrometer* version 2025.9.1, Sept. 8, 2025. Zenodo. DOI: 10.5281/zenodo.17079009, (cited on page 3).

[7] Gerardo A. Paz-Silva, Leigh M. Norris, and Lorenza Viola. "Multiqubit Spectroscopy of Gaussian Quantum Noise." In: *Physical Review A* 95.2 (Feb. 23, 2017), p. 022121. DOI: 10.1103/PhysRevA.95.022121 (cited on pages 4, 71, 116).

[8] Eric W. Weisstein. *Root-Mean-Square*. URL: https://mathworld.wolfram.com/Root-Mean-Square.html (visited on 04/21/2025) (cited on page 4).

[9] Gonzalo A. Álvarez and Dieter Suter. "Measuring the Spectrum of Colored Noise by Dynamical Decoupling." In: *Physical Review Letters* 107.23 (Nov. 30, 2011), p. 230501. DOI: 10.1103/PhysRevLett.107.230501 (cited on pages 4, 71).

[10] P Szańkowski, G Ramon, J Krzywda, D Kwiatkowski, and Ł Cywiński. "Environmental Noise Spectroscopy with Qubits Subjected to Dynamical Decoupling." In: *Journal of Physics: Condensed Matter* 29.33 (Aug. 23, 2017), p. 333001. DOI: 10.1088/1361-648X/aa7648 (cited on pages 4, 10, 78).

[11] O. E. Dial, M. D. Shulman, S. P. Harvey, H. Bluhm, V. Umansky, and A. Yacoby. "Charge Noise Spectroscopy Using Coherent Exchange Oscillations in a Singlet-Triplet Qubit." In: *Physical Review Letters* 110.14 (Apr. 5, 2013), p. 146804. DOI: 10.1103/PhysRevLett.110.146804 (cited on pages 4, 71, 107).

[12] Elliot J. Connors, J. Nelson, Lisa F. Edge, and John M. Nichol. "Charge-Noise Spectroscopy of Si/SiGe Quantum Dots via Dynamically-Decoupled Exchange Oscillations." In: *Nature Communications* 13.1 (Dec. 2022), p. 940. DOI: 10.1038/s41467-022-28519-x (cited on pages 4, 70).

[13] Norbert Wiener. "Generalized Harmonic Analysis." In: *Acta Mathematica* 55 (none Jan. 1930), pp. 117–258. DOI: 10.1007/BF02546511 (cited on pages 4, 6).

[14] A. Khintchine. "Korrelationstheorie der stationären stochastischen Prozesse." In: *Mathematische Annalen* 109.1 (Dec. 1, 1934), pp. 604–615. DOI: 10.1007/BF01449156 (cited on pages 4, 6).

[15] Arian Vezvaee, Nanako Shitara, Shuo Sun, and Andrés Montoya-Castillo. "Fourier Transform Noise Spectroscopy." In: *npj Quantum Information* 10.1 (May 17, 2024), pp. 1–12. DOI: 10.1038/s41534-024-00841-w (cited on page 5).

[16] Lambert Herman Koopmans. *The Spectral Analysis of Time Series*. 2nd ed. Vol. 22. Probability and Mathematical Statistics. San Diego: Academic Press, 1995 (cited on pages 5, 6, 8).

[17] G. E. Uhlenbeck and L. S. Ornstein. "On the Theory of the Brownian Motion." In: *Physical Review* 36.5 (Sept. 1, 1930), pp. 823–841. DOI: 10.1103/PhysRev.36.823 (cited on page 6).

[18] N. G Van Kampen. "Stochastic Differential Equations." In: *Physics Reports* 24.3 (Mar. 1, 1976), pp. 171–228. DOI: 10.1016/0370-1573(76)90029-6 (cited on page 6).

[19] N. R. Lomb. "Least-Squares Frequency Analysis of Unequally Spaced Data." In: *Astrophysics and Space Science* 39.2 (Feb. 1, 1976), pp. 447–462. DOI: 10.1007/BF00648343 (cited on page 7).

[20] J. D. Scargle. "Studies in Astronomical Time Series Analysis. II. Statistical Aspects of Spectral Analysis of Unevenly Spaced Data." In: *The Astrophysical Journal* 263 (Dec. 1, 1982), pp. 835–853. DOI: 10.1086/160554 (cited on page 7).

[21] M. S. Bartlett. "Smoothing Periodograms from Time-Series with Continuous Spectra." In: *Nature* 161.4096 (May 1948), pp. 686–687. DOI: 10.1038/161686a0 (cited on page 7).

[22] P. Welch. "The Use of Fast Fourier Transform for the Estimation of Power Spectra: A Method Based on Time Averaging over Short, Modified Periodograms." In: *IEEE Transactions on Audio and Electroacoustics* 15.2 (June 1967), pp. 70–73. DOI: 10.1109/TAU.1967.1161901 (cited on pages 7, 9).

[23] F.J. Harris. "On the Use of Windows for Harmonic Analysis with the Discrete Fourier Transform." In: *Proceedings of the IEEE* 66.1 (Jan. 1978), pp. 51–83. DOI: 10.1109/PROC.1978.10837 (cited on page 8).

[24] Wikipedia contributors. *Window Function.* Wikipedia, The Free Encyclopedia. Mar. 20, 2025. URL: https://en.wikipedia.org/w/index.php?title=Window_function&oldid=1281514999 (visited on 03/27/2025) (cited on page 8).

[25] A. Nuttall. "Some Windows with Very Good Sidelobe Behavior." In: *IEEE Transactions on Acoustics, Speech, and Signal Processing* 29.1 (Feb. 1981), pp. 84–91. DOI: 10.1109/TASSP.1981.1163506 (cited on page 8).

[26] Ronald Forrest Fox. "Gaussian Stochastic Processes in Physics." In: *Physics Reports* 48.3 (Dec. 1978), pp. 179–283. DOI: 10.1016/0370-1573(78)90145-X (cited on page 10).

[27] Jan Krzywda and Łukasz Cywiński. "Adiabatic Electron Charge Transfer between Two Quantum Dots in Presence of 1/f Noise." In: *Physical Review B* 101.3 (Jan. 15, 2020), p. 035303. DOI: 10.1103/PhysRevB.101.035303. arXiv: 1909.11780 (cited on page 10).

[28] Josef Schriefl, Yuriy Makhlin, Alexander Shnirman, and Gerd Schön. "Decoherence from Ensembles of Two-Level Fluctuators." In: *New Journal of Physics* 8 (Jan. 20, 2006), pp. 1–1. DOI: 10.1088/1367-2630/8/1/001 (cited on page 10).

[29] Félix Beaudoin and W. A. Coish. "Microscopic Models for Charge-Noise-Induced Dephasing of Solid-State Qubits." In: *Physical Review B* 91.16 (Apr. 29, 2015), p. 165432. DOI: 10.1103/PhysRevB.91.165432. arXiv: 1412.5536 (cited on pages 10, 77).

[30] M. Mehmandoost and V. V. Dobrovitski. "Decoherence Induced by a Sparse Bath of Two-Level Fluctuators: Peculiar Features of $1/f$ Noise in High-Quality Qubits." In: *Physical Review Research* 6.3 (Aug. 15, 2024), p. 033175. DOI: 10.1103/PhysRevResearch.6.033175 (cited on page 10).

[31] C.L. Nikias and J.M. Mendel. "Signal Processing with Higher-Order Spectra." In: *IEEE Signal Processing Magazine* 10.3 (July 1993), pp. 10–37. DOI: 10.1109/79.221324 (cited on page 10).

[32] V. Chandran and S. Elgar. "A General Procedure for the Derivation of Principal Domains of Higher-Order Spectra." In: *IEEE Transactions on Signal Processing* 42.1 (Jan. 1994), pp. 229–233. DOI: 10.1109/78.258147 (cited on page 10).

[33] Leigh M. Norris, Gerardo A. Paz-Silva, and Lorenza Viola. "Qubit Noise Spectroscopy for Non-Gaussian Dephasing Environments." In: *Physical Review Letters* 116.15 (Apr. 14, 2016), p. 150503. DOI: 10.1103/PhysRevLett.116.150503 (cited on pages 10, 70, 81).

[34] Tobias Hangleiter, Pascal Cerfontaine, and Hendrik Bluhm. "Filter-Function Formalism and Software Package to Compute Quantum Processes of Gate Sequences for Classical Non-Markovian Noise." In: *Physical Review Research* 3.4 (Oct. 18, 2021), p. 043047. DOI: 10.1103/PhysRevResearch.3.043047 (cited on page 70).

[35] Tobias Hangleiter. "Filter Function Formalism for Unitary Quantum Operations." MA thesis. Aachen: RWTH Aachen University, Aug. 2019 (cited on page 70).

[36] Pascal Cerfontaine, Tobias Hangleiter, and Hendrik Bluhm. "Filter Functions for Quantum Processes under Correlated Noise." In: *Physical Review Letters* 127.17 (Oct. 18, 2021), p. 170403. DOI: 10.1103/PhysRevLett.127.170403 (cited on pages 70–72, 75, 78, 80–83, 114, 115, 117).

[37] Pascal Cerfontaine. "High-Fidelity Single- and Two-Qubit Gates for Two-Electron Spin Qubits." RWTH Aachen University, 2019 (cited on page 70).

[38] Ryogo Kubo. "Generalized Cumulant Expansion Method." In: *Journal of the Physical Society of Japan* 17.7 (July 1962), pp. 1100–1120. DOI: `10.1143/JPSJ.17.1100` (cited on pages 70, 72, 75, 77, 95).

[39] Ronald Forrest Fox. "Critique of the Generalized Cumulant Expansion Method." In: *Journal of Mathematical Physics* 17.7 (July 1, 1976), pp. 1148–1153. DOI: `10.1063/1.523041` (cited on pages 70, 72, 95, 98).

[40] Tobias Hangleiter, Pascal Cerfontaine, and Hendrik Bluhm. "Erratum: Filter-function Formalism and Software Package to Compute Quantum Processes of Gate Sequences for Classical Non-Markovian Noise [Phys. Rev. Research 3, 043047 (2021)]." In: *Physical Review Research* 6.4 (Oct. 16, 2024), p. 049001. DOI: `10.1103/PhysRevResearch.6.049001` (cited on pages 70, 75).

[41] David P. DiVincenzo. "Two-Bit Gates Are Universal for Quantum Computation." In: *Physical Review A* 51.2 (Feb. 1, 1995), pp. 1015–1022. DOI: `10.1103/PhysRevA.51.1015` (cited on page 70).

[42] Vittorio Gorini, Andrzej Kossakowski, and E. C. G. Sudarshan. "Completely Positive Dynamical Semigroups of N-level Systems." In: *Journal of Mathematical Physics* 17.5 (1976), p. 821. DOI: `10.1063/1.522979` (cited on page 70).

[43] G. Lindblad. "On the Generators of Quantum Dynamical Semigroups." In: *Communications in Mathematical Physics* 48.2 (June 1976), pp. 119–130. DOI: `10.1007/BF01608499` (cited on page 70).

[44] M. Brownnutt, M. Kumph, P. Rabl, and R. Blatt. "Ion-Trap Measurements of Electric-Field Noise near Surfaces." In: *Reviews of Modern Physics* 87.4 (Dec. 2015), pp. 1419–1482. DOI: `10.1103/RevModPhys.87.1419` (cited on page 70).

[45] Santosh Kumar, Mauro Brotóns-Gisbert, Rima Al-Khuzheyri, Artur Branny, Guillem Ballesteros-Garcia, Juan F. Sánchez-Royo, and Brian D. Gerardot. "Resonant Laser Spectroscopy of Localized Excitons in Monolayer WSe$_2$." In: *Optica* 3.8 (Aug. 20, 2016), p. 882. DOI: `10.1364/OPTICA.3.000882` (cited on page 70).

[46] Jun Yoneda, Kenta Takeda, Tomohiro Otsuka, Takashi Nakajima, Matthieu R. Delbecq, Giles Allison, Takumu Honda, Tetsuo Kodera, Shunri Oda, Yusuke Hoshi, Noritaka Usami, Kohei M. Itoh, and Seigo Tarucha. "A Quantum-Dot Spin Qubit with Coherence Limited by Charge Noise and Fidelity Higher than 99.9%." In: *Nature Nanotechnology* 13.2 (Feb. 2018), pp. 102–106. DOI: `10.1038/s41565-017-0014-x` (cited on pages 70, 71, 86).

[47] E. Paladino, Y. M. Galperin, G. Falci, and B. L. Altshuler. "$1/f$ Noise: Implications for Solid-State Quantum Information." In: *Reviews of Modern Physics* 86.2 (Apr. 3, 2014), pp. 361–418. DOI: `10.1103/RevModPhys.86.361` (cited on page 70).

[48] Hui Khoon Ng and John Preskill. "Fault-Tolerant Quantum Computation versus Gaussian Noise." In: *Physical Review A* 79.3 (Mar. 16, 2009), p. 032318. DOI: `10.1103/PhysRevA.79.032318`. arXiv: `0810.4953` (cited on page 71).

[49] M. Veldhorst, J. C. C. Hwang, C. H. Yang, A. W. Leenstra, B. de Ronde, J. P. Dehollain, J. T. Muhonen, F. E. Hudson, K. M. Itoh, A. Morello, and A. S. Dzurak. "An Addressable Quantum Dot Qubit with Fault-Tolerant Control-Fidelity." In: *Nature Nanotechnology* 9.12 (Dec. 2014), pp. 981–985. DOI: `10.1038/nnano.2014.216` (cited on pages 71, 86, 107).

[50] S. Debnath, N. M. Linke, C. Figgatt, K. A. Landsman, K. Wright, and C. Monroe. "Demonstration of a Small Programmable Quantum Computer with Atomic Qubits." In: *Nature* 536.7614 (Aug. 4, 2016), pp. 63–66. DOI: `10.1038/nature18648` (cited on page 71).

[51] C. M. Quintana et al. "Observation of Classical-Quantum Crossover of 1/f Flux Noise and Its Paramagnetic Temperature Dependence." In: *Physical Review Letters* 118.5 (Jan. 31, 2017), p. 057702. DOI: `10.1103/PhysRevLett.118.057702` (cited on page 71).

[52] Filip K. Malinowski, Frederico Martins, Łukasz Cywiński, Mark S. Rudner, Peter D. Nissen, Saeed Fallahi, Geoffrey C. Gardner, Michael J. Manfra, Charles M. Marcus, and Ferdinand Kuemmeth. "Spectrum of the Nuclear Environment for GaAs Spin Qubits." In: *Physical Review Letters* 118.17 (Apr. 28, 2017), p. 177702. DOI: `10.1103/PhysRevLett.118.177702` (cited on page 71).

[53] R. Barends et al. "Superconducting Quantum Circuits at the Surface Code Threshold for Fault Tolerance." In: *Nature* 508.7497 (Apr. 2014), pp. 500–503. DOI: `10.1038/nature13171` (cited on pages 71, 107).

[54]   Robin Blume-Kohout, John King Gamble, Erik Nielsen, Kenneth Rudinger, Jonathan Mizrahi, Kevin Fortier, and Peter Maunz. "Demonstration of Qubit Operations below a Rigorous Fault Tolerance Threshold with Gate Set Tomography." In: *Nature Communications* 8.1 (Apr. 28, 2017), p. 14485. DOI: `10.1038/ncomms14485` (cited on page 71).

[55]   Kaveh Khodjasteh and Lorenza Viola. "Dynamically Error-Corrected Gates for Universal Quantum Computation." In: *Physical Review Letters* 102.8 (Feb. 26, 2009), p. 080501. DOI: `10.1103/PhysRevLett.102.080501`. arXiv: `0810.0698` (cited on pages 71, 75).

[56]   A. G. Kofman and G. Kurizki. "Universal Dynamical Control of Quantum Mechanical Decay: Modulation of the Coupling to the Continuum." In: *Physical Review Letters* 87.27 (Dec. 12, 2001), p. 270405. DOI: `10.1103/PhysRevLett.87.270405` (cited on pages 71, 116).

[57]   John M. Martinis, S. Nam, J. Aumentado, K. M. Lang, and C. Urbina. "Decoherence of a Superconducting Qubit Due to Bias Noise." In: *Physical Review B* 67.9 (Mar. 25, 2003), p. 094510. DOI: `10.1103/PhysRevB.67.094510` (cited on pages 71, 116).

[58]   Götz S. Uhrig. "Keeping a Quantum Bit Alive by Optimized π-Pulse Sequences." In: *Physical Review Letters* 98.10 (Mar. 9, 2007), p. 100504. DOI: `10.1103/PhysRevLett.98.100504` (cited on pages 71, 116).

[59]   Łukasz Cywiński, Roman M. Lutchyn, Cody P. Nave, and S. Das Sarma. "How to Enhance Dephasing Time in Superconducting Qubits." In: *Physical Review B* 77.17 (May 13, 2008), p. 174509. DOI: `10.1103/PhysRevB.77.174509` (cited on pages 71, 75, 83).

[60]   Jonas Bylander, Simon Gustavsson, Fei Yan, Fumiki Yoshihara, Khalil Harrabi, George Fitch, David G. Cory, Yasunobu Nakamura, Jaw-Shen Tsai, and William D. Oliver. "Noise Spectroscopy through Dynamical Decoupling with a Superconducting Flux Qubit." In: *Nature Physics* 7.7 (July 2011), pp. 565–570. DOI: `10.1038/nphys1994` (cited on page 71).

[61]   Michael J. Biercuk, Hermann Uys, Aaron P. VanDevender, Nobuyasu Shiga, Wayne M. Itano, and John J. Bollinger. "Optimized Dynamical Decoupling in a Model Quantum Memory." In: *Nature* 458.7241 (Apr. 23, 2009), pp. 996–1000. DOI: `10.1038/nature07951` (cited on page 71).

[62]   Hermann Uys, Michael Biercuk, and John Bollinger. "Optimized Noise Filtration through Dynamical Decoupling." In: *Physical Review Letters* 103.4 (July 20, 2009), p. 040501. DOI: `10.1103/PhysRevLett.103.040501` (cited on page 71).

[63]   A. Soare, H. Ball, D. Hayes, J. Sastrawan, M. C. Jarratt, J. J. Mcloughlin, X. Zhen, T. J. Green, and M. J. Biercuk. "Experimental Noise Filtering by Quantum Control." In: *Nature Physics* 10.11 (Nov. 19, 2014), pp. 825–829. DOI: `10.1038/nphys3115` (cited on pages 71, 107, 108).

[64]   Todd Green, Hermann Uys, and Michael J. Biercuk. "High-Order Noise Filtering in Nontrivial Quantum Logic Gates." In: *Physical Review Letters* 109.2 (July 9, 2012), p. 020501. DOI: `10.1103/PhysRevLett.109.020501` (cited on pages 71, 81, 83, 87).

[65]   Todd J. Green, Jarrah Sastrawan, Hermann Uys, and Michael J. Biercuk. "Arbitrary Quantum Control of Qubits in the Presence of Universal Noise." In: *New Journal of Physics* 15.9 (Sept. 12, 2013), p. 095004. DOI: `10.1088/1367-2630/15/9/095004`. arXiv: `1211.1163` (cited on pages 71, 72, 77–83).

[66]   Utkan Güngördü and J. P. Kestner. "Pulse Sequence Designed for Robust C-phase Gates in SiMOS and Si/SiGe Double Quantum Dots." In: *Physical Review B* 98.16 (Oct. 1, 2018), p. 165301. DOI: `10.1103/PhysRevB.98.165301` (cited on pages 71, 76, 83).

[67]   Harrison Ball, Michael J. Biercuk, Andre Carvalho, Jiayin Chen, Michael Hush, Leonardo A. De Castro, Li Li, Per J. Liebermann, Harry J. Slatyer, Claire Edmunds, Virginia Frey, Cornelius Hempel, and Alistair Milne. *Software Tools for Quantum Control: Improving Quantum Computer Performance through Noise and Error Suppression.* July 9, 2020. DOI: `10.48550/arXiv.2001.04060`. Pre-published (cited on page 71).

[68]   Wilhelm Magnus. "On the Exponential Solution of Differential Equations for a Linear Operator." In: *Communications on Pure and Applied Mathematics* 7.4 (Nov. 1954), pp. 649–673. DOI: `10.1002/cpa.3160070404` (cited on pages 71, 72, 77).

[69]   S. Blanes, F. Casas, J.A. Oteo, and J. Ros. "The Magnus Expansion and Some of Its Applications." In: *Physics Reports* 470.5–6 (Jan. 2009), pp. 151–238. DOI: `10.1016/j.physrep.2008.11.001` (cited on pages 71, 72, 77).

[70] Gerardo A Paz-Silva and Lorenza Viola. "General Transfer-Function Approach to Noise Filtering in Open-Loop Quantum Control." In: *Physical Review Letters* 113.25 (Dec. 19, 2014), p. 250501. DOI: 10.1103/PhysRevLett.113.250501 (cited on pages 71, 75).

[71] Jens Clausen, Guy Bensky, and Gershon Kurizki. "Bath-Optimized Minimal-Energy Protection of Quantum Operations from Decoherence." In: *Physical Review Letters* 104.4 (Jan. 25, 2010), p. 040401. DOI: 10.1103/PhysRevLett.104.040401 (cited on pages 71, 79).

[72] Chingiz Kabytayev, Todd J. Green, Kaveh Khodjasteh, Michael J. Biercuk, Lorenza Viola, and Kenneth R. Brown. "Robustness of Composite Pulses to Time-Dependent Control Noise." In: *Physical Review A - Atomic, Molecular, and Optical Physics* 90.1 (July 14, 2014), p. 012316. DOI: 10.1103/PhysRevA.90.012316 (cited on page 71).

[73] Harrison Ball, Thomas M. Stace, Steven T. Flammia, and Michael J. Biercuk. "Effect of Noise Correlations on Randomized Benchmarking." In: *Physical Review A* 93.2 (Feb. 1, 2016), p. 022303. DOI: 10.1103/PhysRevA.93.022303 (cited on pages 71, 111).

[74] Jeroen P. G. van Dijk, Erika Kawakami, Raymond N. Schouten, Menno Veldhorst, Lieven M. K. Vandersypen, Masoud Babaie, Edoardo Charbon, and Fabio Sebastiano. "The Impact of Classical Control Electronics on Qubit Fidelity." In: *Physical Review Applied* 12.4 (Oct. 24, 2019), p. 044054. DOI: 10.1103/PhysRevApplied.12.044054. arXiv: 1803.06176 (cited on page 71).

[75] Ryogo Kubo. "Stochastic Liouville Equations." In: *Journal of Mathematical Physics* 4.2 (Feb. 1963), pp. 174–183. DOI: 10.1063/1.1703941 (cited on pages 72, 75, 78, 95).

[76] Marco Bianucci and Mauro Bologna. "About the Foundation of the Kubo Generalized Cumulants Theory. A Revisited and Corrected Approach." In: *Journal of Statistical Mechanics: Theory and Experiment* 2020.4 (Apr. 1, 2020), p. 043405. DOI: 10.1088/1742-5468/ab7755. arXiv: 1911.09620 [math-ph, stat] (cited on pages 72, 95).

[77] Tobias Hangleiter, Isabel Nha Minh Le, and Julian D. Teske, *Filter_functions* version v1.1.3, May 14, 2024. Zenodo. DOI: 10.5281/ZENODO.4575000, (cited on pages 72, 101, 117).

[78] J. R. Johansson, P. D. Nation, and Franco Nori. "QuTiP: An Open-Source Python Framework for the Dynamics of Open Quantum Systems." In: *Computer Physics Communications* 183.8 (Aug. 1, 2012), pp. 1760–1772. DOI: 10.1016/j.cpc.2012.02.021 (cited on pages 72, 101, 113).

[79] Julian David Teske, Pascal Cerfontaine, and Hendrik Bluhm. "Qopt: An Experiment-Oriented Software Package for Qubit Simulation and Quantum Optimal Control." In: *Physical Review Applied* 17.3 (Mar. 14, 2022), p. 034036. DOI: 10.1103/PhysRevApplied.17.034036 (cited on pages 72, 101, 104, 117).

[80] Karl Kraus, A. Böhm, J. D. Dollard, and W. H. Wootters, eds. *States, Effects, and Operations Fundamental Notions of Quantum Theory*. Vol. 190. Berlin, Heidelberg: Springer Berlin Heidelberg, 1983 (cited on page 74).

[81] Michael A. Nielsen and Isaac L. Chuang. *Quantum Computation and Quantum Information: 10th Anniversary Edition*. 10th ed. Cambridge University Press, 2011 (cited on pages 74, 113, 116).

[82] Isaac L. Chuang and M. A. Nielsen. "Prescription for Experimental Determination of the Dynamics of a Quantum Black Box." In: *Journal of Modern Optics* 44.11–12 (Nov. 1997), pp. 2455–2467. DOI: 10.1080/09500349708231894 (cited on page 74).

[83] J. F. Poyatos, J. I. Cirac, and P. Zoller. "Complete Characterization of a Quantum Process: The Two-Bit Quantum Gate." In: *Physical Review Letters* 78.2 (Jan. 13, 1997), pp. 390–393. DOI: 10.1103/PhysRevLett.78.390 (cited on page 74).

[84] Robin Blume-Kohout, John King Gamble, Erik Nielsen, Jonathan Mizrahi, Jonathan D. Sterk, and Peter Maunz. *Robust, Self-Consistent, Closed-Form Tomography of Quantum Logic Gates on a Trapped Ion Qubit*. Oct. 16, 2013. DOI: 10.48550/arXiv.1310.4492. Pre-published (cited on page 74).

[85] Daniel Greenbaum. *Introduction to Quantum Gate Set Tomography*. Sept. 9, 2015. DOI: 10.48550/arXiv.1509.02921. Pre-published (cited on pages 74, 80, 88).

[86] Easwar Magesan, J. M. Gambetta, and Joseph Emerson. "Scalable and Robust Randomized Benchmarking of Quantum Processes." In: *Physical Review Letters* 106.18 (May 6, 2011), p. 180504. DOI: 10.1103/PhysRevLett.106.180504 (cited on pages 74, 110).

[87] Shelby Kimmel, Marcus P. da Silva, Colm A. Ryan, Blake R. Johnson, and Thomas Ohki. "Robust Extraction of Tomographic Information via Randomized Benchmarking." In: *Physical Review X* 4.1 (Mar. 25, 2014), p. 011050. DOI: 10.1103/PhysRevX.4.011050 (cited on page 74).

[88] Yoshihiro Nambu and Kazuo Nakamura. *On the Matrix Representation of Quantum Operations.* Apr. 12, 2005. DOI: 10.48550/arXiv.quant-ph/0504091. Pre-published (cited on page 74).

[89] U. Fano. "Description of States in Quantum Mechanics by Density Matrix and Operator Techniques." In: *Reviews of Modern Physics* 29.1 (Jan. 1, 1957), pp. 74–93. DOI: 10.1103/RevModPhys.29.74 (cited on page 74).

[90] Yuan-Chi Yang, S. N. Coppersmith, and Mark Friesen. "Achieving High-Fidelity Single-Qubit Gates in a Strongly Driven Charge Qubit with 1/f Charge Noise." In: *npj Quantum Information* 5.1 (Dec. 2019), p. 12. DOI: 10.1038/s41534-019-0127-1 (cited on page 75).

[91] P C Moan, J A Oteo, and J Ros. "On the Existence of the Exponential Solution of Linear Differential Systems." In: *Journal of Physics A: Mathematical and General* 32.27 (1999), pp. 5133–5139. DOI: 10.1088/0305-4470/32/27/311 (cited on page 77).

[92] Kyle Willick, Daniel K. Park, and Jonathan Baugh. "Efficient Continuous-Wave Noise Spectroscopy beyond Weak Coupling." In: *Physical Review A* 98.1 (July 18, 2018), p. 013414. DOI: 10.1103/PhysRevA.98.013414 (cited on page 77).

[93] Pascal Cerfontaine, René Otten, and Hendrik Bluhm. "Self-Consistent Calibration of Quantum Gate Sets." In: *Physical Review Applied* 13.4 (Apr. 28, 2020), p. 044071. DOI: 10.1103/PhysRevApplied.13.044071. arXiv: 1906.00950 (cited on page 78).

[94] Shelby Kimmel, Guang Hao Low, and Theodore J. Yoder. "Robust Calibration of a Universal Single-Qubit Gate Set via Robust Phase Estimation." In: *Physical Review A* 92.6 (Dec. 8, 2015), p. 062315. DOI: 10.1103/PhysRevA.92.062315 (cited on page 78).

[95] Mark Byrd and Daniel Lidar. "Bang–Bang Operations from a Geometric Perspective." In: *Quantum Information Processing* 1.1/2 (2002), pp. 19–34. DOI: 10.1023/A:1019697017584 (cited on page 79).

[96] Daniel Loss and David P. DiVincenzo. "Quantum Computation with Quantum Dots." In: *Physical Review A* 57.1 (Jan. 1, 1998), pp. 120–126. DOI: 10.1103/PhysRevA.57.120 (cited on page 86).

[97] T. D. Ladd, F. Jelezko, R. Laflamme, Y. Nakamura, C. Monroe, and J. L. O'Brien. "Quantum Computers." In: *Nature* 464.7285 (7285 Mar. 2010), pp. 45–53. DOI: 10.1038/nature08812 (cited on page 86).

[98] Jerry M. Chow, Jay M. Gambetta, A. D. Córcoles, Seth T. Merkel, John A. Smolin, Chad Rigetti, S. Poletto, George A. Keefe, Mary B. Rothwell, J. R. Rozen, Mark B. Ketchen, and M. Steffen. "Universal Quantum Gate Set Approaching Fault-Tolerant Thresholds with Superconducting Qubits." In: *Physical Review Letters* 109.6 (Aug. 9, 2012), p. 060501. DOI: 10.1103/PhysRevLett.109.060501 (cited on page 86).

[99] Michał Horodecki, Paweł Horodecki, and Ryszard Horodecki. "General Teleportation Channel, Singlet Fraction, and Quasidistillation." In: *Physical Review A* 60.3 (Sept. 1, 1999), pp. 1888–1898. DOI: 10.1103/PhysRevA.60.1888 (cited on pages 87, 107).

[100] Michael A. Nielsen. "A Simple Formula for the Average Gate Fidelity of a Quantum Dynamical Operation." In: *Physics Letters A* 303.4 (Oct. 7, 2002), pp. 249–252. DOI: 10.1016/S0375-9601(02)01272-0 (cited on pages 87, 107).

[101] Joel J. Wallman and Steven T. Flammia. "Randomized Benchmarking with Confidence." In: *New Journal of Physics* 16.10 (Oct. 20, 2014), p. 103032. DOI: 10.1088/1367-2630/16/10/103032 (cited on page 88).

[102] Jens Koch, Terri M. Yu, Jay Gambetta, A. A. Houck, D. I. Schuster, J. Majer, Alexandre Blais, M. H. Devoret, S. M. Girvin, and R. J. Schoelkopf. "Charge-Insensitive Qubit Design Derived from the Cooper Pair Box." In: *Physical Review A* 76.4 (Oct. 12, 2007), p. 042319. DOI: 10.1103/PhysRevA.76.042319 (cited on page 88).

[103] J. R. Petta, A. C. Johnson, J. M. Taylor, E. A. Laird, A. Yacoby, M. D. Lukin, C. M. Marcus, M. P. Hanson, and A. C. Gossard. "Coherent Manipulation of Coupled Electron Spins in Semiconductor Quantum Dots." In: *Science* 309.5744 (Sept. 30, 2005), pp. 2180–2184. DOI: 10.1126/science.1116955 (cited on page 88).

[104] Christopher J. Wood and Jay M. Gambetta. "Quantification and Characterization of Leakage Errors." In: *Physical Review A* 97.3 (Mar. 8, 2018), p. 032306. DOI: 10.1103/PhysRevA.97.032306 (cited on page 88).

[105] Gen Kimura. "The Bloch Vector for N-level Systems." In: *Physics Letters A* 314.5–6 (Aug. 21, 2003), pp. 339–349. DOI: 10.1016/S0375-9601(03)00941-1 (cited on page 90).

[106] Reinhold A Bertlmann and Philipp Krammer. "Bloch Vectors for Qudits." In: *Journal of Physics A: Mathematical and Theoretical* 41.23 (June 13, 2008), p. 235303. DOI: 10.1088/1751-8113/41/23/235303 (cited on page 90).

[107] F. T. Hioe and J. H. Eberly. "N-Level Coherence Vector and Higher Conservation Laws in Quantum Optics and Quantum Mechanics." In: *Physical Review Letters* 47.12 (Sept. 21, 1981), pp. 838–841. DOI: 10.1103/PhysRevLett.47.838 (cited on page 90).

[108] Don Coppersmith and Shmuel Winograd. "Matrix Multiplication via Arithmetic Progressions." In: *Journal of Symbolic Computation* 9.3 (Mar. 1990), pp. 251–280. DOI: 10.1016/S0747-7171(08)80013-2 (cited on page 92).

[109] N. G. Van Kampen. "A Cumulant Expansion for Stochastic Linear Differential Equations. I." In: *Physica* 74.2 (June 1, 1974), pp. 215–238. DOI: 10.1016/0031-8914(74)90121-9 (cited on page 95).

[110] N. G. Van Kampen. "A Cumulant Expansion for Stochastic Linear Differential Equations. II." In: *Physica* 74.2 (June 1, 1974), pp. 239–247. DOI: 10.1016/0031-8914(74)90122-0 (cited on page 95).

[111] Lotte Geck. "Scalable Control Electronics for a Spin Based Quantum Computer." PhD thesis. Jülich: Forschungszentrum Jülich GmbH, 2021 (cited on page 96).

[112] Wikipedia contributors. *Rayleigh Distribution*. Wikipedia, The Free Encyclopedia. July 20, 2024. URL: https://en.wikipedia.org/w/index.php?title=Rayleigh_distribution&oldid=1235639507 (visited on 01/10/2025) (cited on page 97).

[113] Awad H. Al-Mohy, Nicholas J. Higham, and Samuel D. Relton. "Computing the Fréchet Derivative of the Matrix Logarithm and Estimating the Condition Number." In: *SIAM Journal on Scientific Computing* 35.4 (Jan. 2013), pp. C394–C410. DOI: 10.1137/120885991 (cited on page 97).

[114] Charles R. Harris et al. "Array Programming with NumPy." In: *Nature* 585.7825 (Sept. 17, 2020), pp. 357–362. DOI: 10.1038/s41586-020-2649-2 (cited on page 101).

[115] Pauli Virtanen et al. "SciPy 1.0: Fundamental Algorithms for Scientific Computing in Python." In: *Nature Methods* 17.3 (Mar. 2, 2020), pp. 261–272. DOI: 10.1038/s41592-019-0686-2 (cited on page 101).

[116] John D. Hunter. "Matplotlib: A 2D Graphics Environment." In: *Computing in Science & Engineering* 9.3 (2007), pp. 90–95. DOI: 10.1109/MCSE.2007.55 (cited on page 101).

[117] Daniel G. A. Smith and Johnnie Gray. "Opt_einsum - A Python Package for Optimizing Contraction Order for Einsum-like Expressions." In: *Journal of Open Source Software* 3.26 (June 29, 2018), p. 753. DOI: 10.21105/joss.00753 (cited on page 101).

[118] Pydata, *Sparse* 2019. URL: https://github.com/pydata/sparse/ (cited on page 101).

[119] E. L. Hahn. "Spin Echoes." In: *Physical Review* 80.4 (Nov. 15, 1950), pp. 580–594. DOI: 10.1103/PhysRev.80.580 (cited on page 102).

[120] Julian David Teske. "A Software Framework for the Realistic Simulation and Optimal Control of Solid-State Qubits." PhD thesis. Aachen: RWTH Aachen University, Oct. 25, 2022 (cited on page 104).

[121] Isabel Nha Minh Le, Julian D. Teske, Tobias Hangleiter, Pascal Cerfontaine, and Hendrik Bluhm. "Analytic Filter-Function Derivatives for Quantum Optimal Control." In: *Physical Review Applied* 17.2 (Feb. 2, 2022), p. 024006. DOI: 10.1103/PhysRevApplied.17.024006 (cited on pages 104, 117).

[122] Simon Humpohl. PhD thesis. Aachen: RWTH Aachen University, 2025 (cited on page 104).

[123] S. Humpohl, L. Prediger, L. Lankes, A. Willmes, P. Cerfontaine, P. Bethke, E. Kammerloher, L. Schreiber, S. Meyer, B. Rumpe, and H. Bluhm, *Qutech/Qupulse* version 0.6, July 2021. Zenodo. DOI: 10.5281/zenodo.2650139, (cited on page 104).

[124] Thomas Kluyver, Benjamin Ragan-kelley, Fernando Pérez, Brian Granger, Matthias Bussonnier, Jonathan Frederic, Kyle Kelley, Jessica Hamrick, Jason Grout, Sylvain Corlay, Paul Ivanov, Damián Avila, Safia Abdalla, and Carol Willing. "Jupyter Notebooks—a Publishing Format for Reproducible Computational Workflows." In: *Positioning and Power in Academic Publishing: Players, Agents and Agendas*. 2016, pp. 87–90. DOI: 10.3233/978-1-61499-649-1-87 (cited on page 105).

[125] Pascal Cerfontaine, René Otten, M. A. Wolfe, Patrick Bethke, and Hendrik Bluhm. "High-Fidelity Gate Set for Exchange-Coupled Singlet-Triplet Qubits." In: *Physical Review B* 101.15 (Apr. 28, 2020), p. 155311. DOI: 10.1103/PhysRevB.101.155311. arXiv: 1901.00851 (cited on pages 105–107, 111).

[126] A. Wallraff, D. I. Schuster, A. Blais, L. Frunzio, R. S. Huang, J. Majer, S. Kumar, S. M. Girvin, and R. J. Schoelkopf. "Strong Coupling of a Single Photon to a Superconducting Qubit Using Circuit Quantum Electrodynamics." In: *Nature* 431.7005 (Sept. 2004), pp. 162–167. DOI: 10.1038/nature02851 (cited on page 107).

[127] E.T. Jaynes and F.W. Cummings. "Comparison of Quantum and Semiclassical Radiation Theories with Application to the Beam Maser." In: *Proceedings of the IEEE* 51.1 (1963), pp. 89–109. DOI: 10.1109/PROC.1963.1664 (cited on page 108).

[128] Christopher C. Gerry and Peter Knight. *Introductory Quantum Optics*. 3. print. Cambridge: Cambridge Univ. Press, 2008. 317 pp. (cited on page 108).

[129] Fei Yan, Simon Gustavsson, Jonas Bylander, Xiaoyue Jin, Fumiki Yoshihara, David G. Cory, Yasunobu Nakamura, Terry P. Orlando, and William D. Oliver. "Rotating-Frame Relaxation as a Noise Spectrum Analyser of a Superconducting Qubit Undergoing Driven Evolution." In: *Nature Communications* 4.1 (Dec. 15, 2013), p. 2337. DOI: 10.1038/ncomms3337. PMID: 23945930 (cited on pages 108, 109).

[130] D. M. Zajac, A. J. Sigillito, M. Russ, F. Borjans, J. M. Taylor, G. Burkard, and J. R. Petta. "Resonantly Driven CNOT Gate for Electron Spins." In: *Science* 359.6374 (Jan. 26, 2018), pp. 439–442. DOI: 10.1126/science.aao5965. PMID: 29217586 (cited on page 108).

[131] Jarryd J. Pla, Kuan Y. Tan, Juan P. Dehollain, Wee H. Lim, John J. L. Morton, David N. Jamieson, Andrew S. Dzurak, and Andrea Morello. "A Single-Atom Electron Spin Qubit in Silicon." In: *Nature* 489.7417 (Sept. 19, 2012), pp. 541–545. DOI: 10.1038/nature11449 (cited on page 108).

[132] Chunqing Deng, Jean-Luc Orgiazzi, Feiruo Shen, Sahel Ashhab, and Adrian Lupascu. "Observation of Floquet States in a Strongly Driven Artificial Atom." In: *Physical Review Letters* 115.13 (Sept. 24, 2015), p. 133601. DOI: 10.1103/PhysRevLett.115.133601 (cited on page 108).

[133] E. Knill, D. Leibfried, R. Reichle, J. Britton, R. B. Blakestad, J. D. Jost, C. Langer, R. Ozeri, S. Seidelin, and D. J. Wineland. "Randomized Benchmarking of Quantum Gates." In: *Physical Review A* 77.1 (Jan. 8, 2008), p. 012307. DOI: 10.1103/PhysRevA.77.012307 (cited on page 110).

[134] Easwar Magesan, Jay M. Gambetta, B. R. Johnson, Colm A. Ryan, Jerry M. Chow, Seth T. Merkel, Marcus P. Da Silva, George A. Keefe, Mary B. Rothwell, Thomas A. Ohki, Mark B. Ketchen, and M. Steffen. "Efficient Measurement of Quantum Gate Error by Interleaved Randomized Benchmarking." In: *Physical Review Letters* 109.8 (Aug. 24, 2012), p. 080505. DOI: 10.1103/PhysRevLett.109.080505 (cited on page 110).

[135] Mãris Ozols. "Clifford Group." July 31, 2008 (cited on page 110).

[136] Jeffrey M. Epstein, Andrew W. Cross, Easwar Magesan, and Jay M. Gambetta. "Investigating the Limits of Randomized Benchmarking Protocols." In: *Physical Review A* 89.6 (June 18, 2014), p. 062321. DOI: 10.1103/PhysRevA.89.062321 (cited on pages 110, 111).

[137] M. A. Fogarty, M. Veldhorst, R. Harper, C. H. Yang, S. D. Bartlett, S. T. Flammia, and A. S. Dzurak. "Nonexponential Fidelity Decay in Randomized Benchmarking with Low-Frequency Noise." In: *Physical Review A* 92.2 (Aug. 11, 2015), p. 022326. DOI: 10.1103/PhysRevA.92.022326. arXiv: 1502.05119 (cited on page 110).

[138] Guanru Feng, Joel J. Wallman, Brandon Buonacorsi, Franklin H. Cho, Daniel K. Park, Tao Xin, Dawei Lu, Jonathan Baugh, and Raymond Laflamme. "Estimating the Coherence of Noise in Quantum Control of a Solid-State Qubit." In: *Physical Review Letters* 117.26 (Dec. 20, 2016), p. 260501. DOI: 10.1103/PhysRevLett.117.260501 (cited on page 110).

[139] S. Mavadia, C. L. Edmunds, C. Hempel, H. Ball, F. Roy, T. M. Stace, and M. J. Biercuk. "Experimental Quantum Verification in the Presence of Temporally Correlated Noise." In: *npj Quantum Information* 4.1 (Dec. 2018), p. 7. DOI: 10.1038/s41534-017-0052-0 (cited on page 110).

[140] C. L. Edmunds, C. Hempel, R. J. Harris, V. Frey, T. M. Stace, and M. J. Biercuk. "Dynamically Corrected Gates Suppressing Spatiotemporal Error Correlations as Measured by Randomized Benchmarking." In: *Physical Review Research* 2.1 (Feb. 13, 2020), p. 013156. DOI: 10.1103/PhysRevResearch.2.013156 (cited on page 110).

[141] Pascal Cerfontaine, Tim Botzem, Julian Ritzmann, Simon Sebastian Humpohl, Arne Ludwig, Dieter Schuh, Dominique Bougeard, Andreas D. Wieck, and Hendrik Bluhm. "Closed-Loop Control of a GaAs-based Singlet-Triplet Spin Qubit with 99.5% Gate Fidelity and Low Leakage." In: *Nature Communications* 11.1 (Dec. 2020), p. 4144. DOI: `10.1038/s41467-020-17865-3` (cited on page 111).

[142] Navin Khaneja, Timo Reiss, Cindie Kehlet, Thomas Schulte-Herbrüggen, and Steffen J. Glaser. "Optimal Control of Coupled Spin Dynamics: Design of NMR Pulse Sequences by Gradient Ascent Algorithms." In: *Journal of Magnetic Resonance* 172.2 (Feb. 2005), pp. 296–305. DOI: `10.1016/j.jmr.2004.11.004` (cited on pages 112, 113).

[143] T. Schulte-Herbrüggen, A. Spörl, N. Khaneja, and S. J. Glaser. "Optimal Control-Based Efficient Synthesis of Building Blocks of Quantum Algorithms: A Perspective from Network Complexity towards Time Complexity." In: *Physical Review A* 72.4 (Oct. 27, 2005), p. 042331. DOI: `10.1103/PhysRevA.72.042331` (cited on pages 112, 113).

[144] Tommaso Caneva, Tommaso Calarco, and Simone Montangero. "Chopped Random-Basis Quantum Optimization." In: *Physical Review A* 84.2 (Aug. 22, 2011), p. 022326. DOI: `10.1103/PhysRevA.84.022326` (cited on page 112).

[145] D. Coppersmith. *An Approximate Fourier Transform Useful in Quantum Factoring*. Technical report, IBM Research Division, 1994. arXiv: `quant-ph/0201067` (cited on page 113).

[146] Peter W. Shor. "Polynomial-Time Algorithms for Prime Factorization and Discrete Logarithms on a Quantum Computer." In: *SIAM Journal on Computing* 26.5 (Oct. 1997), pp. 1484–1509. DOI: `10.1137/S0097539795293172` (cited on page 113).

[147] Tatsuro Yuge, Susumu Sasaki, and Yoshiro Hirayama. "Measurement of the Noise Spectrum Using a Multiple-Pulse Sequence." In: *Physical Review Letters* 107.17 (Oct. 18, 2011), p. 170504. DOI: `10.1103/PhysRevLett.107.170504` (cited on page 116).

[148] Heinz-Peter Breuer and Francesco Petruccione. *The Theory of Open Quantum Systems*. Oxford: Oxford University Press, 2007. 656 pp. (cited on page 116).

[149] Simon J Devitt, William J Munro, and Kae Nemoto. "Quantum Error Correction for Beginners." In: *Reports on Progress in Physics* 76.7 (July 1, 2013), p. 076001. DOI: `10.1088/0034-4885/76/7/076001` (cited on page 116).

[150] Hui Khoon Ng, Daniel A. Lidar, and John Preskill. "Combining Dynamical Decoupling with Fault-Tolerant Quantum Computation." In: *Physical Review A* 84.1 (July 5, 2011), p. 012305. DOI: `10.1103/PhysRevA.84.012305` (cited on page 116).

[151] Naomi H. Nickerson and Benjamin J. Brown. "Analysing Correlated Noise on the Surface Code Using Adaptive Decoding Algorithms." In: *Quantum* 3 (Apr. 8, 2019), p. 131. DOI: `10.22331/q-2019-04-08-131`. arXiv: `1712.00502` (cited on page 116).

[152] B. D. Clader, Colin J. Trout, Jeff P. Barnes, Kevin Schultz, Gregory Quiroz, and Paraj Titum. "Impact of Correlations and Heavy Tails on Quantum Error Correction." In: *Physical Review A* 103.5 (May 24, 2021), p. 052428. DOI: `10.1103/PhysRevA.103.052428` (cited on page 116).

[153] Zhenhuan Liu, Yunlong Xiao, and Zhenyu Cai. *Non-Markovian Noise Suppression Simplified through Channel Representation*. Dec. 15, 2024. DOI: `10.48550/arXiv.2412.11220`. (Visited on 09/05/2025). Pre-published (cited on page 116).

[154] A. G. Kofman and G. Kurizki. "Acceleration of Quantum Decay Processes by Frequent Observations." In: *Nature* 405.6786 (June 2000), pp. 546–550. DOI: `10.1038/35014537` (cited on page 116).

[155] Adam Zaman Chaudhry. "A General Framework for the Quantum Zeno and Anti-Zeno Effects." In: *Scientific Reports* 6.1 (Sept. 13, 2016), p. 29497. DOI: `10.1038/srep29497` (cited on page 116).

[156] Juan Garcia Nila and Todd A. Brun. *Continuous Quantum Correction on Markovian and Non-Markovian Models*. June 24, 2025. DOI: `10.48550/arXiv.2505.18400`. (Visited on 09/05/2025). Pre-published (cited on page 116).

Glossary

Numbers
2DEG two-dimensional electron gas. x

A
API application programming interface. 72, 92, 101

C
CRAB chopped random-basis. 112

D
DAQ data acquisition. 3, 9, 10
DCG dynamically corrected gate. 71, 75, 83, 107, 109
DD dynamical decoupling. 4, 71, 75, 83, 100, 114
DUT device under test. 4

F
FF filter function. 71, 79, 83, 91, 93–99
FFT fast Fourier transform. 10

G
GGM generalized Gell-Mann. 90, 91, 102
GKSL Gorini-Kossakowski-Sudarshan-Lindblad. 70, 115
GRAPE gradient ascent pulse engineering. 112, 113
GST gate set tomography. 74

I
i.i.d. independent and identically distributed. 76
IQ in-phase/quadrature. 113
IRB interleaved randomized benchmarking. 110

L
LIA lock-in amplifier. 4, 10

M
MC Monte Carlo. 72, 89, 91–100, 115, 117
ME Magnus expansion. 71, 72, 75, 77, 78, 84, 86, 100
MOS metal-oxide-semiconductor. 108

P
PL photoluminescence. x
PLE photoluminescence excitation. x
POVM positive operator-valued measure. 88
PSD power spectral density. viii, 3, 5–7, 9, 10, 81, 95, 98
PTM Pauli transfer matrix. 74, 98

Q
QEC quantum error correction. 116
QFT quantum Fourier transform. 73, 90, 113–115
QPT quantum process tomography. 74

R
RB randomized benchmarking. 73, 74, 87, 110, 112
RMS root mean square. 4, 6, 95
RWA rotating-wave approximation. 108

Figure source files and parameters

Declaration of Authorship

I, Tobias Hangleiter, declare that this thesis and the work presented in it are my own and has been generated by me as the result of my own original research.

I do solemnly swear that:

1. This work was done wholly or mainly while in candidature for the doctoral degree at this faculty and university;
2. Where any part of this thesis has previously been submitted for a degree or any other qualification at this university or any other institution, this has been clearly stated;
3. Where I have consulted the published work of others or myself, this is always clearly attributed;
4. Where I have quoted from the work of others or myself, the source is always given. This thesis is entirely my own work, with the exception of such quotations;
5. I have acknowledged all major sources of assistance;
6. Where the thesis is based on work done by myself jointly with others, I have made clear exactly what was done by others and what I have contributed myself;
7. Parts of this work have been published before as:

[1] Yaiza Aragonés-Soria, René Otten, Tobias Hangleiter, Pascal Cerfontaine, and David Gross. "Minimising Statistical Errors in Calibration of Quantum-Gate Sets." June 7, 2022. DOI: 10.48550/arXiv.2206.03417. arXiv: 2206.03417 [quant-ph]. Pre-published.

[2] Pascal Cerfontaine, Tobias Hangleiter, and Hendrik Bluhm. "Filter Functions for Quantum Processes under Correlated Noise." In: *Physical Review Letters* 127.17 (Oct. 18, 2021), p. 170403. DOI: 10.1103/PhysRevLett.127.170403.

[3] Thomas Descamps, Feng Liu, Sebastian Kindel, René Otten, Tobias Hangleiter, Chao Zhao, Mihail Ion Lepsa, Julian Ritzmann, Arne Ludwig, Andreas D. Wieck, Beata E. Kardynał, and Hendrik Bluhm. "Semiconductor Membranes for Electrostatic Exciton Trapping in Optically Addressable Quantum Transport Devices." In: *Physical Review Applied* 19.4 (Apr. 28, 2023), p. 044095. DOI: 10.1103/PhysRevApplied.19.044095.

[4] Thomas Descamps, Feng Liu, Tobias Hangleiter, Sebastian Kindel, Beata E. Kardynał, and Hendrik Bluhm. "Millikelvin Confocal Microscope with Free-Space Access and High-Frequency Electrical Control." In: *Review of Scientific Instruments* 95.8 (Aug. 9, 2024), p. 083706. DOI: 10.1063/5.0200889.

[5] Denny Dütz, Sebastian Kock, Tobias Hangleiter, and Hendrik Bluhm. "Distributed Bragg Reflectors for Thermal Isolation of Semiconductor Spin Qubits." In preparation.

[6] Sarah Fleitmann, Fabian Hader, Jan Vogelbruch, Simon Humpohl, Tobias Hangleiter, Stefanie Meyer, and Stefan van Waasen. "Noise Reduction Methods for Charge Stability Diagrams of Double Quantum Dots." In: *IEEE Transactions on Quantum Engineering* 3 (2022), pp. 1–19. DOI: 10.1109/TQE.2022.3165968.

[7] Fabian Hader, Jan Vogelbruch, Simon Humpohl, Tobias Hangleiter, Chimezie Eguzo, Stefan Heinen, Stefanie Meyer, and Stefan van Waasen. "On Noise-Sensitive Automatic Tuning of Gate-Defined Sensor Dots." In: *IEEE Transactions on Quantum Engineering* 4 (2023), pp. 1–18. DOI: 10.1109/TQE.2023.3255743.

[8] Tobias Hangleiter, Pascal Cerfontaine, and Hendrik Bluhm. "Filter-Function Formalism and Software Package to Compute Quantum Processes of Gate Sequences for Classical Non-Markovian Noise." In: *Physical Review Research* 3.4 (Oct. 18, 2021), p. 043047. DOI: 10.1103/PhysRevResearch.3.043047.

[9] Tobias Hangleiter, Pascal Cerfontaine, and Hendrik Bluhm. "Erratum: Filter-function Formalism and Software Package to Compute Quantum Processes of Gate Sequences for Classical Non-Markovian Noise [Phys. Rev. Research 3, 043047 (2021)]." In: *Physical Review Research* 6.4 (Oct. 16, 2024), p. 049001. DOI: 10.1103/PhysRevResearch.6.049001.

[10] Isabel Nha Minh Le, Julian D. Teske, Tobias Hangleiter, Pascal Cerfontaine, and Hendrik Bluhm. "Analytic Filter-Function Derivatives for Quantum Optimal Control." In: *Physical Review Applied* 17.2 (Feb. 2, 2022), p. 024006. DOI: 10.1103/PhysRevApplied.17.024006.

[11] Paul Surrey, Julian D. Teske, Tobias Hangleiter, Pascal Cerfontaine, and Hendrik Bluhm. "Data-Driven Qubit Characterization and Optimal Control Using Deep Learning." In preparation.

[12] Kui Wu, Sebastian Kindel, Thomas Descamps, Tobias Hangleiter, Jan Christoph Müller, Rebecca Rodrigo, Florian Merget, Beata E. Kardynal, Hendrik Bluhm, and Jeremy Witzens. "Modeling an Efficient Singlet-Triplet-Spin-Qubit-to-Photon Interface Assisted by a Photonic Crystal Cavity." In: *Physical Review Applied* 21.5 (May 24, 2024), p. 054052. DOI: 10.1103/PhysRevApplied.21.054052.

[13] Kui Wu, Sebastian Kindel, Thomas Descamps, Tobias Hangleiter, Jan Christoph Müller, Rebecca Rodrigo, Florian Merget, Hendrik Bluhm, and Jeremy Witzens. "An Efficient Singlet-Triplet Spin Qubit to Fiber Interface Assisted by a Photonic Crystal Cavity." In: *The 25th European Conference on Integrated Optics*. Ed. by Jeremy Witzens, Joyce Poon, Lars Zimmermann, and Wolfgang Freude. Cham: Springer Nature Switzerland, 2024, pp. 365–372. DOI: 10.1007/978-3-031-63378-2_60.

Aachen, September 8, 2025.